

#### Politecnico di Torino Master Degree in Electronic Engineering

### Design-Oriented Modeling of Active Fibers for High-Power Laser Applications

Candidate:

Roberta Carofiglio

Supervisors:

Prof. Guido Perrone

Co-supervisor:

Valentina Serafini



### Abstract

Fiber lasers have become the leading optical source in high-power industrial and medical applications, thanks to their unique combination of efficiency, robustness, and high beam quality. These systems rely on active optical fibers doped with rare-earth ions and pumped by semiconductor laser diodes. For their optimal design and operation, accurate numerical models are essential. However, the predictive capability of such models critically depends on the knowledge of fiber parameters, such as emission and absorption cross sections or rare-earth dopant concentration, which vary significantly with fabrication processes and structural design and are rarely disclosed by manufacturers. This lack of reliable parameter data makes calibration procedures indispensable to ensure meaningful simulations and guide optimization efforts.

This thesis addresses the development of a systematic procedure for recovering the key parameters of active fibers to improve the design of high-power fiber lasers. The proposed methodology is based on fitting experimental results to the predictions of an accurate physical model, with the parameter retrieval carried out using advanced optimization algorithms, in particular particle swarm optimization. To this end, a general simulation framework was implemented in MATLAB, designed to be applicable to virtually any rare-earth dopant. Beyond parameter fitting, the model was employed to investigate the sensitivity of laser performance to variations in simulation parameters, highlighting the most critical quantities on which optimization efforts should concentrate.

The approach was validated through an experimental study on a high-power ytterbium-doped double-cladding fiber. Simulations showed good agreement with experimental measurements, confirming the accuracy, robustness, and practical relevance of the proposed calibration procedure.

Overall, this work demonstrates that, starting from a limited set of experimental data, it is possible to extract reliable parameters for use in simulation and optimization of fiber lasers. The developed methodology thus represents an effective tool for the design and analysis of rare-earth-doped fiber lasers, with particular importance for applications requiring efficient, stable, and scalable high-power light sources.

## Contents

A	bstra	ct		i
C	ontei	nts		iv
Li	st of	Figur	es	x
Li	st of	Table	s	xi
A	crony	yms		xiii
In	trod	uction		1
1	Ove	erview	on the State of the Art	3
	1.1	Histor	rical Background on Rare-Earth-Doped Fiber Lasers	3
	1.2	Fiber	Lasers and Their Principles of Operation	5
	1.3	Limiti	ing Factors and Challenges in High-Power Fiber Lasers	12
		1.3.1	Nonlinear Effects in High-Power Operation	12
		1.3.2	Thermal Effects and Modal Instabilities	13
		1.3.3	Design Trade-offs and Mitigation Strategies	13
	1.4	High 1	Power Laser Application	14
<b>2</b>	The	eoretic	al Framework for Ytterbium-Doped Fiber Systems	17
	2.1	Ytterl	bium-doped gain media	18
	2.2	Rate a	and Propagation Equations	20
		2.2.1	Propagation Equations	22
		2.2.2	Gain Spectrum and Relative Inversion	23
		2.2.3	Fiber Amplifier Model	25
		2.2.4	Fiber Laser Model	26
		2.2.5	Numerical Solution via Shooting Method	28
3	Nu	merica	l modeling and simulation procedures	31
	3.1	Motiv	ations and role of simulation	31
	3.2	Theor	retical framework and numerical solution	32

iv CONTENTS

	3.3	Struct	ure of the simulation code	34
	3.4	Simula	ation results: forward-pumped YDFA and YDFL	38
	3.5	Sensit	ivity Analysis	40
	3.6	Nume	rical Fitting as Preliminary Validation	53
		3.6.1	Particle Swarm Optimization (PSO)	55
	3.7	Result	S	57
		3.7.1	Fitting results for $N_t$	58
		3.7.2	Fitting results for $\tau_{21}$	60
		3.7.3	Fitting results for signal absorption and emission cross-sections	62
		3.7.4	Fitting results for pump absorption and emission cross-sections	65
	3.8	Fitting	g Analysis under Noisy Conditions	67
4	Exp	erime	ntal Validation of the Simulation Model	75
	4.1	Exper	imental Setup	76
	4.2	Sampl	e Configurations	78
		4.2.1	Fiber Bragg Gratings	78
		4.2.2	Spectral Measurements of the Assembled Cavities	80
	4.3	Exper	imental measurements	86
		4.3.1	Pump diode characterization	86
		4.3.2	Cavity measurements	86
	4.4	Fitting	g Results	88
5	Cor	nclusio	$\mathbf{n}\mathbf{s}$	95
C	onclu	ısions		95
$\mathbf{B}^{i}$	ibliog	graphy		97

# List of Figures

1.1	Fundamental light-matter interactions: (1) spontaneous emission, (2)	
	stimulated emission, and (3) absorption	5
1.2	Schematic of a conventional solid-state laser with mirror-based cavity.	6
1.3	Schematic of the fiber indicating the core, cladding, critical angle, and	
	trajectory of a guided ray	7
1.4	Schematics of different laser resonator cavities: (a) dielectric mirrors,	
	(b) Bragg gratings, (c) Sagnac loop, and (d) ring cavity laser	8
1.5	Schematic of (a) End-pumped linear-cavity fiber laser and (b) Co-	
	pumped fiber amplifier	9
1.6	Schematic of a cladding-pumped double-clad fiber amplifier	10
1.7	Different fiber inner cladding and core geometries used to increase	
	pump absorption: (a) offset core fiber, (b) octagonal inner cladding,	
	(c) "D"-shaped inner cladding, (d) square inner cladding	10
1.8	(a) Endlessly single mode PCF; (b) highly nonlinear PCF; (c) Hi-Bi	
	PCF	11
1.9	Conceptual diagram showing the increase of nonlinear effects with	
	higher input power in an optical fiber	12
1.10	Main application sectors of high-power fiber lasers: automotive, aerospace	;
	and defense, electronics, medical, additive manufacturing, and ener-	
	gy/renewables	15
2.1	Comparison of brightness (left) and beam parameter product (BPP,	
	right) as a function of output power for different laser technologies.	
	Single-mode fiber lasers show superior performance, maintaining diffraction	n-
	limited beam quality while scaling to higher powers. Adapted from	
	[1, 2]	18
2.2	Yb <sup>3+</sup> energy level structure, consisting of two manifolds: the ground	
	manifold $({}^2F_{7/2})$ with four Stark levels, and the higher excited man-	
	ifold $({}^2F_{5/2})$ with three Stark levels. Approximate energies in wave-	
	numbers above the ground energy are indicated on the left side	19

vi LIST OF FIGURES

2.3	Absorption and emission cross-sections of ytterbium-doped germanosilicate glass, as typically used in the cores of ytterbium-doped fibers	
	(data from spectroscopic measurements by R. Paschotta[3]	20
2.4	Simplified two-level energy diagram for ytterbium-doped fiber pumped	
	at 975 nm	21
2.5	Gain spectrum at different wavelengths for varying levels of relative	
	inversion	23
2.6	Simplified energy level diagram of a doped fiber showing pump absorp-	
	tion, stimulated emission (signal), and amplified spontaneous emission	
	(ASE)	24
2.7	Example of a Yb-doped fiber amplifier, adapted from [4]. The sim-	
	plified concepts of pump input $(P_p^{in})$ , seed input $(P_s^{in})$ , and output	
	powers $(P_s^{out}, P_p^{out})$ are clearly visible. The figure illustrates how	
	these basic concepts are implemented in a practical system, and how	
	more complex designs (multi-stage amplification, counter-pumping,	
	ASE management) build upon this fundamental scheme	26
2.8	Schematic of counter-pumped linear cavity fiber laser. The pump is	
	injected from the output side, while the forward $(P_s^+)$ and backward	
	$(P_s^-)$ propagating signal fields are reflected by the cavity mirrors with	
	reflectivities $R_1$ and $R_2$	27
2.9	Flowchart of the shooting method applied to boundary value prob-	
	lems. Flowchart of the shooting method applied to boundary value	
	problems. The boundary conditions are transformed into an initial	
	value formulation, integrated iteratively with a Runge-Kutta scheme,	
	and corrected until the desired accuracy is reached	29
3.1	Comparison between the Euler and Runge–Kutta 4th-order (RK4)	
	integration methods. The RK4 trajectory closely follows the true	
	solution.[5]	33
3.2	Flowchart summarizing the main script logic	35
3.3	Compact flowchart of the LaserPowerForward routine, showing iter-	
	ative forward/backward propagation with convergence check	36
3.4	Flowchart of LaserAmpForward, showing initialization of parameters	
	(with $n$ as max iterations), iterative RK4 loop, and storage of outputs.	37
3.5	Pump $(920\mathrm{nm})$ and signal $(1064\mathrm{nm})$ power evolution along the fiber	
	for a forward-pumped YDFA with input pump $10\mathrm{W.}$	39
3.6	Pump $(920\mathrm{nm})$ and signal $(1064\mathrm{nm})$ power evolution along the fiber	
	for a forward-pumped YDFL with input pump $10\mathrm{W.}$	39
3.7	Pump power along the fiber as $N_t$ varies ( $\pm 50\%$ relative to the nom-	
	inal value).	40

LIST OF FIGURES vii

3.8	Signal power along the fiber as $N_t$ varies ( $\pm 50\%$ relative to the nominal value)	41
3.9	Output signal power and residual pump at $L=2\mathrm{m}$ as $N_t$ varies $(\pm 50\%$ relative to the nominal value)	41
3.10	Pump power evolution along the fiber length for different values of $\tau_{21}$ .	42
	Signal power evolution along the fiber length for different values of $\tau_{21}$ .	42
3.12	Output signal power and residual pump at a fixed fiber length of 2 m,	
	for different values of $\tau_{21}$	43
3.13	Pump power evolution along the fiber length for different values of of	
	$\sigma_{ap}$ and $\sigma_{ep}$	44
3.14	Signal power evolution along the fiber length for different values of	
	$\sigma_{ap}$ and $\sigma_{ep}$	44
3.15	Output signal power and residual pump at a fixed fiber length of 2 m,	
	for varying $\sigma_{ap}$ (top) and varying $\sigma_{ep}$ (bottom)	45
3.16	Pump power evolution along the fiber for different values of $\sigma_{as}$ and	
	$\sigma_{es}$	46
3.17	Signal power evolution along the fiber for different values of $\sigma_{as}$ and	
	$\sigma_{es}$	46
3.18	Output signal power and residual pump at a fixed fiber length of $2\mathrm{m}$ ,	
	for varying $\sigma_{as}$ (top) and varying $\sigma_{es}$ (bottom)	47
3.19	Pump power evolution along the fiber for different combinations of $N_t$	
	and $\sigma_{as}$ keeping $\alpha$ constant	48
3.20	Signal power evolution along the fiber for different combinations of $N_t$	
	and $\sigma_{as}$ keeping $\alpha$ constant	48
3.21	Output signal power and residual pump at a fixed fiber length of $2\mathrm{m}$ ,	
	for varying $\sigma_{as}$ (top) and varying $N_t$ (bottom), while keeping $\alpha$ constant.	49
3.22	Pump power evolution along the fiber length for different values of $\sigma_{ap}$	
	and the corresponding recalculated $N_t$	50
3.23	Signal power evolution along the fiber length for different values of	
	$\sigma_{ap}$ and the corresponding recalculated $N_t$	50
3.24	Output signal power and residual pump at a fixed fiber length of $2\mathrm{m}$ ,	
	for varying $\sigma_{ap}$ (left) and varying $N_t$ (right)	51
3.25	Comparison of the spectroscopic parameters of the Nufern $10125\mathrm{DC}$	
	fiber as reported by different sources. The most significant variations	
	are observed for the dopant concentration $N_t$ , the absorption cross	
	section at the pump wavelength $\sigma_{ap}$ , and the emission cross section at	
	the signal wavelength $\sigma_{es}$ [6, 7, 8, 9, 10, 11]	52
3.26	Workflow of the MATLAB®-based fitting procedure: from data re-	
	trieval to error evaluation and parameter optimization	54

viii LIST OF FIGURES

3.27	Flowchart illustrating the operation of the Particle Swarm Optimiza- tion algorithm as applied to the parameter fitting of a doped fiber	
	laser.	56
3.28	Fitting results for $N_t$ : comparison of RP Fiber Power experimental	
0.20	data with theoretical and PSO-optimized simulated curves	58
3.29	Behavior of the function error during the optimization of $N_t$ . The	
	convergence is reached around $N_t^* = 4.02 \times 10^{25} \mathrm{m}^{-3}$	59
3.30	Fitting results for $\tau_{21}$ : comparison of RP Fiber Power experimental	
	data with theoretical and PSO-optimized simulated curves	60
3.31	Behavior of the SSE during the optimization of $\tau_{21}$ . The convergence	
	is reached around $\tau_{21}^* = 8.4 \times 10^{-4} \mathrm{s.}$	61
3.32	Fitting results for $\sigma_{as}$ : comparison of RP Fiber Power experimental	
	data with theoretical and PSO-optimized simulated curves	62
3.33	Fitting results for $\sigma_{es}$ : comparison of RP Fiber Power experimental	
	data with theoretical and PSO-optimized simulated curves	63
3.34	SSE behavior during the optimization of $\sigma_{as}$ . Convergence is reached	
	around $\sigma_{as}^* = 5.481 \times 10^{-27} \mathrm{m}^2$	63
3.35	SSE behavior during the optimization of $\sigma_{es}$ . The algorithm converges	
	to $\sigma_{es}^* = 2.877 \times 10^{-25} \mathrm{m}^2$	64
3.36	Fitting results for $\sigma_{ap}$ : comparison of RP Fiber Power experimental	
	data with theoretical and PSO-optimized simulated curves	65
3.37	Fitting results for $\sigma_{ep}$ : comparison of RP Fiber Power experimental	
	data with theoretical and PSO-optimized simulated curves	66
3.38	SSE behavior during the optimization of $\sigma_{ap}$ . The algorithm converges	
	perfectly to $\sigma_{ap}^* = 7.8 \times 10^{-25} \mathrm{m}^2$	66
3.39	SSE behavior during the optimization of $\sigma_{ep}$ . Convergence is reached	
	at $\sigma_{ep}^* = 4.8 \times 10^{-26} \mathrm{m}^2$	67
3.40	Fitting results for $N_t$ : comparison of RP Fiber Power reference data	
	with additive white Gaussian noise at a noise power of $-10\mathrm{dBW},$	
	along with theoretical and PSO-optimized simulated curves	68
3.41	Fitting results for $\tau_{21}$ :comparison of RP Fiber Power reference data	
	with additive white Gaussian noise at a noise power of $-10\mathrm{dBW},$	
	along with theoretical and PSO-optimized simulated curves	69
3.42	Fitting results for $\sigma_{as}$ :comparison of RP Fiber Power reference data	
	with additive white Gaussian noise at a noise power of $-10\mathrm{dBW},$	
	along with theoretical and PSO-optimized simulated curves	70
3.43	Fitting results for $\sigma_{es}$ :comparison of RP Fiber Power reference data	
	with additive white Gaussian noise at a noise power of $-10\mathrm{dBW},$	
	along with theoretical and PSO-optimized simulated curves	71

LIST OF FIGURES ix

3.44	Fitting results for $\sigma_{ap}$ :comparison of RP Fiber Power reference data with additive white Gaussian noise at a noise power of $-10 \mathrm{dBW}$ ,	
	along with theoretical and PSO-optimized simulated curves	72
3.45	Fitting results for $\sigma_{ep}$ : comparison of RP Fiber Power reference data	
	with additive white Gaussian noise at a noise power of $-10\mathrm{dBW},$	
	along with theoretical and PSO-optimized simulated curves	73
4.1	Schematic of the experimental setup. The main components are: pump diode (pump source), current supply (power supply), chiller and cold plate (Thermal management), active fiber (Yb-DC), high-reflectivity (HR) grating, output coupler (OC), dichroic mirror, collimating lens (plano-convex lens), and power meter (Thermal power	
	sensor).	77
4.2	Reflection spectrum of the HR grating, showing a peak attenuation of	
	about 9 dB	79
4.3	Reflection spectrum of the OC grating with reflectivity $R \approx 0.29$	
	$(\sim 1.5  \mathrm{dB}   \mathrm{attenuation})$	79
4.4	Reflection spectrum of the OC grating with reflectivity $R \approx 0.60$	
	$(\sim 4  dB  attenuation)$	80
4.5	Emission spectrum of the 25 m cavity with HR + Fresnel termination. The signal peak is visible around 1070 nm, while ASE appears at longer wavelengths	81
1 C		01
4.6	Emission spectrum of the 25 m cavity with HR + OC (R = 0.60). The ASE contribution is dominant relative to the signal peak	81
1 7	9 2	01
4.7	Emission spectrum of the 15 m cavity with HR + Fresnel termination (R $\approx 0.04$ ). The lasing peak is at 1070 nm	82
4.0	, , , , , , , , , , , , , , , , , , , ,	02
4.8	Emission spectrum of the 15 m cavity with HR + OC (R = 0.60). The	
	spectrum is dominated by the lasing line at 1070 nm, while the pump residual at 920 nm remains visible	82
1.0		02
4.9	Emission spectrum of the 10 m cavity terminated by HR + Fresnel	
	reflection (R $\approx$ 0.04). The lasing line at 1070 nm is accompanied by a residual pump peak at 920 nm	83
4.10		00
4.10	Emission spectrum of the 10 m cavity terminated by $HR + OC$ (R = 0.20). The leging line at 1070 nm is observed without significant number	
	0.29). The lasing line at 1070 nm is observed without significant pump residual	83
111		00
4.11	Emission spectrum of the $10 \mathrm{m}$ cavity terminated by HR + OC (R = $0.60$ ). The lasing emission at $1070 \mathrm{nm}$ coexists with the residual pump	
	at 920 nm	84
	αυ <i>θ</i> Δυ 11111	04

4.12	Emission spectrum of the 5 m cavity terminated by HR + Fresnel	
	reflection (R $\approx0.04).~$ A clean lasing line is observed at $1070\mathrm{nm},$	
	without pump or ASE	84
4.13	Emission spectrum of the 5 m cavity terminated by HR + OC (R = $$	
	0.29). The laser emission at $1070\mathrm{nm}$ is clearly visible without other	
	contributions	85
4.14	Emission spectrum of the $5\mathrm{m}$ cavity terminated by HR + OC (R =	
	0.60). The spectrum shows only the lasing emission at $1070\mathrm{nm}$	85
4.15	Comparison between experimental data and simulated model for $5\mathrm{m},$	
	R=0.04: (left) before and (right) after PSO optimization on splice	
	losses	88
4.16	Comparison between experimental data and simulated model for L=5 m,	
	R=0.29: (left) before and (right) after PSO optimization on splice	
	losses	88
4.17	Comparison between experimental data and simulated model for L=5 m,	
	R=0.60: (left) before and (right) after PSO optimization on splice	
	losses	89
4.18	Comparison between experimental data and simulated model for $10\mathrm{m},$	
	R=0.04: (left) before and (right) after PSO optimization on splice	
	losses	89
4.19	Comparison between experimental data and simulated model for L=10 m,	
	R=0.29: (left) before and (right) after PSO optimization on splice	
	losses	89
4.20	Comparison between experimental data and simulated model for L=10 m,	
	R=0.60: (left) before and (right) after PSO optimization on splice	
	losses	90
4.21	Comparison between experimental data and simulated model for $15\mathrm{m},$	
	R=0.04: (left) before and (right) after PSO optimization on splice	
	losses	90
4.22	Comparison between experimental data and simulated model for L=15 m,	
	R=0.60: (left) before and (right) after PSO optimization on splice	
	losses	91
4.23	Comparison between experimental data and simulated model for $25\mathrm{m},$	
	R=0.04: (left) before and (right) after PSO optimization on splice	
	losses.	91

# List of Tables

1.1	Summary of main limiting factors in high-power fiber lasers	13
2.1	Summary of main parameters used in rate and propagation equations.	21
4.1	Characterization of the pump diode module	86
4.2	Measured powers for the 25 m fiber samples	86
4.3	Measured powers for the 15 m fiber samples	87
4.4	Measured powers for the 10 m fiber samples	87
4.5	Measured powers for the 5 meter fiber samples	87

## Acronyms

ASE Amplified Spontaneous Emission. 10, 13, 78, 95

BVP Boundary Value Problem. 28

**CW** Continuous Wave. 20, 32, 38, 39

**DCF** Double-Clad Fiber. 3, 4, 9, 10, 14

**Er** Erbium. 37, 38

ESA Excited State Absorption. 13, 18, 19

FBG Fiber Bragg Grating. 4, 7–9

**FL** Fiber Laser. 3, 6–9, 11, 31

**FWM** Four-Wave Mixing. 12, 13

Ho Holmium. 37, 38

HR High-Reflectivity. 78, 88

IVP Initial Value Problem. 28

LASER Light Amplification by Stimulated Emission of Radiation. 3, 5–8, 11

**LD** Laser Diode. 3, 5

LMA Large Mode Area. 4, 7, 10

MI Modal Instability. 13

 $\mathbf{MMF}$  Multi-Mode Fiber. 7

MOPA Master Oscillator Power Amplifier. 14, 20

xiv Acronyms

NA Numerical Aperture. 6

Nd:YAG Neodymium-doped Yttrium Aluminum Garnet. 3, 18

OC Output Coupler. 78, 88

PCF Photonic Crystal Fiber. 11

**PSO** Particle Swarm Optimization. 53, 55–58, 62, 65, 67

**RE** Rare Earth. xiv, 40

**REDFL** Rare-Earth-Doped Fiber Laser. 4, 5, 7

RK4 Runge-Kutta Fourth-Order method. vi, 32, 33, 37, 38

SBS Stimulated Brillouin Scattering. 10, 12

**SMF** Single-Mode Fiber. 7

**SPM** Self-Phase Modulation. 12, 13

SRS Stimulated Raman Scattering. 10, 12

**SSE** Sum of Squared Errors. viii, 53, 56, 57, 61, 63, 64, 66, 67

SSL Solid State Laser. 3, 8

**Tm** Thulium. 37, 38

XPM Cross-Phase Modulation. 12

 $Yb^{3+}$  Ytterbium ion. 4, 17–19, 25, 95

YbEr Ytterbium-Erbium. 37, 38

**YDF** Rare Earth (RE)-Doped Fiber. 40, 57

YDFA Ytterbium-Doped Fiber Amplifier. vi, 32, 38–40, 78

YDFL Ytterbium-Doped Fiber Laser. vi, 4, 17, 18, 38–40, 53, 95, 96

## Introduction

Fiber lasers are among the most widely adopted laser sources today, particularly in high-power applications, owing to their unique combination of high efficiency, mechanical robustness, and excellent beam quality. Achieving such performance, however, requires careful optimization of the laser design, which in turn depends on reliable simulation tools capable of accurately predicting power evolution along the fiber and evaluating how the internal cavity parameters influence the overall performance.

A significant challenge arises from the lack of information on the internal parameters of fibers, such as emission and absorption cross sections or dopant concentration, which are rarely reported in manufacturers' datasheets. The availability of accurate physical models, calibrated against experimental data, is therefore essential to understand internal dynamics, diagnose laser behavior, and guide design and optimization strategies based on reliable information.

The work presented in this thesis addresses this challenge by proposing a methodology for retrieving the internal parameters of active fibers, demonstrating that it is possible to obtain reliable information from a limited set of experimental data. The developed model was also validated on a high-power ytterbium-doped double-clad fiber, showing good agreement between simulations and experimental measurements and confirming the robustness and reliability of the approach.

To fully understand the foundations of this work, the study begins with an analysis of the fundamental characteristics of optical fibers and the physical phenomena that govern their operation. This theoretical understanding provides the basis for the methodological choices adopted and clarifies how the developed approach can be effectively applied for the analysis, simulation, and optimization of high-power fiber lasers.

## Chapter 1

## Overview on the State of the Art

#### 1.1 Historical Background on Rare-Earth-Doped Fiber Lasers

The foundational principle behind laser technology, namely stimulated emission, was theoretically introduced by Albert Einstein in 1917 [12]. This quantum mechanical phenomenon paved the way for the idea that electromagnetic radiation could be amplified by exciting atoms or ions into higher energy states and then triggering their emission coherently. However, it was not until 1960 that the first practical realization of a device exploiting Light Amplification by Stimulated Emission of Radiation (LASER) was achieved by Theodore H. Maiman using a ruby crystal [13]. Just a year later, in 1961, Elias Snitzer proposed using optical fibers as gain media for LASER systems, initiating the era of Fiber Laser (FL)s [14]. Although the early designs were limited by technological challenges – especially in coupling pump light into the fiber core and managing material losses – the principle of fiber-based amplification was firmly established.

In 1964, Geusic, Marcus, and Van Uitert from Bell Labs demonstrated the first operational Solid State Laser (SSL) based on neodymium-doped yttrium aluminum garnet (Neodymium-doped Yttrium Aluminum Garnet (Nd:YAG)), pumped with a tungsten lamp to produce emission at 1064 nm [15]. This achievement marked a major milestone in solid-state laser technology, paving the way for the subsequent development of rare-earth-doped gain media, including the glass-based and fiber-based systems that would emerge in the following decades.

A significant breakthrough came with the introduction of the Double-Clad Fiber (DCF) architecture. Initially conceived in the 1970s and practically implemented in 1988 by Snitzer et al., this design allowed high-power, multimode pump light to be coupled into an inner cladding surrounding a single-mode core [16]. This innovation enabled the use of powerful but low-beam-quality Laser Diode (LD) as pump sources,

while preserving the excellent beam quality of single-mode output.

The first single-mode continuous-wave fiber laser was demonstrated in 1985 by Mears et al., utilizing improved silica fiber fabrication and single-mode diode pumping techniques [17]. These technological advances laid the foundation for modern Rare-Earth-Doped Fiber Laser (REDFL) systems.

Among various rare-earth dopants, Ytterbium ion (Yb<sup>3+</sup>) emerged as one of the most promising for high-power applications due to its simplified electronic structure. Hanna et al. in 1988 demonstrated one of the first Ytterbium-Doped Fiber Laser (YDFL)s, highlighting a broad tunability from from 1.015 µm to 1.4 µm when pumped with a dye laser at 840 nm [18]. Ytterbium's two-level-like energy diagram minimizes non-radiative losses, allowing for high slope efficiency and reduced thermal effects [3, 12].

The 1990s and 2000s saw an exponential rise in output power levels of YDFLs, driven by advances in DCF designs, high-power diode pumping, and passive fiber components like Fiber Bragg Grating (FBG)s. Noteworthy demonstrations include:

- Dominic et al. (1999): 110 W output with a rectangular-cladding YDFL pumped at 915 nm [19];
- Barannikov et al. (2004): 250 W linearly polarized YDFL using a master oscillator and amplifier configuration [20];
- Khitrov et al. (2004): 306 W fully fiber-integrated linearly polarized YDFL with FBGs and coiled Large Mode Area (LMA) fiber [21];
- Jeong et al. (2004): systems producing 610 W and later 1.36 kW of output with slope efficiencies up to 83%, using D-shaped claddings and optimized pump coupling [22, 23].

The adoption of non-circular cladding geometries (e.g., octagonal, D-shaped, offset-core) further improved pump absorption efficiency, enabling better overlap of pump light with the doped core region [24].

These milestones demonstrate the evolution of fiber laser technology from theoretical models to highly efficient, compact, and robust systems capable of delivering kilowatt-class powers with diffraction-limited beam quality. The integration of fiber-based components also eliminates the need for free-space optics, improving alignment stability and environmental resilience.

In summary, the historical development of REDFL is a testament to the synergy between material science, photonic design, and laser engineering. YDFLs in particular exemplify the ideal platform for high-power applications, combining efficiency, simplicity, and scalability.

#### 1.2 Fiber Lasers and Their Principles of Operation

Fiber lasers are a class of laser sources that combine the coherence and brightness typical of lasers with the inherent advantages of optical fiber waveguides. As in other lasers, the principles of their operation are rooted in fundamental light–matter interactions, namely: absorption, spontaneous emission, and stimulated emission. In this section, we explore these processes and trace the development of REDFL and amplifiers, emphasizing the innovations that made high-power operation possible.

Consider an atomic or molecular medium whose electrons initially reside in a lower energy state  $E_1$ . When a photon of frequency  $\nu$  and energy

$$E = h\nu = E_2 - E_1, \tag{1.1}$$

is absorbed, an electron is excited to a higher energy level  $E_2$ . This is the process of absorption. The electron can then return to the ground state either spontaneously, emitting a photon in a random direction and phase, or via *stimulated emission*, in which another incident photon induces the decay with the consequent release of a new photon with the same phase, direction, frequency, and polarization.

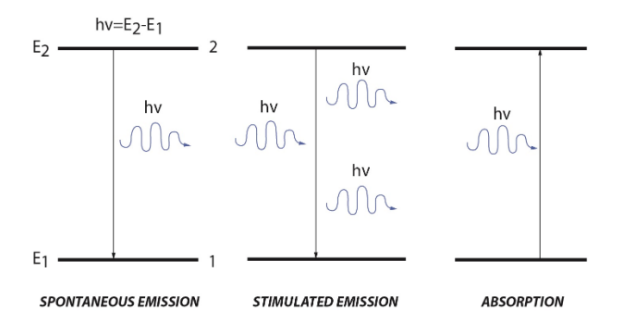


Figure 1.1: Fundamental light-matter interactions: (1) spontaneous emission, (2) stimulated emission, and (3) absorption.

These three fundamental processes: absorption, spontaneous emission, and stimulated emission, are illustrated in Fig. 1.1. Population inversion, a condition where more electrons occupy the excited state  $E_2$  than the ground state  $E_1$ , is necessary for net amplification of light via stimulated emission, forming the basis for LASER operation. In conventional solid-state LASERs, such as rod LASERs, the gain medium is a crystal or glass doped with rare-earth ions. Pump sources (e.g., LDs or flash-lamps) provide the energy to achieve population inversion, and a pair of mirrors forms a resonant cavity to amplify the stimulated emission. However, such systems face limitations at high power levels due to thermal lensing, stress-induced birefringence, and lack of efficient optical confinement [25].

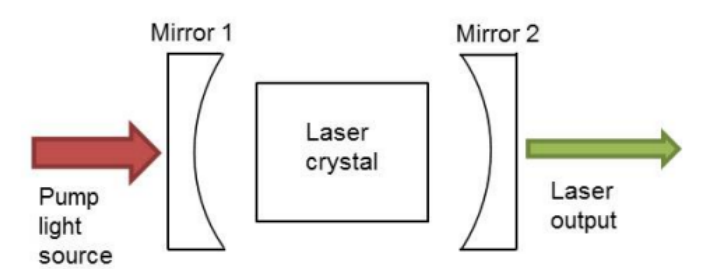


Figure 1.2: Schematic of a conventional solid-state laser with mirror-based cavity.

Fig. 1.2 shows the structure of a typical solid-state LASER setup using mirrors to form a resonant cavity.

FLs exploit the efficient confinement and guidance of light within the fiber core. The simplest form of an optical fiber consists of a central core with refractive index  $n_1$ , surrounded by a cladding with a slightly lower refractive index  $n_2$  ( $n_1 > n_2$ ). This refractive index difference makes total internal reflection (TIR) at the core-cladding interface possible, one the essential conditions to allow trapping the light beam within the core as it propagates along the fiber length [26]. Indeed, when a light ray traveling inside the core hits the core-cladding interface at an angle  $\theta_i$  (measured from the normal to the interface) greater than the critical angle  $\theta_c$ , defined by

$$\theta_{\rm c} = \arcsin\left(\frac{n_2}{n_1}\right),$$

the ray is totally internally reflected back into the core, preventing leakage into the cladding. The range of angles within the core that can be in TIR conditions depends on the fiber's numerical aperture (Numerical Aperture (NA)):

$$NA = \sqrt{n_1^2 - n_2^2},$$

which defines the maximum acceptance angle  $\theta_a$  at the fiber input, through

$$\sin \theta_a = NA$$
.

Light entering the fiber within this acceptance cone will be subject to total internal reflections.

In addition to satisfying the TIR condition, guided modes must also meet a phase-matching requirement: after each reflection at the core-cladding interface, the optical field must reproduce itself in phase to allow constructive interference along the propagation direction. This leads to discrete propagation constants  $\beta_{\rm m}$  associated with the allowed modes of the waveguide, as determined by solving Maxwell's equations with the appropriate boundary conditions. The interplay between the TIR criterion

and the phase condition defines the set of modes that can propagate in the fiber.

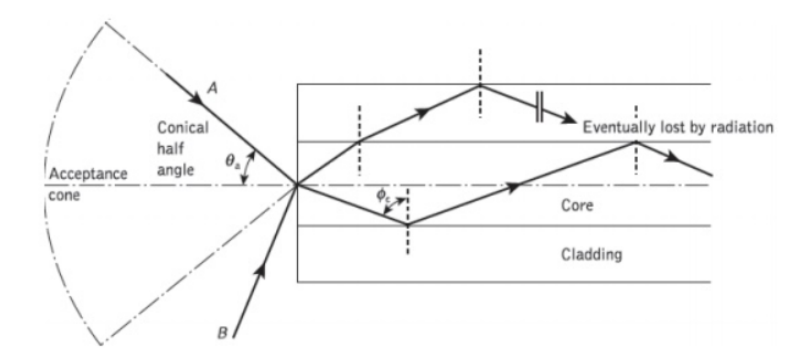


Figure 1.3: Schematic of the fiber indicating the core, cladding, critical angle, and trajectory of a guided ray.

Fig. 1.3 visually explains how total internal reflection confines light in the fiber. For Single-Mode Fiber (SMF)s, only the fundamental mode propagates. In this condition the core diameter d and NA satisfy the V-number condition:

$$V = \frac{2\pi a}{\lambda} \, \text{NA} < 2.405,$$

where V is the normalized frequency, a=d/2 is the core radius and  $\lambda$  the wavelength in vacuum. This ensures single-mode operation with excellent beam quality, important for high-performance FLs.

For Multi-Mode Fiber (MMF) or LMA fibers, V is larger, supporting multiple modes, and special design is required to maintain a good-enough beam quality.

The use of fibers as LASER media dates back to the mid-20th century. In 1954, Heel studied light guidance in glass and plastic fibers through total internal reflection [26]. By 1961, Snitzer proposed utilizing fiber waveguides as LASER cavities [14], and by 1964, REDFL were used in the first FLs and amplifiers.

Early devices suffered from high optical losses and limited pump sources, with typical fibers having core diameters of a few microns and lengths of under two meters. A typical FL consists of an optical fiber doped with rare-earth ions, bounded by mirrors or FBGs forming a resonator. FBGs are periodic variations of the refractive index inscribed along the fiber core, acting as wavelength-selective mirrors that reflect specific wavelengths while transmitting others, enabling compact and robust cavity designs without free-space optics [27].

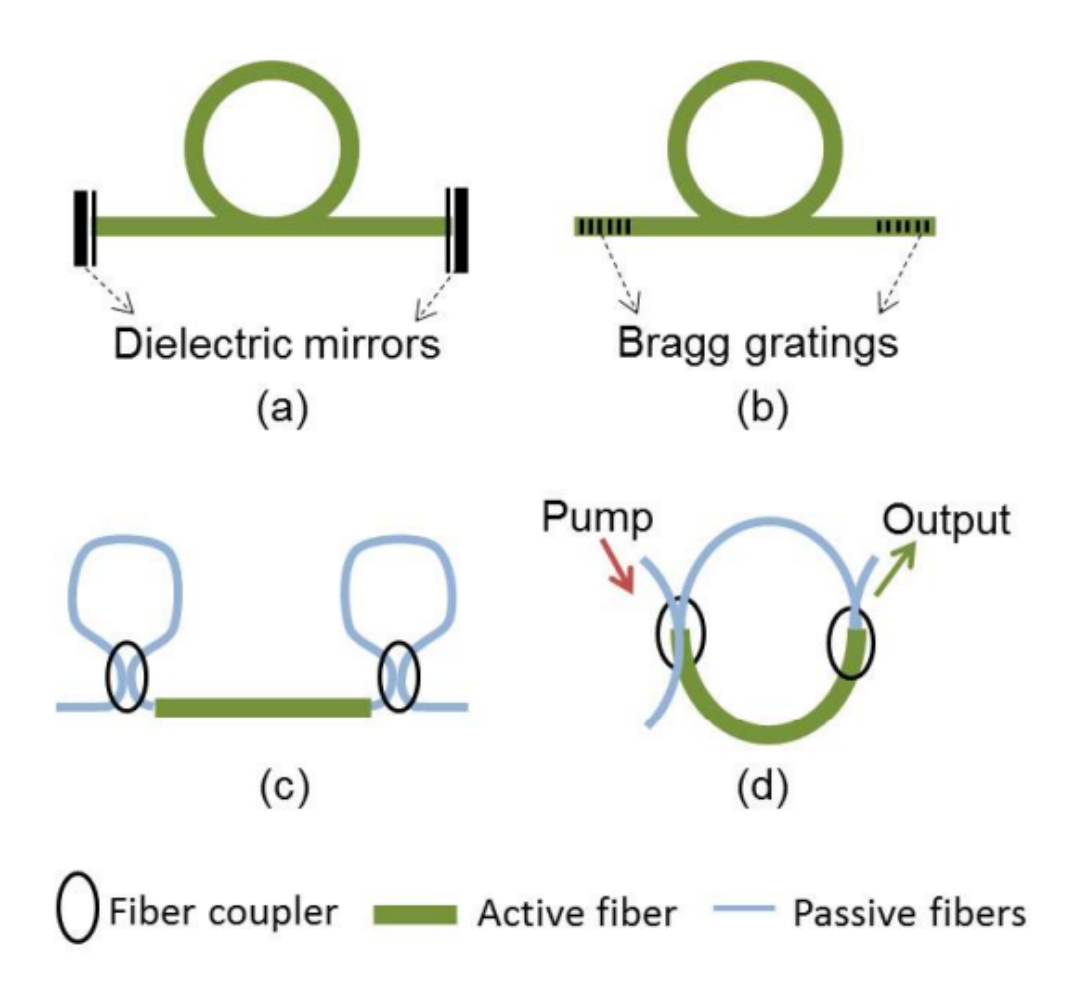


Figure 1.4: Schematics of different laser resonator cavities: (a) dielectric mirrors, (b) Bragg gratings, (c) Sagnac loop, and (d) ring cavity laser.

Fig. 1.4 illustrates schematics of different LASER resonator cavities commonly used in FLs: (a) linear cavity with dielectric mirrors, (b) linear cavity with FBGs, (c) Sagnac loop, and (d) ring cavity LASERs, where it compares the different configurations used to form laser cavities inside fibers. The pump and signal light are confined in the fiber core via total internal reflection, resulting in excellent spatial overlap and high gain. Compared to traditional SSL, FLs offer several intrinsic advantages arising from the waveguide geometry: the large surface-to-volume ratio ensures efficient heat dissipation, reducing thermal distortions and preserving beam quality; the monolithic fiber geometry provides compactness, mechanical robustness, and permanent alignment, eliminating the need for free-space optics. Furthermore, light confinement within the fiber enables excellent mode quality even at high output powers, while also delivering higher optical-to-optical conversion efficiencies than conventional SSL [28, 29]. The detailed physics of the ion excitation, energy levels, and population dynamics are discussed in the following section. FLs are classified ac-

cording to cavity configuration: linear cavities (formed by dielectric mirrors, FBGs, or Sagnac loops) and ring cavities offering unidirectional feedback using couplers [28]. These configurations influence the feedback dynamics and output coupling.

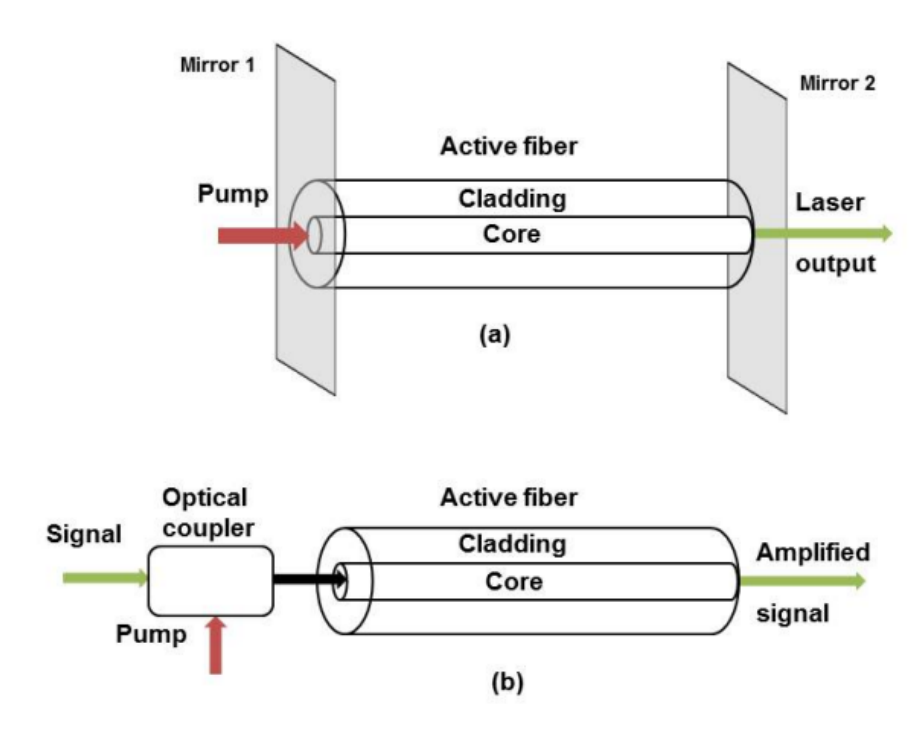


Figure 1.5: Schematic of (a) End-pumped linear-cavity fiber laser and (b) Co-pumped fiber amplifier.

Fig. 1.5 depicts different fiber laser and amplifier pumping setups. Pumping schemes vary: end-pumping, side-pumping, and V-groove side-pumping are used depending on how the pump light couples into the fiber. The pumping directions can be co-directional, counter-directional, or bidirectional relative to the seed beam. Optical isolators are employed to prevent harmful back-reflections [29]. While single-clad fibers provide high gain, output power is limited by the pump power that can be delivered through single-mode diodes. High-power diode sources tend to be multimode and cannot couple efficiently into narrow fiber cores. This challenge led to the development of DCF, first proposed by Snitzer in 1988 [16]. In a DCF, the pump light is coupled into a large inner cladding surrounding the single-mode doped core. The cladding guides multimode pump light, which is absorbed by the core as it propagates, enabling efficient energy transfer from high-power multimode sources. This cladding-pumped design revolutionized high-power FL development.

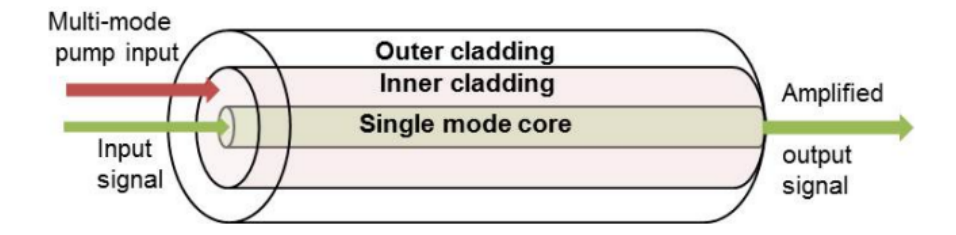


Figure 1.6: Schematic of a cladding-pumped double-clad fiber amplifier.

Fig. 1.6 shows how DCF structures enable absorption of multimode pump light in high-power applications. To improve absorption efficiency, inner cladding shapes such as octagonal, square, or D-shaped geometries have been proposed to enhance mode scrambling and pump-core interaction [1].

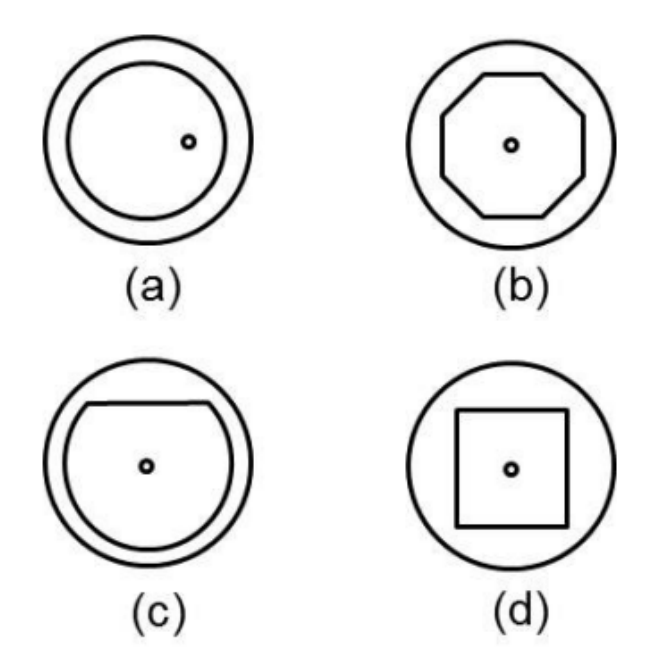


Figure 1.7: Different fiber inner cladding and core geometries used to increase pump absorption: (a) offset core fiber, (b) octagonal inner cladding, (c) "D"-shaped inner cladding, (d) square inner cladding.

Fig. 1.7 highlights how different fiber shapes enhance pump absorption efficiency. As power levels increased, nonlinear optical effects such as Amplified Spontaneous Emission (ASE), Stimulated Raman Scattering (SRS), and Stimulated Brillouin Scattering (SBS) and thermal issues became limiting factors. To mitigate these, LMA fibers were introduced, increasing the core size while maintaining single-mode guidance to reduce optical intensities and nonlinearities [30]. An elegant advancement was the

introduction of Photonic Crystal Fiber (PCF)s by P. St. J. Russell in the 1990s [31]. PCFs feature a periodic array of air holes around the core to control light guidance via photonic bandgap or modified total internal reflection, enabling large core areas with controlled single-mode operation.

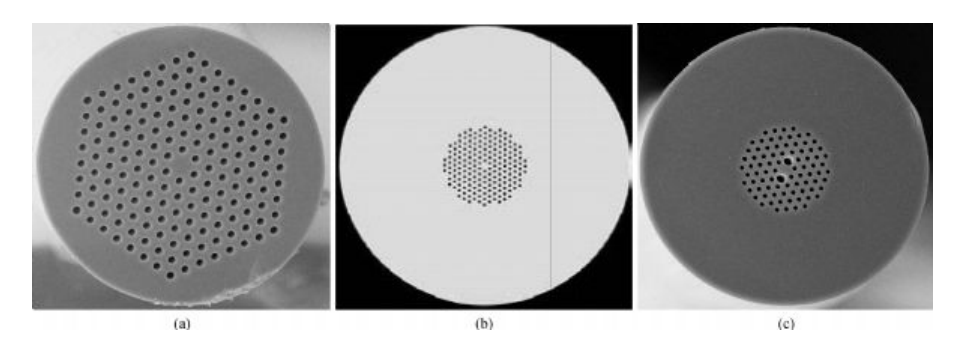


Figure 1.8: (a) Endlessly single mode PCF; (b) highly nonlinear PCF; (c) Hi-Bi PCF.

Figure 1.8 shows examples of different PCF designs: (a) endlessly single-mode PCF, (b) highly nonlinear PCF, and (c) high-birefringence (Hi-Bi) PCF, each optimized for specific performance characteristics and applications. The combination of cladding-pumped schemes and PCFs has led to FLs with output powers exceeding kilowatts, suitable for industrial, medical, and defense applications. Nevertheless, challenges such as thermal lensing, modal instabilities, and nonlinear scattering remain areas of active research [2]. In summary, FLs represent the integration of quantum principles of light-matter interaction with advanced photonic engineering. For a detailed treatment of the physical processes governing ion excitation and LASER efficiency, see the dedicated section on population dynamics and quantum efficiency.

# 1.3 Limiting Factors and Challenges in High-Power Fiber Lasers

Despite the numerous advantages of ytterbium-doped fiber lasers, especially in high-power applications, their performance is inherently limited by various physical effects. These effects originate from both the quantum nature of light-matter interaction and the specific geometry of fiber structures.

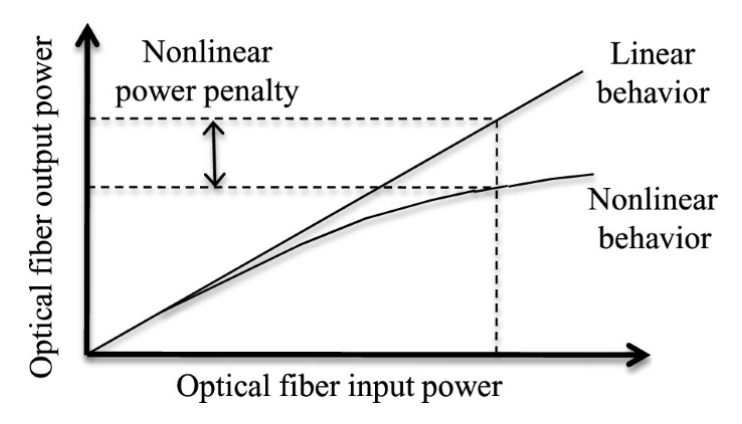


Figure 1.9: Conceptual diagram showing the increase of nonlinear effects with higher input power in an optical fiber.

Fig. 1.9 highlights the increase in nonlinear effects with rising input power, which poses a major limitation in high-power fiber laser systems.

#### 1.3.1 Nonlinear Effects in High-Power Operation

The long interaction length in fibers, combined with strong optical confinement in the small core area, results in high optical intensities. These conditions give rise to several third-order nonlinear effects  $(\chi^{(3)})$ , such as:

- Self-phase modulation (Self-Phase Modulation (SPM))
- Cross-phase modulation (Cross-Phase Modulation (XPM))
- Four-wave mixing (Four-Wave Mixing (FWM))
- Stimulated Raman Scattering (SRS)
- Stimulated Brillouin Scattering (SBS)
- Kerr effect

While these effects can be harnessed for specific applications — such as supercontinuum generation — they are usually detrimental in the context of high-power fiber

lasers, where they can cause pulse distortion, beam quality degradation, or even fiber damage [32].

#### 1.3.2 Thermal Effects and Modal Instabilities

At high powers, thermal effects in the fiber become non-negligible. The absorption of pump and signal light generates heat, leading to temperature gradients in the fiber. These gradients induce refractive index changes via the thermo-optic effect, causing modal instabilities (Modal Instability (MI)), which can transfer energy from the fundamental mode to higher-order modes.

Modal instabilities can result in temporal fluctuations in beam quality and limit the scalability of power [33].

#### 1.3.3 Design Trade-offs and Mitigation Strategies

Mitigating these limiting factors requires a careful balance between fiber geometry, doping concentration, core/cladding ratio, and pumping configuration. For instance, increasing the mode area reduces nonlinear effects but may worsen modal instability due to multi-mode operation. Similarly, optimizing the fiber length can help limit ASE but may reduce gain.

ASE, or Amplified Spontaneous Emission, is a broadband noise generated by the spontaneous emission of dopant ions that is subsequently amplified along the fiber. It propagates both in the forward and backward directions, competing with the signal for the available gain and potentially leading to gain saturation and power depletion. The strength of ASE depends on factors such as the dopant concentration, fiber length, pump power, and the spectral properties of the fiber. If not properly managed, ASE can severely limit the achievable output power and efficiency, especially in high-gain or long-fiber configurations.

Fiber design innovations, such as photonic crystal fibers, chirally coupled core fibers, and specialty double-clad geometries, are ongoing attempts to overcome these challenges. Table 1.1 provides an overview of the primary limiting factors in high-power fiber lasers and their corresponding effects on performance.

Limiting Factor	Effect on Performance		
ASE	Reduces gain and adds noise		
Excited State Absorption (ESA)	Decreases efficiency via loss of inversion		
Nonlinear effects (SPM, FWM, etc.)	Distortion, spectral broadening, damage		
Thermal effects	Modal instabilities, degradation of beam quality		

#### 1.4 High Power Laser Application

High-power fiber lasers represent one of the most significant and versatile technologies in today's scientific and industrial landscape. Their evolution, driven by the growing need for compact, efficient, and reliable light sources, has led to the development of devices capable of delivering kilowatt-level output powers while maintaining excellent beam quality and long-term operational stability [3, 12].

This technological transition did not occur in isolation, but has been intertwined with innovations in materials, fiber design, and control electronics. These advancements have enabled the overcoming of historical limitations related to heating, beam distortion, and optical cavity instabilities. In particular, the introduction of DCF allowed the separation of pump and signal paths, enabling the efficient injection of high-power multimode diode light into the cladding while preserving single-mode propagation in the core [16].

The Master Oscillator Power Amplifier (MOPA) (Master Oscillator Power Amplifier) architecture further solidified the concept of modular and scalable fiber laser sources. By separating signal generation from amplification, each stage could be optimized for specific performance targets, such as pulse shape, polarization, or spectral width. This architecture has become dominant in nearly all applications that require high brightness and precise control over temporal or spectral characteristics [17].

In the industrial domain, high-power fiber lasers have become the preferred tool for a wide range of processing tasks. Cutting, welding, cladding, hardening, and metal 3D printing are just a few examples where these lasers have successfully replaced bulkier, less efficient, or less precise technologies. Their ability to concentrate optical energy into extremely small areas allows for high-precision machining with minimal thermal damage, improving product quality and reducing post-processing costs [22, 23].

In the medical field, the miniaturization and flexibility of fiber systems have made ytterbium-doped fiber lasers ideal for surgical and therapeutic applications. In laser surgery, for example, they enable highly precise, minimally invasive procedures with shorter recovery times. Moreover, their compatibility with extremely thin optical fibers facilitates the design of endoscopic or catheter-based laser instruments for deep or hard-to-reach anatomical targets [18].

Equally significant is the role of fiber lasers in the defense sector. With growing interest in directed energy weapons, high-power lasers offer concrete solutions for counter-drone, anti-missile, and optical countermeasure systems. In these scenarios, the compactness and efficiency of fiber lasers are crucial for deployment on mobile platforms, while their intrinsic robustness ensures reliable operation in harsh environments [20, 21].

In scientific research, fiber lasers are a preferred platform for studies in nonlinear optics, spectroscopy, supercontinuum generation, and optical metrology. Their ability to deliver high-repetition-rate ultrashort pulses with precise temporal shaping has opened new frontiers in ultrafast science, matter interaction studies, and extreme frequency generation [17].

Despite the progress, the development of high-power fiber lasers continues to face significant challenges. Phenomena such as stimulated Brillouin and Raman scattering, thermal management in large-mode-area fibers, and polarization maintenance at high powers remain active fields of research. Solutions include innovative fiber geometries, advanced cooling techniques, and the use of novel materials or photonic crystal structures [24].

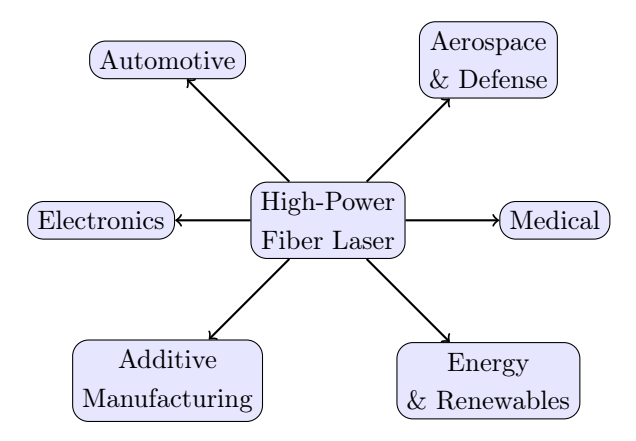


Figure 1.10: Main application sectors of high-power fiber lasers: automotive, aerospace and defense, electronics, medical, additive manufacturing, and energy/renewables.

Fig. 1.10 shows the main application sectors of high-power fiber lasers.

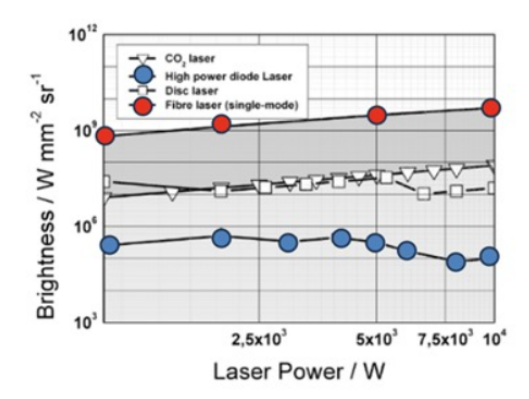
In conclusion, high-power fiber lasers are not merely technical tools of great relevance: they embody a photonic paradigm that integrates efficiency, scalability, and precision. Their ongoing development and adaptability to diverse applications confirm their role as undisputed protagonists in the ongoing optoelectronic revolution.

# Chapter 2

# Theoretical Framework for Ytterbium-Doped Fiber Systems

This chapter presents the theoretical framework necessary to understand the behavior of ytterbium-doped fiber devices. The objective is to provide a solid basis for the simulation and experimental analysis in the following chapters, starting from the spectroscopic properties of the Yb<sup>3+</sup> ion and leading to the formulation of the rate equations, which are fundamental to model population dynamics and power propagation along the fiber. This section draws inspiration from the main works in the literature [12, 32, 33] and from the established experience in the design and simulation of YDFL systems.

Before delving into the spectroscopic properties, it is useful to observe the comparative performance of different high-power laser technologies. In particular, two of the most relevant figures of merit are the beam brightness and the beam parameter product (BPP), which jointly determine the efficiency and the applicability of the source in demanding scenarios such as material processing.



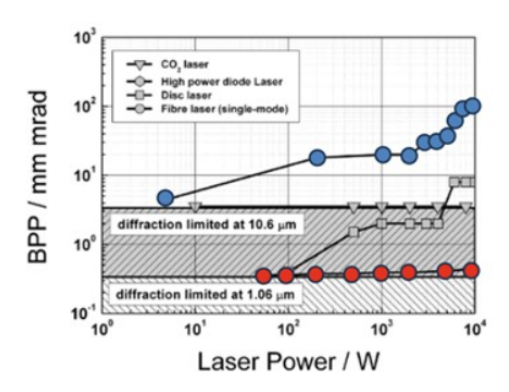


Figure 2.1: Comparison of brightness (left) and beam parameter product (BPP, right) as a function of output power for different laser technologies. Single-mode fiber lasers show superior performance, maintaining diffraction-limited beam quality while scaling to higher powers. Adapted from [1, 2].

Fig. 2.1 illustrates the evolution of these parameters as a function of the laser output power for various architectures, namely CO<sub>2</sub> lasers, high-power diode lasers, disc lasers, and single-mode fiber lasers. It is evident that fiber lasers, especially those based on Yb<sup>3+</sup>, stand out for their ability to combine high output power with excellent beam quality, operating close to the diffraction limit at 1070 nm. This combination explains their widespread adoption and continuous development compared to other solid-state laser platforms [1, 2].

# 2.1 Ytterbium-doped gain media

The rapid development of high-power fiber lasers has been driven by the favorable spectroscopic properties of the Yb<sup>3+</sup> ion, which has gradually replaced other dopants such as neodymium and erbium, used in Nd:YAG solid-state lasers and erbium-doped fiber lasers, respectively. Although the first YDFL was demonstrated as early as in 1988 [16], it only became the preferred solution in subsequent years, initially overshadowed by the widespread use of other rare-earth ions [17, 34]. For instance, neodymium-doped active materials, such as YAG or silica fibers, are particularly attractive because they exhibit four-level behavior, which facilitates lasing with emission around 1060 nm when pumped at 800 nm. In contrast, erbium-doped fibers, while exhibiting a more challenging three-level behavior, dominate telecommunication applications due to emission in the 1520 nm to 1600 nm range, corresponding to the third optical communication window, and the possibility of pumping over a wide wavelength range (510 nm to 1480 nm). However, intrinsic limitations, such as ESA in erbium fibers and the reduced spectral width in neodymium fibers, have

constrained their further development [3].

In contrast, Yb<sup>3+</sup> offers a simple and highly efficient electronic structure for optical amplification, consisting of only two energy manifolds: the ground state  ${}^2F_{7/2}$  and the excited state  ${}^2F_{5/2}$ , separated by a relatively small energy gap. This configuration results in a low *quantum defect*, which reduces thermal losses, enhances efficiency, and minimizes detrimental processes such as quenching and ESA.

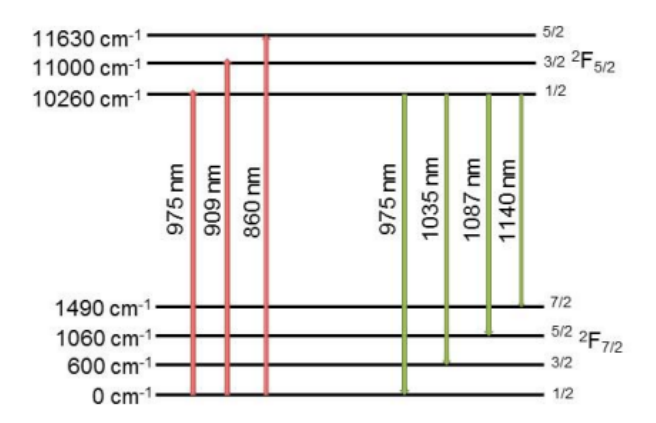


Figure 2.2: Yb<sup>3+</sup> energy level structure, consisting of two manifolds: the ground manifold ( ${}^2F_{7/2}$ ) with four Stark levels, and the higher excited manifold ( ${}^2F_{5/2}$ ) with three Stark levels. Approximate energies in wave-numbers above the ground energy are indicated on the left side.

Figure 2.2 shows the energy level structure of  $Yb^{3+}$ .

Spectrally, ytterbium-doped fibers show quasi-three-level behavior at wavelengths below 1080 nm, where the laser transition approaches the ground state, causing reabsorption and higher threshold powers, and four-level behavior at longer wavelengths, where population inversion is easier to achieve [3]. The absorption and emission cross sections are influenced by the host glass: germanosilicate is the most commonly used core material [3]. The main absorption bands are around 910 nm (broad but less intense) and 975 nm (narrow and highly efficient), while the useful emission extends from about 1000 nm to beyond 1100 nm, with resonant peaks for pumping and high-power amplification.

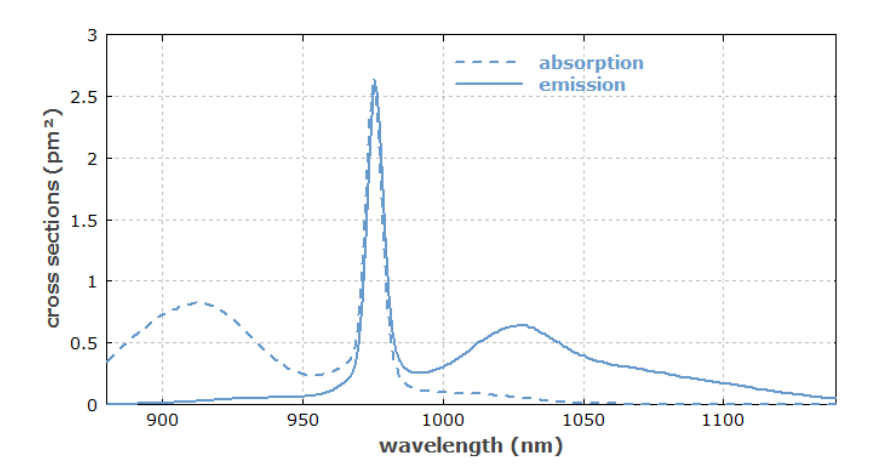


Figure 2.3: Absorption and emission cross-sections of ytterbium-doped germanosilicate glass, as typically used in the cores of ytterbium-doped fibers (data from spectroscopic measurements by R. Paschotta[3].

As shown in Figure 2.3, the main absorption and emission bands determine the optimal pumping and amplification wavelengths. Despite some challenges, such as pronounced at 975 nm and potential quenching phenomena, ytterbium-doped fibers combine high efficiency, wide gain bandwidth, and robustness, making them ideal for Continuous Wave (CW), MOPA, and ultrashort pulse systems.

# 2.2 Rate and Propagation Equations

Building on the spectroscopic considerations introduced in the previous section, the quantitative description of light–matter interaction in ytterbium-doped fiber devices is conventionally formulated in terms of the *rate equations* and propagation equations. These are established tools in the literature for modeling and analyzing fiber lasers and amplifiers. The dynamic behavior of these systems can be effectively represented by a reduced two-level model due to the fast non-radiative relaxation to the metastable state [3].

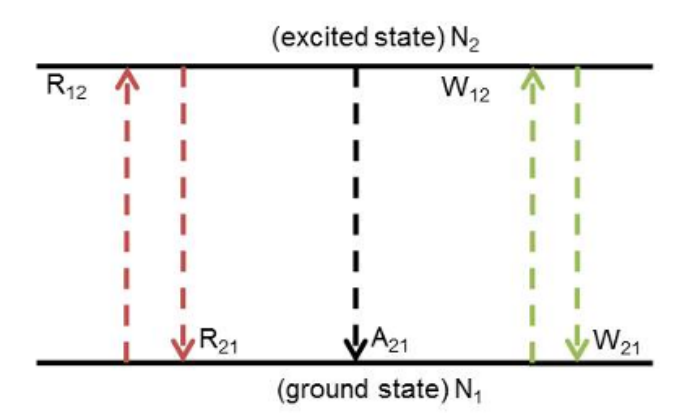


Figure 2.4: Simplified two-level energy diagram for ytterbium-doped fiber pumped at  $975\,\mathrm{nm}$ .

When pumped near 975 nm, the active medium can be approximated as shown in Figure 2.4. Before analyzing the rate and propagation equations, Table 2.1 summarizes the parameters and symbols used throughout this section.

Table 2.1: Summary of main parameters used in rate and propagation equations.

Symbol	Description	Units
$n_1, n_2$	Normalized populations (ground, excited)	_
$R_{12}, R_{21}$	Pump absorption and stimulated emission rates	$s^{-1}$
$W_{12}, W_{21}$	Signal absorption and stimulated emission rates	$s^{-1}$
$A_{21}$	Spontaneous decay rate $(1/\tau_{21})$	$s^{-1}$
$\sigma_{ap},\sigma_{ep}$	Pump absorption and emission cross sections	$m^2$
$\sigma_{as},\sigma_{es}$	Signal absorption and emission cross sections	$m^2$
$I_p, I_s$	Pump and signal intensities	$W \cdot m^{-2}$
$h\nu_p, h\nu_s$	Photon energies	J
$N_t$	Total active ion concentration	$\mathrm{m}^{-3}$
$\Gamma_p, \Gamma_s$	Pump/signal overlap factors	_
$R_1, R_2$	Reflectivities of cavity mirrors	_
g(z)	Local gain coefficient	$\mathrm{m}^{-1}$
RI	Relative inversion $(n_2 - n_1)$	_
$P_{sat,p}, P_{sat,s}$	Pump/signal saturation powers	W
$A_{eff}$	Effective core area	$m^2$

The normalized populations  $n_1$  and  $n_2$  of the ground and excited states are governed

by the local rate equations:

$$\frac{dn_2}{dt} = (R_{12} + W_{12})n_1 - (R_{21} + W_{21} + A_{21})n_2, \tag{2.1}$$

$$\frac{dn_1}{dt} = (R_{12} + W_{12})n_1 + (R_{21} + W_{21} + A_{21})n_2. \tag{2.3}$$

Since the total population is conserved,

$$n_1 + n_2 = 1. (2.4)$$

Under steady-state conditions  $(dn_i/dt = 0)$ , one obtains:

$$n_1 = \frac{R_{21} + W_{21} + A_{21}}{R_{12} + R_{21} + W_{12} + W_{21} + A_{21}},$$
(2.5)

$$n_{1} = \frac{R_{21} + W_{21} + A_{21}}{R_{12} + R_{21} + W_{12} + W_{21} + A_{21}},$$

$$n_{2} = \frac{R_{12} + W_{12}}{R_{12} + R_{21} + W_{12} + W_{21} + A_{21}}.$$
(2.5)

The transition rates depend on the absorption and emission cross sections, as well as on pump and signal intensities:

$$R_{12} = \frac{\sigma_{ap}I_p}{h\nu_p}, W_{12} = \frac{\sigma_{as}I_s}{h\nu_s}, (2.7-2.8)$$

$$R_{21} = \frac{\sigma_{ep}I_p}{h\nu_p}, W_{21} = \frac{\sigma_{es}I_s}{h\nu_s}, (2.7-2.8)$$

$$R_{21} = \frac{\sigma_{ep}I_p}{h\nu_p},$$
  $W_{21} = \frac{\sigma_{es}I_s}{h\nu_s},$  (2.7–2.8)

$$A_{21} = \frac{1}{\tau_{21}},\tag{2.9}$$

where  $\tau_{21}$  is the upper-state lifetime.

#### 2.2.1**Propagation Equations**

In a doped fiber waveguide, the pump and signal powers evolve along the longitudinal coordinate z as:

$$\frac{dP_p}{dz} = \Gamma_p N_t \left( \sigma_{ep} n_2 - \sigma_{ap} n_1 \right) P_p(z), \tag{2.10}$$

$$\frac{dP_s}{dz} = \Gamma_s N_t \left(\sigma_{es} n_2 - \sigma_{as} n_1\right) P_s(z), \tag{2.11}$$

where  $\Gamma_p$  and  $\Gamma_s$  are the overlap factors between the guided modes and the doped area, defined as

$$\Gamma_{p,s} = \frac{\int_{A_{\text{doped}}} |E_{p,s}(x,y)|^2 dA}{\int_{A_{\text{out}}} |E_{p,s}(x,y)|^2 dA},$$
(2.12)

with  $E_{p,s}(x,y)$  denoting the transverse field distribution of the pump or signal mode. The overlap factor represents the fraction of the optical power that effectively interacts with the doped ions in the core. Since only the portion of the mode confined within the active region contributes to absorption and stimulated emission processes,  $\Gamma_p$  and  $\Gamma_s$  directly scale the effective cross-sections appearing in the rate equations. In practice, a higher overlap implies more efficient pump absorption and stronger signal amplification, whereas poor overlap leads to reduced gain and higher pump power requirements. The local small-signal gain coefficient is:

$$g(z) = \Gamma_s N_t \left( \sigma_{es} n_2 - \sigma_{as} n_1 \right). \tag{2.13}$$

#### 2.2.2 Gain Spectrum and Relative Inversion

It is convenient to introduce the *relative inversion*:

$$RI = n_2 - n_1. (2.14)$$

For an active ion density  $N_t=10^{26}\,\mathrm{m}^{-3}$  and ideal overlap ( $\Gamma_s=1$ ), Eq. (2.13) becomes:

$$g(\lambda) = N_t \left[ \sigma_e(\lambda) \frac{1 + RI}{2} - \sigma_a(\lambda) \frac{1 - RI}{2} \right]. \tag{14}$$

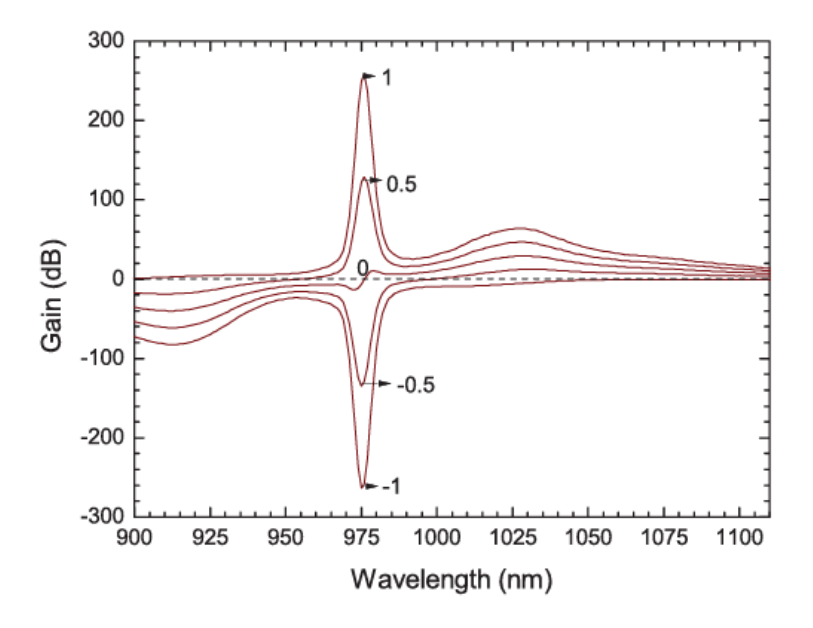


Figure 2.5: Gain spectrum at different wavelengths for varying levels of relative inversion.

The gain spectra in Fig. 2.5 show how the amplification strongly depends on the inversion level. For RI = 0 (i.e. 50% population inversion), achieved when pumping at 975 nm due to the nearly equal absorption and emission cross-sections, the maximum gain occurs close to 1035 nm. Higher inversion levels (0 < RI < 1) can be

obtained by pumping at shorter wavelengths, where the maximum gain is centered at 975 nm. However, this also enhances the onset of Amplified Spontaneous Emission () at 975 nm, which limits the usable gain at longer signal wavelengths. Conversely, negative values of RI (0 > RI > -1) correspond to an unpumped medium, where re-absorption dominates and the net gain becomes negative. This behavior requires careful optimization of the fiber length to minimize re-absorption losses.

One of the primary sources of noise in fiber amplifiers is indeed Amplified Spontaneous Emission (). Unlike electrical amplifiers, where noise often arises from thermal agitation, optical amplifiers suffer from quantum noise mechanisms. Spontaneous emission occurs randomly in all directions; however, due to the waveguiding nature of the fiber core and its large aspect ratio, the spontaneous emission can be preferentially amplified along the propagation axis, resulting in [32]. Fig. 2.6 highlights how reduces the signal-to-noise ratio and ultimately limits the usable gain of the device. Moreover, can further reduce efficiency by promoting electrons from the excited metastable state to higher-lying energy levels, thereby depleting the population available for stimulated emission [33].

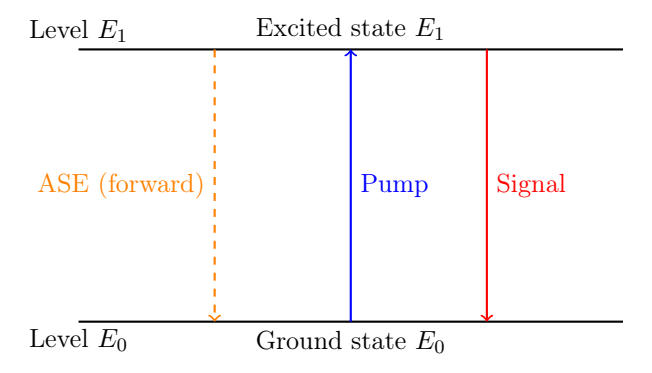


Figure 2.6: Simplified energy level diagram of a doped fiber showing pump absorption, stimulated emission (signal), and amplified spontaneous emission (ASE).

The presence of , illustrated in Fig. 2.6, thus represents a fundamental limitation in Yb-doped fiber systems, particularly around 975 nm, where the gain is highest. In order to mitigate these effects and achieve stable operation, fiber lasers must be designed by carefully tailoring cavity length, reflectivity, and pumping conditions, as discussed in the following section on fiber laser models.

#### 2.2.3 Fiber Amplifier Model

In contrast to the resonant cavity laser configuration, fiber amplifiers operate in an open geometry where the signal is amplified during a single pass through the active medium. A complete description requires solving the coupled differential rate equations, often numerically. However, under reasonable approximations, a simplified analytical solution can be obtained, which is extremely useful to gain physical insight and to estimate amplifier performance.

The model assumes:

- a two-level system approximation for Yb<sup>3+</sup>-doped fibers,
- homogeneous distributions of pump and signal intensities across the core,
- negligible contributions from excited-state absorption (ESA),
- seed power much larger than amplified spontaneous emission (ASE), ensuring a signal-dominated regime.

Under these conditions, the steady-state upper-level population can be written as:

$$n_2 = \frac{\sigma_{ap}\Gamma_s P_{sat,s} P_p + \sigma_{as}\Gamma_p P_{sat,p} P_s}{\Gamma_p \Gamma_s P_p P_{sat,s} + \Gamma_p \Gamma_s P_s P_{sat,p} + \Gamma_p \Gamma_s P_{sat,p} P_{sat,s}}.$$
 (2.15)

The pump and signal saturation powers are:

$$P_{sat,p} = \frac{h\nu_p A_{eff}}{\Gamma_p(\sigma_{ap} + \sigma_{ep})},\tag{2.16}$$

$$P_{sat,s} = \frac{h\nu_s A_{eff}}{\Gamma_s(\sigma_{as} + \sigma_{es})}.$$
 (2.17)

The evolution of pump and signal powers along the fiber is described by the coupled equations:

$$P_p^{out} + P_s^{out} = P_p^{in} \exp \left[ \sigma_p L + \frac{P_p^{in} - P_p^{out}}{P_{sat,p}} \right], \tag{2.18}$$

$$P_s^{out} = P_s^{in} \exp \left[ \sigma_s L + \frac{P_s^{in} - P_s^{out}}{P_{sat,s}} \right]. \tag{2.19}$$

These analytical expressions capture the fundamental physics of a fiber amplifier: the pump power drives the population inversion, which in turn amplifies the signal.

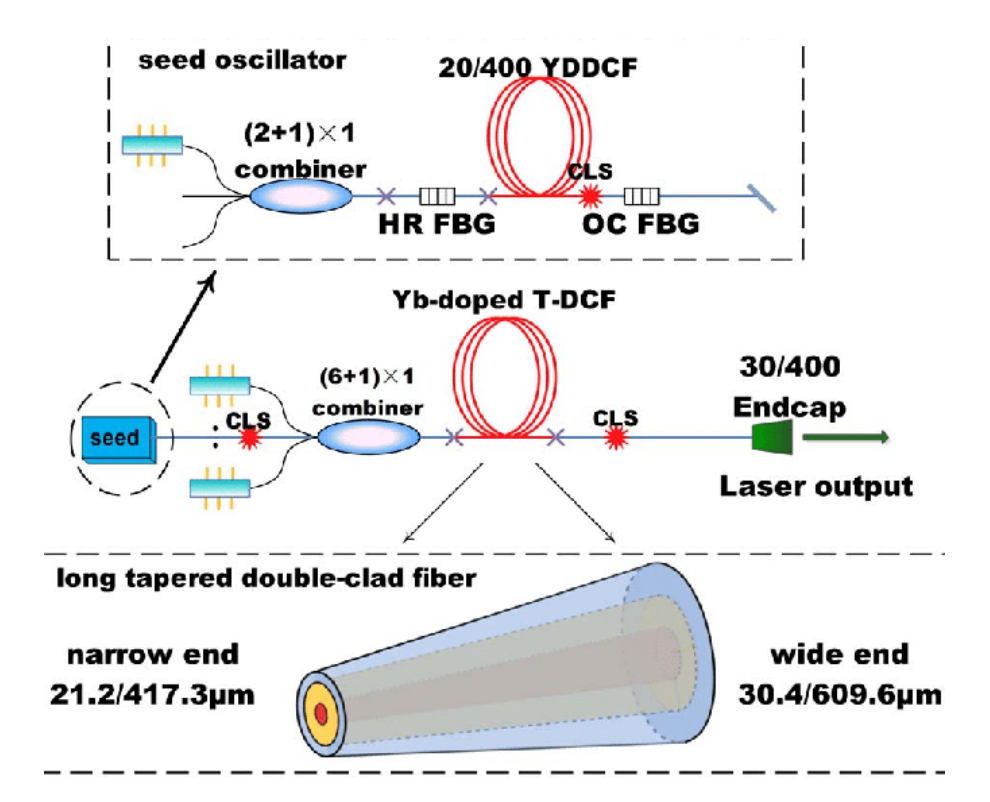


Figure 2.7: Example of a Yb-doped fiber amplifier, adapted from [4]. The simplified concepts of pump input  $(P_p^{in})$ , seed input  $(P_s^{in})$ , and output powers  $(P_s^{out}, P_p^{out})$  are clearly visible. The figure illustrates how these basic concepts are implemented in a practical system, and how more complex designs (multi-stage amplification, counterpumping, ASE management) build upon this fundamental scheme.

By comparing Eqs. (2.18)–(2.19) with Fig. 2.7, the reader can see how the basic amplification principles translate into a practical device. Although the figure shows a more complex layout, the essential mechanism remains the same: the pump drives inversion in the fiber core, which amplifies the input seed to produce the output signal. More advanced designs simply extend these concepts, for example by optimizing pump coupling, fiber geometry, or staging multiple amplification sections.

#### 2.2.4 Fiber Laser Model

When the active medium is placed inside a resonant cavity, the forward  $(P_s^+)$  and backward  $(P_s^-)$  propagating fields are determined by the boundary conditions imposed by the reflectivities of the cavity mirrors. The schematic configuration of a counter-pumped linear cavity fiber laser is shown in Fig. 2.8, where the fiber is pumped from the output side and the signal oscillates between the two reflectors.

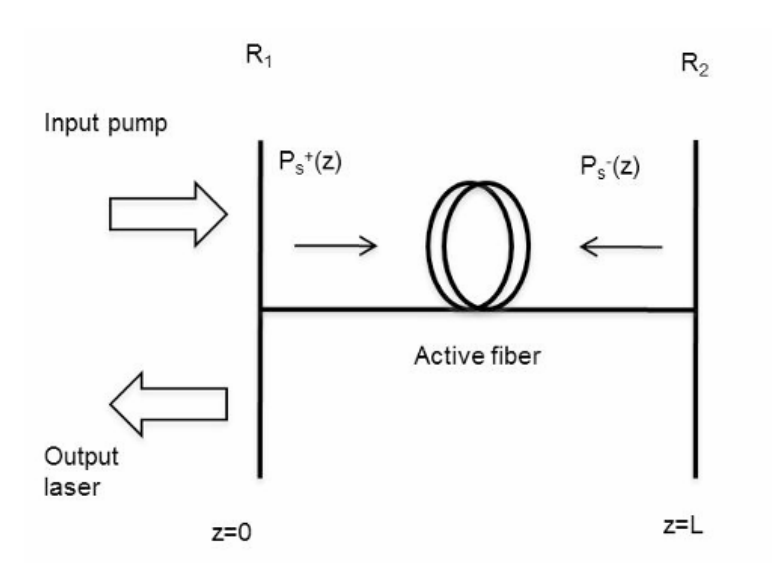


Figure 2.8: Schematic of counter-pumped linear cavity fiber laser. The pump is injected from the output side, while the forward  $(P_s^+)$  and backward  $(P_s^-)$  propagating signal fields are reflected by the cavity mirrors with reflectivities  $R_1$  and  $R_2$ .

According to this scheme, the fields satisfy the boundary conditions:

$$P_s^+(0) = R_1 P_s^-(0), (2.20)$$

$$P_s^-(L) = R_2 P_s^+(L), (2.21)$$

$$P_s^+(z)P_s^-(z) = \text{constant.} \tag{2.22}$$

It is worth noting that the assumption expressed in Eq. (2.22) corresponds to an approximation valid only under ideal conditions, where no internal losses are present and the cavity is considered perfectly efficient. In practical cases, the total power is not strictly conserved along the propagation due to effects such as absorption, scattering, or imperfect reflectivity, and therefore this condition holds only as a simplified model.

The net single-pass gain is defined as:

$$G = \int_0^L g(z) dz = \Gamma_s N_t \int_0^L (\sigma_{es} n_2 - \sigma_{as} n_1) dz.$$
 (2.23)

The stationary lasing condition requires:

$$R_1 R_2 \exp(2G) = 1. (2.24)$$

By substituting the propagation equations into Eq. (2.23), the pump-dependent

gain can be written as:

$$G_p = \ln\left[\frac{P_p(L)}{P_p(0)}\right] = \frac{\Gamma_p \lambda_p}{2\Gamma_s \lambda_s} \ln\left(\frac{1}{R_1 R_2}\right). \tag{20}$$

From this relation, the output laser power is obtained:

$$P_{out} = (1 - R_1)P_s^-(0). (2.24)$$

The laser threshold pump power corresponds to:

$$P_{th} = \frac{P_{sat,p}(G_p + \Gamma_p N_t \sigma_{ap} L)}{1 + \exp(G_p)}.$$
(2.25)

#### 2.2.5 Numerical Solution via Shooting Method

The coupled propagation equations for pump and signal (Eqs. (2.20),(2.22)) form a Boundary Value Problem (BVP), since conditions are imposed at both ends of the fiber:

- Signal:  $P_s^+(0) = R_1 P_s^-(0)$  and  $P_s^-(L) = R_2 P_s^+(L)$
- Pump:  $P_p(0)$  known at the input, residual  $P_p(L)$  determined by the fiber

A common numerical approach to solve this BVP is the **shooting method**:

- 1. Guess the unknown initial condition at z=0 (e.g., backward-propagating signal  $P_s^-(0)$ )
- 2. Integrate the coupled differential equations along the fiber as an Initial Value Problem (IVP)
- 3. Compare the computed value at z = L with the boundary condition  $P_s^-(L) = R_2 P_s^+(L)$
- 4. Iterate the initial guess until the boundary condition is satisfied within a chosen tolerance

This method allows direct computation of the pump and signal evolution along the fiber, respecting the physical boundary conditions imposed by the laser cavity. For amplifier configurations, the shooting method is typically required only in the case of bidirectional propagation (e.g., when both forward and backward signals are present due to reflections or ASE). In unidirectional amplifiers, instead, the problem reduces to an initial value problem (IVP) that can be solved by straightforward integration.

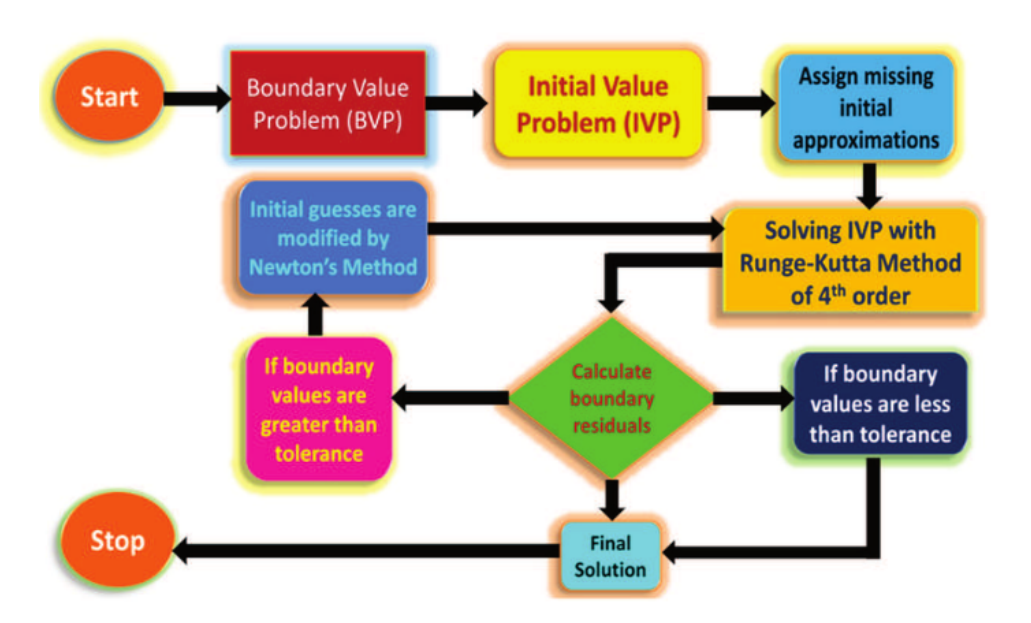


Figure 2.9: Flowchart of the shooting method applied to boundary value problems. Flowchart of the shooting method applied to boundary value problems. The boundary conditions are transformed into an initial value formulation, integrated iteratively with a Runge-Kutta scheme, and corrected until the desired accuracy is reached.

Figure 2.9 illustrates the algorithmic structure of the shooting method. The boundary value problem is first recast as an initial value problem (IVP) by assigning a trial value to the missing initial condition. The equations are then integrated along the fiber, typically with a fourth-order Runge–Kutta method, which provides a stable and accurate solution for the coupled pump and signal powers. At the fiber end, the computed values are compared with the required boundary condition: if the discrepancy (residual) exceeds a chosen tolerance, the initial guess is updated and the process is repeated. This iterative procedure ensures that the solution satisfies the boundary conditions imposed by the laser cavity or amplifier configuration.

# Chapter 3

# Numerical modeling and simulation procedures

#### 3.1 Motivations and role of simulation

The study and design of FL require a deep knowledge of the characteristic parameters of the active medium,in particular the absorption and emission cross sections  $(\sigma_{ap}, \sigma_{ep}, \sigma_{as}, \sigma_{es})$ , the upper-level lifetime  $(\tau_{21})$ , and the dopant concentration  $(N_t)$ . These parameters strongly affect the device performance, influencing fundamental aspects such as gain, efficiency, and lasing threshold. Unfortunately, the values reported in the literature are often unreliable, as they depend on several factors such as the glass host composition, the dopant concentration, and the operating regime of the fiber. Although direct measurements could, in principle, provide more accurate information, they are extremely challenging and prone to significant experimental uncertainties.

Numerical simulations therefore become an essential tool for understanding and predicting the behavior of fiber lasers. A reliable model enables not only the prediction and optimization of the laser performance before the physical realization, but also provides physical insight into the underlying mechanisms. However, without an accurate knowledge of the spectroscopic and physical parameters, simulation remains a merely theoretical exercise. For this reason, fitting procedures based on experimental data are of crucial importance, as they allow the indirect estimation of the unknown internal parameters starting from measurable quantities such as cavity length and pump power.

A calibrated simulation model therefore provides three main benefits:

- Prediction evaluate system performance without expensive or complex prototyping;
- 2. **Optimization** identify parameter values and operating conditions that maximize efficiency and output power;
- 3. **Physical insight** study the role of each parameter in the internal dynamics, highlighting the interplay between absorption, emission, and population inversion.

Simulation thus becomes not only a theoretical exercise, but a design and diagnostic tool that bridges the mathematical model with experimental data, guiding the realization of rare-earth-doped optical devices.

#### 3.2 Theoretical framework and numerical solution

The model of a Ytterbium-Doped Fiber Amplifier (YDFA) operating in CW regime is based on the system of rate equations, introduced in Chapter 2, which describe the temporal and spatial evolution of the population densities and of the pump and signal optical powers. This set of coupled, nonlinear differential equations cannot be solved analytically in closed form, and therefore requires a numerical approach. Among the various numerical integration methods, the Runge-Kutta Fourth-Order method (RK4) scheme is one of the most widely adopted, thanks to its favorable trade-off between accuracy and computational cost. To frame the comparison, it is useful to recall what the Euler method is: this is the simplest numerical scheme, where the derivative is evaluated only once per step, at the beginning of the interval, and then linearly extrapolated to estimate the next value. Although very intuitive and easy to implement, this approach tends to accumulate errors rapidly, especially for nonlinear systems or when relatively large step sizes are used. In contrast, the RK4 method improves the accuracy by computing the derivative at several intermediate points within each integration interval and combining them through a weighted average. This strategy allows a much better approximation of the true trajectory, even for coarser discretizations, providing a significant reduction of the global error compared to the Euler approach.

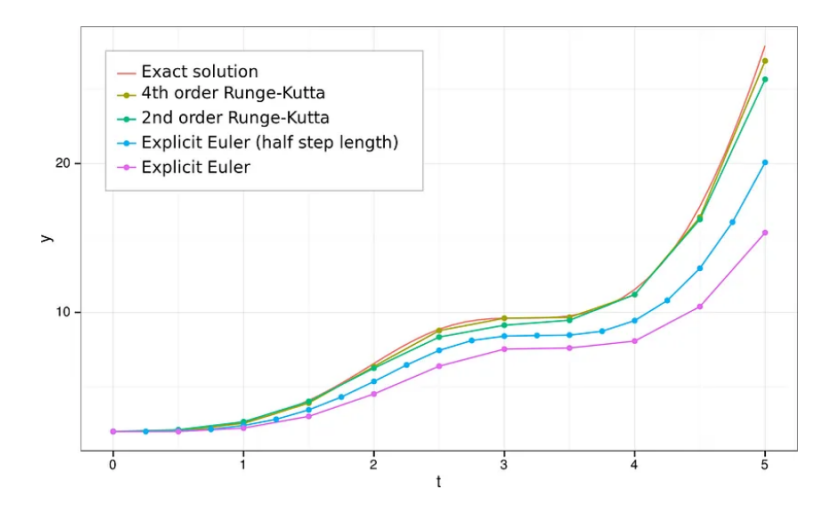


Figure 3.1: Comparison between the Euler and Runge–Kutta 4th-order (RK4) integration methods. The RK4 trajectory closely follows the true solution.[5].

In the general case, if y(z) is the unknown function (for instance the optical power along the fiber length) and f(z,y) its derivative, the RK4 algorithm can be written as:

$$k_1 = f(z_n, y_n), \tag{3.1}$$

$$k_2 = f(z_n + \frac{h}{2}, y_n + \frac{h}{2}k_1),$$
 (3.2)

$$k_3 = f(z_n + \frac{h}{2}, y_n + \frac{h}{2}k_2),$$
 (3.3)

$$k_4 = f(z_n + h, y_n + hk_3),$$
 (3.4)

$$y_{n+1} = y_n + \frac{h}{6}(k_1 + 2k_2 + 2k_3 + k_4), \tag{3.5}$$

where h is the integration step.

When applied to the system of rate equations, this scheme allows the step-by-step calculation of the population distribution and of the pump and signal powers along the cavity. This provides a quantitative description of the system in different operating conditions, for instance analyzing the variation of the residual pump and the output signal power as a function of cavity length.

The implementation of the Runge-Kutta method in MATLAB® is particularly advantageous, as it allows the numerical solver to be integrated within a more general model of the cavity, including the method for the boundary conditions and the optimization routines for parameter fitting. In the next section, the logical structure of the developed code will be presented, showing how the numerical algorithm fits into the overall simulation workflow.

#### 3.3 Structure of the simulation code

The MATLAB® code has been designed with a modular architecture, where the main script initializes the cavity parameters, defines the boundary conditions, and calls the appropriate routines to simulate either laser or amplifier operation. The boundary conditions are enforced through the previously explained shooting method, where an iterative loop propagates pump and signal powers until the reflectivity constraints at the cavity mirrors are satisfied within a given tolerance.

A convergence criterion is imposed to terminate the iterative process: the relative difference between two successive iterations must fall below  $10^{-6}$ . To prevent divergence in exceptional cases, a minimum number of iterations (typically 10–15) is enforced. This ensures both accuracy and computational efficiency.

The main script serves as the central controller of the simulation, orchestrating the initialization of all relevant parameters and the execution of the numerical routines. It first prompts the user to select the type of device to be simulated, either a laser or an amplifier, and then initializes the fiber characteristics and dopant properties by calling the GetDefaultSettings function, which assigns the appropriate physical and geometrical parameters according to the selected material system (e.g., erbium-, ytterbium-, or thulium-doped fiber) and operating wavelength. This includes setting the fiber length, pump and signal powers, core and cladding diameters, dopant concentrations, cross sections, and other parameters essential to describe the physical system. Once the parameters are set, the script determines whether a laser or an amplifier simulation is required. Depending on this choice, it calls the corresponding routines to propagate the pump and signal powers along the fiber. In the case of laser operation, a forward and backward propagation loop is executed, implementing the shooting method to enforce boundary conditions at the cavity mirrors. For amplifiers, only a single propagation along the active fiber is necessary, as no cavity is present. At the end of the simulation, the script stores the computed pump and signal powers along the fiber and produces graphical outputs for visualization.

Fig. 3.2 provides a flowchart with compact overview of the main script operation, highlighting the sequence of steps from initialization to results visualization. This flow helps in understanding how the modular routines, described in the following section, are orchestrated to simulate the behavior of different fiber devices.

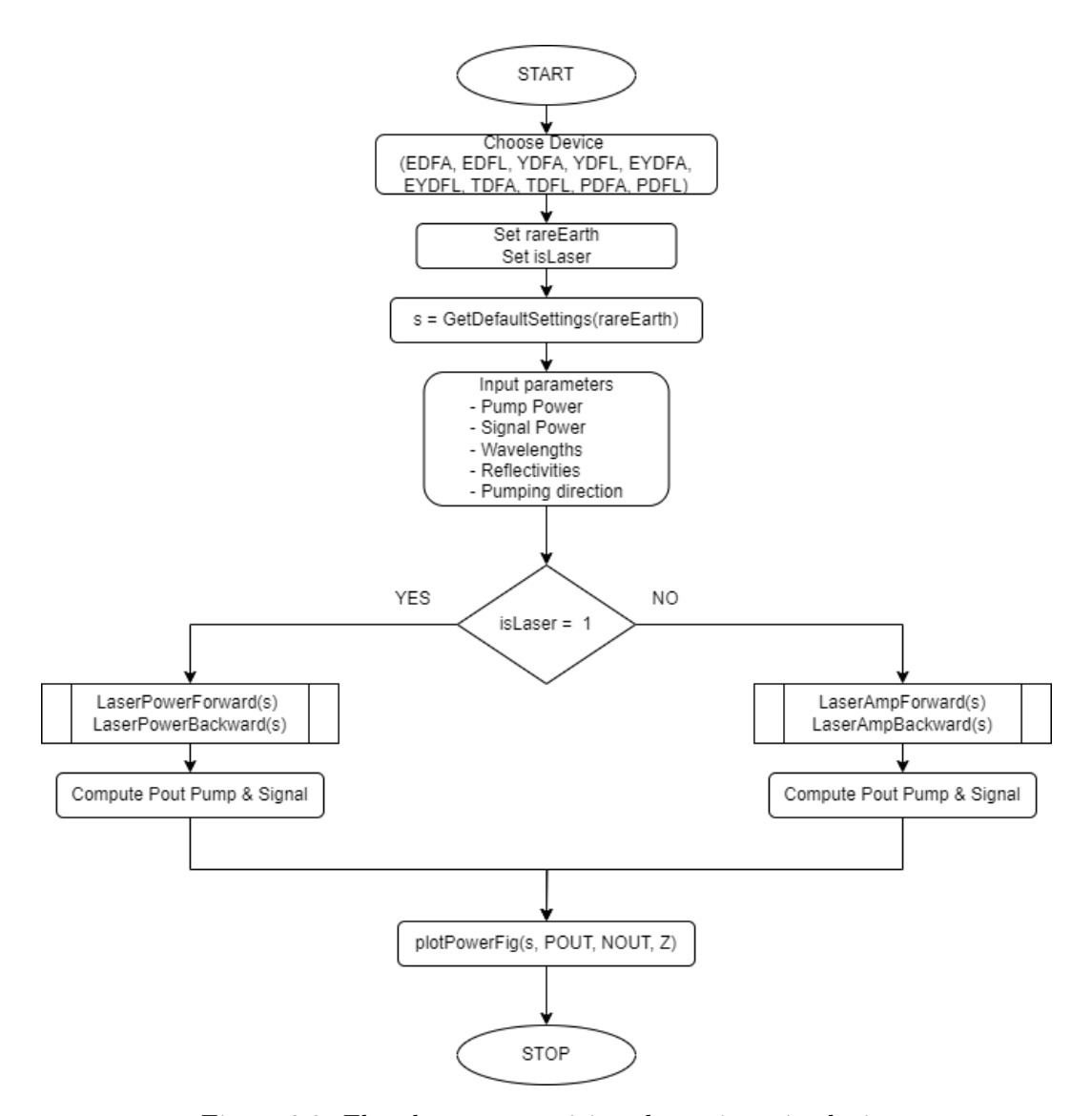


Figure 3.2: Flowchart summarizing the main script logic.

Analysis proceeds in detail on the functions called by the main script, which implement the core numerical routines for the simulation of laser and amplifier operation:

• LaserPowerForward: simulates forward-pumped laser cavities through a two-trip algorithm (forward and backward propagation).

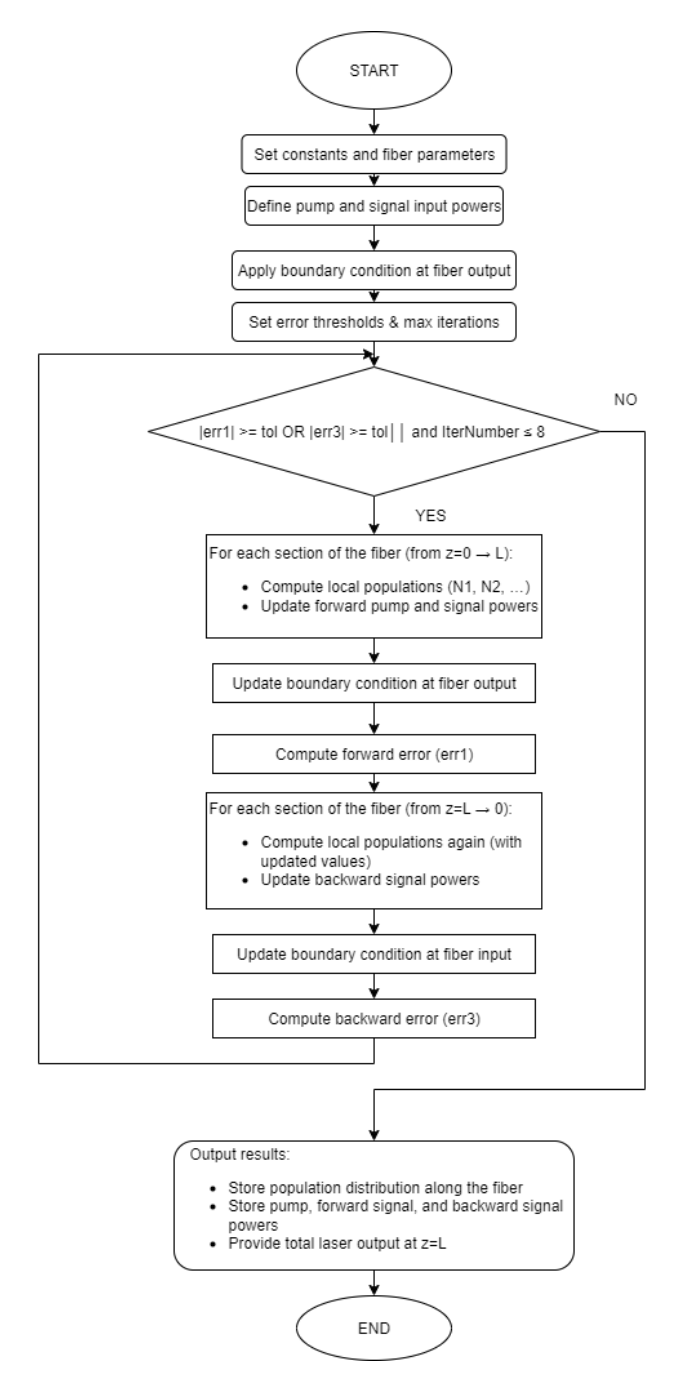


Figure 3.3: Compact flowchart of the LaserPowerForward routine, showing iterative forward/backward propagation with convergence check.

• LaserPowerBackward: This function is identical to LaserPowerForward, shown in Fig. 3.3, except that the integration proceeds from the fiber end towards the beginning and the boundary conditions are applied at the input rather than at

the output, to account for the backward propagation configuration.

• LaserAmpForward: describes forward-pumped amplifiers, where no cavity is present and only one forward propagation is required.

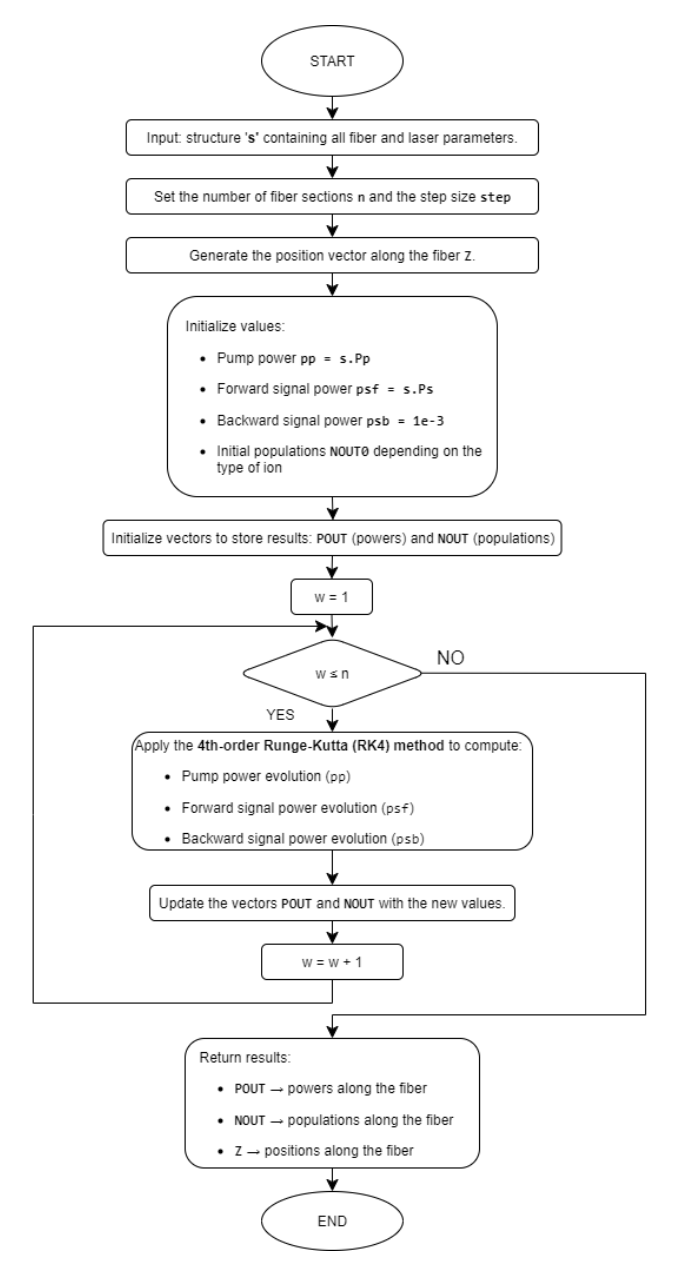


Figure 3.4: Flowchart of LaserAmpForward, showing initialization of parameters (with n as max iterations), iterative RK4 loop, and storage of outputs.

The core of the numerical model is implemented in dedicated functions:

• PopulationDensity: computes the distribution of ions among energy levels. For Yb, a simple two-level analytical model is used. For more complex dopants (Thulium (Tm), Holmium (Ho), Erbium (Er), or Ytterbium-Erbium (YbEr)

co-doped), the function uses MATLAB® solvers: fsolve, which attempts to solve F(x) = 0 starting from an initial guess (Optimization Toolbox) [35]; and vpasolve, which employs numeric methods with variable-precision arithmetic to solve symbolic equations (Symbolic Math Toolbox) [36].

- PPF and PPB: represent the differential equations for the pump power evolution in forward and backward direction, respectively.
- PSF and PSB: describe the forward and backward propagation of the signal power, including both gain and distributed losses.

Some simplifying assumptions were introduced to reduce the complexity of the model:

- In Yb-doped fibers, a two-level effective model was adopted, neglecting higherorder processes such as quenching or upconversion.
- A uniform spatial discretization was chosen, integrated with the RK4 method to balance accuracy and computational cost.
- Boundary conditions, simplified by neglecting losses, were implemented using an iterative shooting loop, typically converging within ten iterations.

Although this work focused on YDFL devices operating in CW regime, the modular code allows extending the model to other dopants (Tm, Ho, Er, or YbEr) with minimal modifications. This flexibility is ensured by the structure of PopulationDensity, which internally selects the appropriate solver depending on the rare-earth ion.

# 3.4 Simulation results: forward-pumped YDFA and YDFL

To demonstrate the performance of the developed numerical model, simulations were carried out for both a YDFA and a YDFL, considering only forward pumping. The input pump power was set to 10 W, with a signal wavelength of 1064 nm and a pump wavelength of 920 nm, typical for Yb-doped fibers. Although the main absorption peak of ytterbium is around 975 nm, the broader absorption band at 920 nm allows for more stable and efficient operation, as it does not require wavelength-stabilized diode modules. The YDFA configuration allows studying the amplification of a pre-existing signal along the active fiber without cavity effects, whereas the YDFL includes reflective cavity mirrors, enabling the analysis of lasing dynamics and output power saturation.

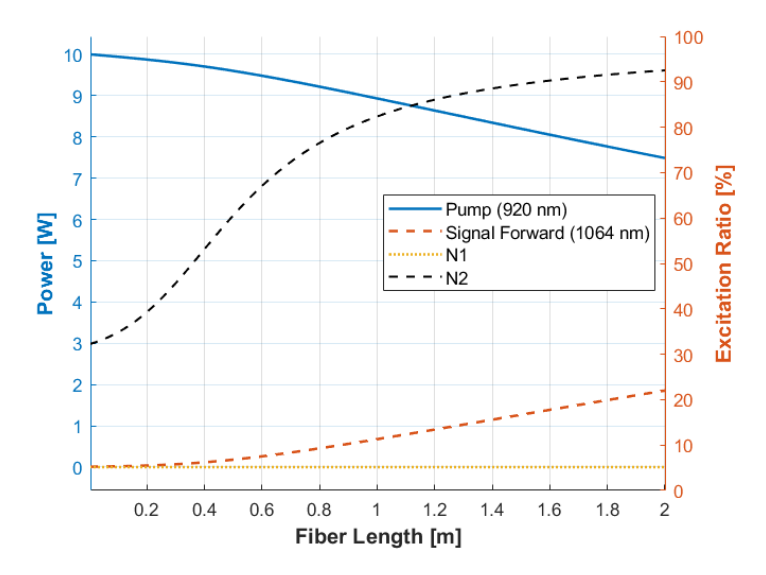


Figure 3.5: Pump  $(920 \,\mathrm{nm})$  and signal  $(1064 \,\mathrm{nm})$  power evolution along the fiber for a forward-pumped YDFA with input pump  $10 \,\mathrm{W}$ .

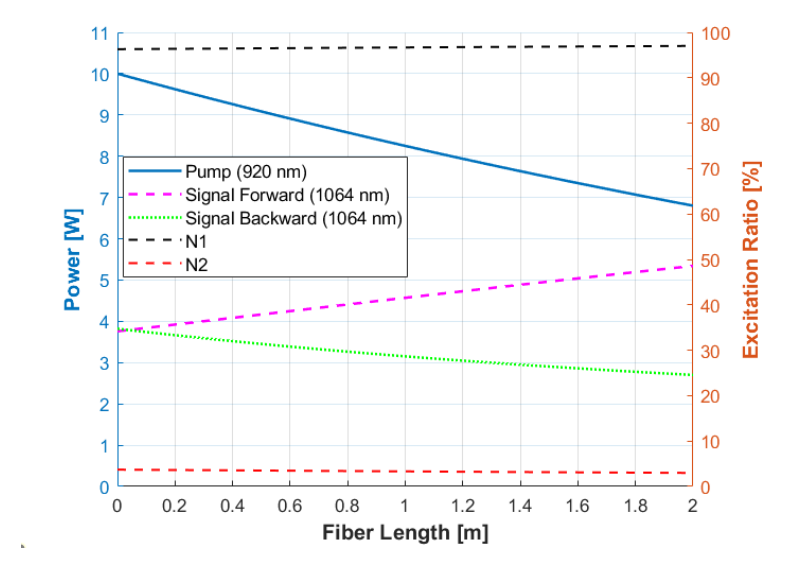


Figure 3.6: Pump (920 nm) and signal (1064 nm) power evolution along the fiber for a forward-pumped YDFL with input pump  $10\,\mathrm{W}$ .

In Figs. 3.5 and 3.6, the pump is depleted along the fiber, while the signal grows until saturation at the fiber end in the YDFL. The output signal reaches 0.93 W for the YDFA and 2.67 W for the YDFL, in agreement with literature on CW Yb-doped fiber devices [11, 37].

### 3.5 Sensitivity Analysis

The study of RE-Doped Fiber (RE) devices doped with ytterbium is strongly influenced by the accuracy with which the spectral and material parameters entering the propagation equations are known and modeled. For this reason, a sensitivity analysis was conducted to evaluate the impact of uncertainties on the fundamental parameters of the numerical model. This analysis provides valuable guidance for the fitting procedure, both in the theoretical modeling and in the experimental validation phases. Simulations were carried out considering a YDFA. However, the results obtained can be extended to the case of a YDFL, since the underlying physics governing the absorption and emission processes, as well as the rate and propagation equations, are the same in both configurations. The simulations were based on the numerical code presented in the previous section, which models the laser cavity and the propagation of pump and signal powers. All sensitivity analyses were performed by assuming an input signal power of 10 W and considering only the forward pumping scheme. For each parameter analyzed, the nominal value was varied by  $\pm 50 \,\%$ , keeping the others constant. In each case study, three plots are reported:

- 1. pump power along the fiber;
- 2. signal power along the fiber;
- 3. output signal power and residual pump at a fixed fiber length  $(L = 2 \,\mathrm{m})$ .

The first parameter considered is the concentration of dopant ions. The nominal value used in the simulations is  $4 \times 10^{25} \,\mathrm{m}^{-3}$ .

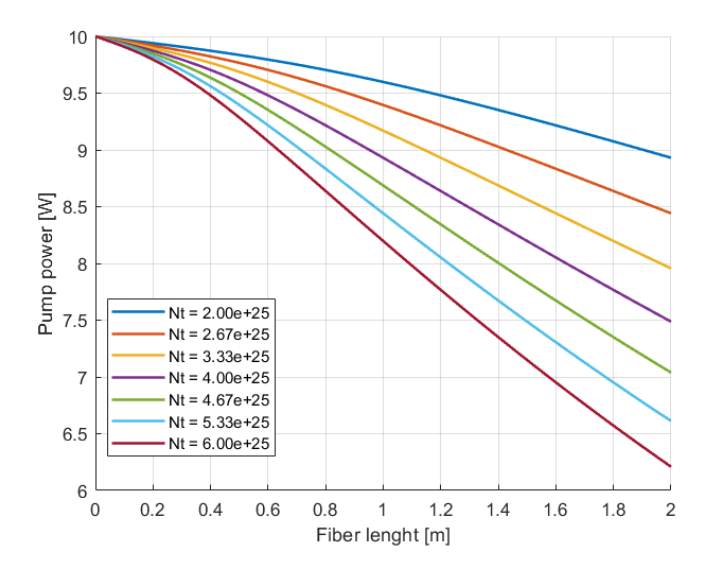


Figure 3.7: Pump power along the fiber as  $N_t$  varies ( $\pm 50\%$  relative to the nominal value).

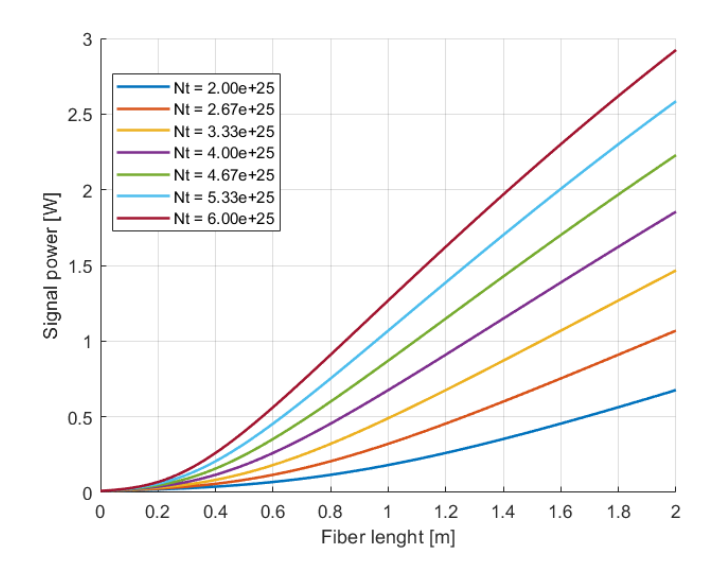


Figure 3.8: Signal power along the fiber as  $N_t$  varies ( $\pm 50\%$  relative to the nominal value).

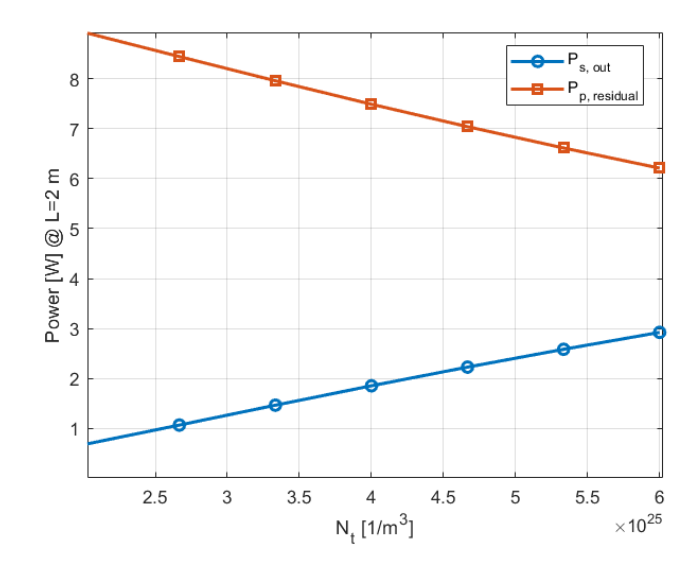


Figure 3.9: Output signal power and residual pump at L = 2 m as  $N_t$  varies ( $\pm 50 \%$  relative to the nominal value).

From the simulations shown in Figs. 3.7, 3.8, and 3.9, it is evident that the concentration  $N_t$  has a significant impact on device behavior. An increase in the number of dopant ions accelerates pump absorption along the fiber, resulting in a higher output signal power, while a 50 % reduction in concentration leads to lower conversion efficiency and slower signal growth. In particular, the values obtained at the fixed fiber length L=2 m correspond to the measurable quantities in experiments, confirming that  $N_t$  represents one of the most critical parameters to determine accurately for

correct modeling and design of the device.

Subsequently, the same sensitivity analysis was carried out on the lifetime of the upper laser level,  $\tau_{21}$ , whose nominal value was set to  $9.43 \times 10^{-4}$  s. As in the previous case, three simulations were performed by varying the parameter by  $\pm 50\%$  with respect to the nominal value, while keeping all the other parameters fixed.

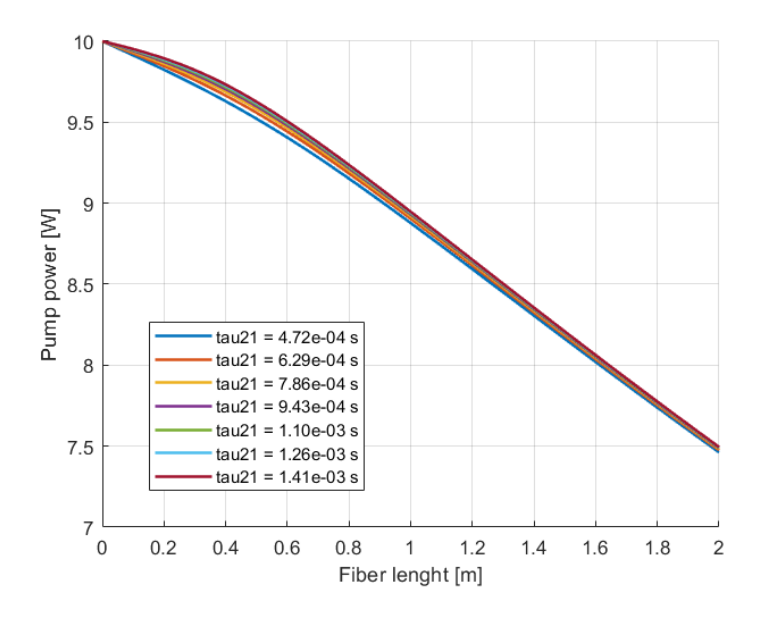


Figure 3.10: Pump power evolution along the fiber length for different values of  $\tau_{21}$ .

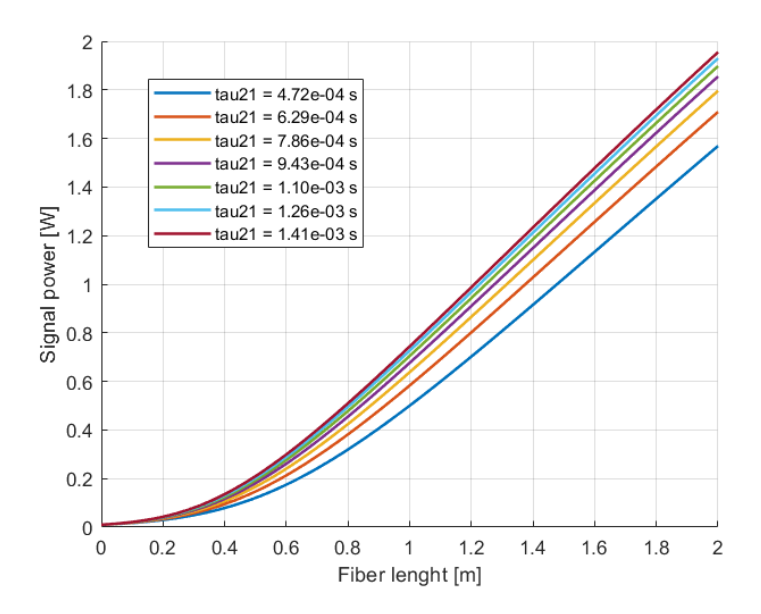


Figure 3.11: Signal power evolution along the fiber length for different values of  $\tau_{21}$ .

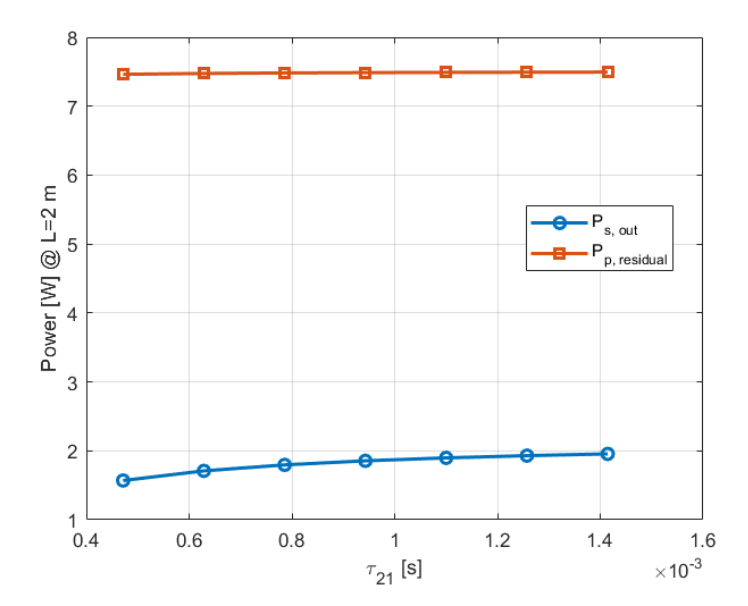


Figure 3.12: Output signal power and residual pump at a fixed fiber length of 2 m, for different values of  $\tau_{21}$ .

From Figs. 3.10, 3.11, 3.12 it emerges that the curves do not exhibit significant deviations despite the variations applied to  $\tau_{21}$ , indicating that the system performance is only weakly dependent on this parameter. This confirms that the uncertainty on the lifetime of the excited state plays a minor role compared to other material and spectroscopic parameters.

In the following, the same analysis will be extended to the absorption and emission pump cross sections,  $\sigma_{ap}$  and  $\sigma_{ep}$ , in order to assess their relative influence on device performance.

These two parameters are related through the expression; [38]

$$\sigma_{ap} = \sigma_{ep} \cdot \exp\left(\frac{h\nu_p - E_0}{k_B T}\right),\tag{3.6}$$

where h is Planck's constant,  $\nu_p = c/\lambda_p$  is the pump frequency,  $E_0$  is the characteristic transition energy,  $k_B$  is the Boltzmann constant, and T is the temperature. In this analysis the temperature was fixed at 296 K (23 °C), consistently with the experimental conditions. The nominal values used as reference were  $\sigma_{ep} = 3.80 \times 10^{-26} \text{ m}^2$  and  $\sigma_{ap} = 7.80 \times 10^{-25} \text{ m}^2$ .

In the simulations,  $\sigma_{ep}$  was varied by  $\pm 50\%$  with respect to its nominal value, while  $\sigma_{ap}$  was recalculated according to Eq. (1). All other parameters were kept constant.

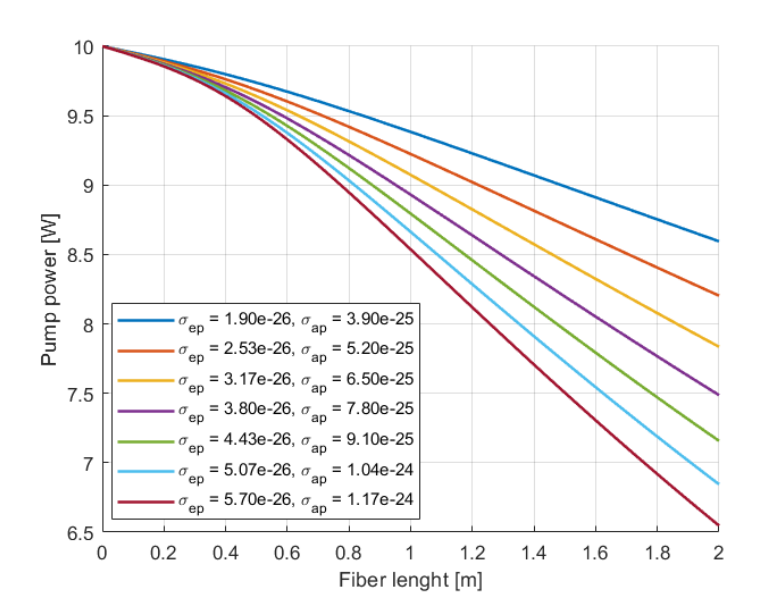


Figure 3.13: Pump power evolution along the fiber length for different values of of  $\sigma_{ap}$  and  $\sigma_{ep}$ .

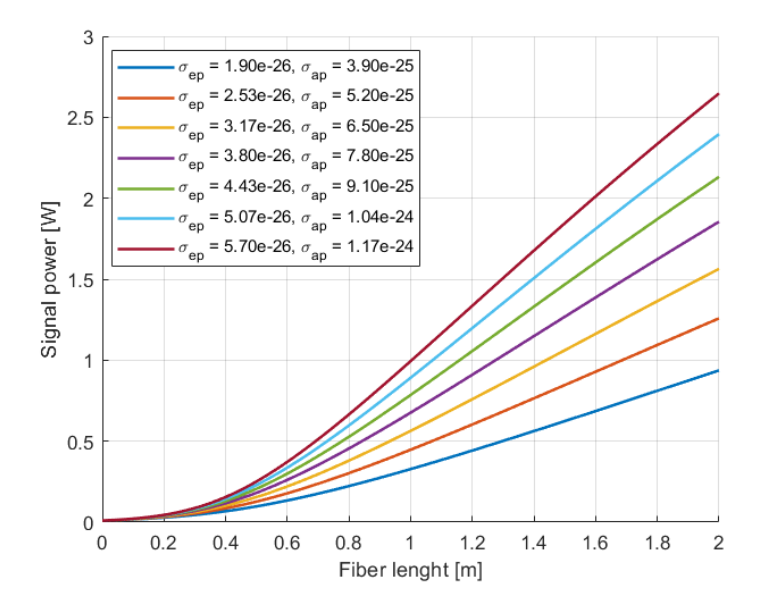


Figure 3.14: Signal power evolution along the fiber length for different values of  $\sigma_{ap}$  and  $\sigma_{ep}$ .

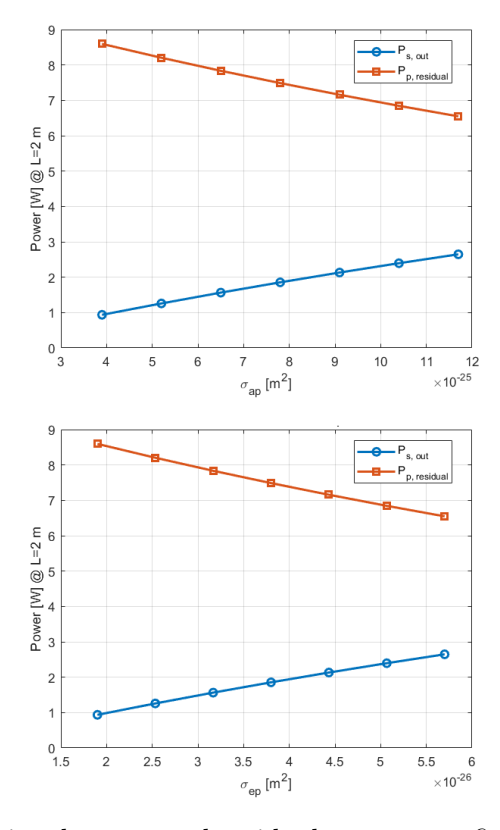


Figure 3.15: Output signal power and residual pump at a fixed fiber length of 2 m, for varying  $\sigma_{ap}$  (top) and varying  $\sigma_{ep}$  (bottom).

From Figs. 3.13, 3.14, it can be observed that variations of  $\pm 50\%$  in the emission cross section, and the corresponding recalculated absorption cross section, produce non-negligible deviations in the evolution of both the signal and the residual pump power. From Fig. 3.15, which shows the output signal power and residual pump at a fixed fiber length of 2 m for varying  $\sigma_{ap}$  (left) and  $\sigma_{ep}$  (right), it can be observed that variations of  $\pm 50\%$  in the emission cross section, and the corresponding recalculated absorption cross section, produce non-negligible deviations in both quantities. This confirms the critical role played by  $\sigma_{ap}$  and  $\sigma_{ep}$  in determining device performance and highlights the need for careful measurement and accurate modeling of these spectroscopic parameters to achieve reliable simulations.

The sensitivity study is now extended to the absorption and emission signal cross sections,  $\sigma_{as}$  and  $\sigma_{es}$ , in order to evaluate their impact on the performance of the fiber device. As in the previous case, the two parameters are linked through Eq. (3.6), which also relates the absorption and emission cross sections at the signal wavelength. The nominal reference values used in this analysis were  $\sigma_{es} = 3.02 \times 10^{-25} \text{ m}^2$  and  $\sigma_{as} = 5.13 \times 10^{-27} \text{ m}^2$ . In the simulations,  $\sigma_{es}$  was varied by  $\pm 50\%$  around its nominal value, while  $\sigma_{as}$  was recalculated accordingly, keeping all other parameters constant.

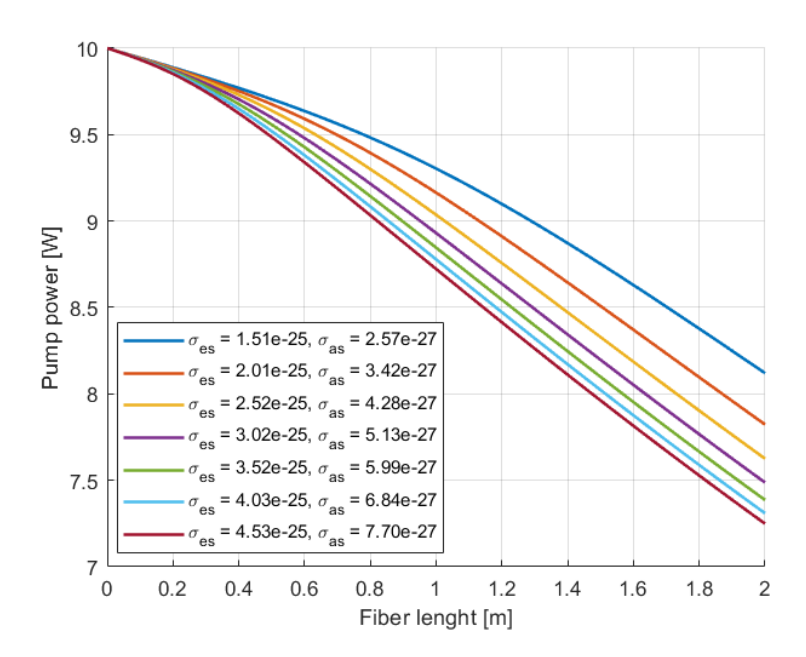


Figure 3.16: Pump power evolution along the fiber for different values of  $\sigma_{as}$  and  $\sigma_{es}$ .

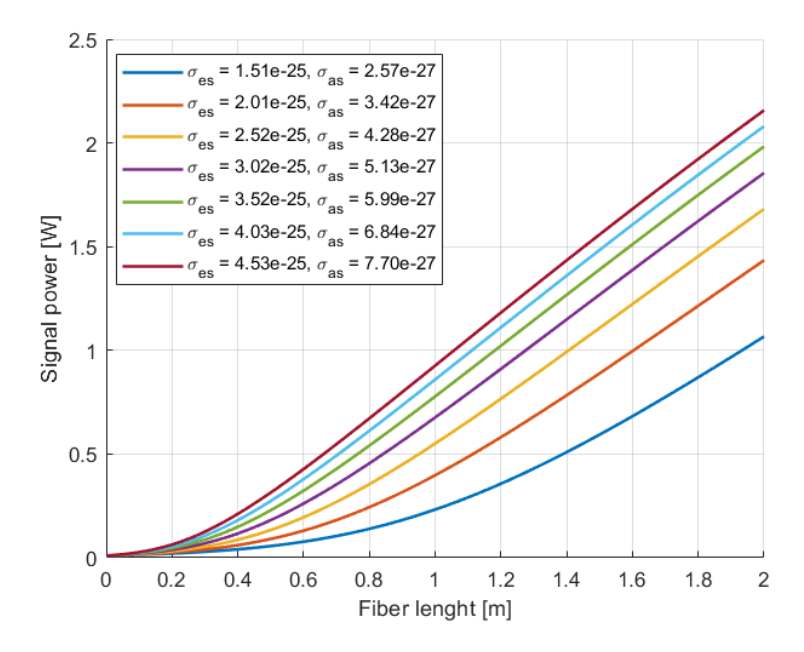


Figure 3.17: Signal power evolution along the fiber for different values of  $\sigma_{as}$  and  $\sigma_{es}$ .

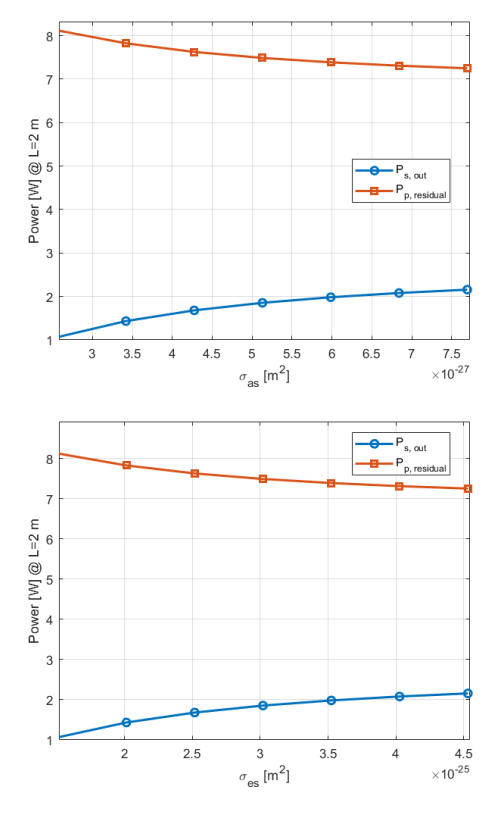


Figure 3.18: Output signal power and residual pump at a fixed fiber length of 2 m, for varying  $\sigma_{as}$  (top) and varying  $\sigma_{es}$  (bottom).

From Fig. 3.16,3.17, 3.18, it is evident that variations of  $\pm 50\%$  in the emission cross section, along with the corresponding recalculated absorption cross section, lead to noticeable changes in both output signal and residual pump at a fixed fiber length of 2 m. These results highlight the key role of  $\sigma_{as}$  and  $\sigma_{es}$  in defining the device performance and emphasize the necessity of accurate measurement and modeling of these spectroscopic parameters for reliable simulation outcomes.

In addition to the independent variation of single spectroscopic parameters, it is also relevant to investigate the combined influence of the dopant concentration  $N_t$  and the absorption signal cross section  $\sigma_{as}$ . These two quantities are directly related through their product

$$\alpha = N_t \cdot \sigma_{as},\tag{3.7}$$

The absorption coefficient is a fundamental spectroscopic parameter, since it directly relates to the effective strength of light absorption in the medium and thus strongly influences both pump absorption and signal amplification processes [39, 40]. In this study,  $\sigma_{as}$  was varied by  $\pm 50\%$  with respect to its nominal value  $\sigma_{as} = 4.40 \times$ 

 $10^{-27} \,\mathrm{m}^2$ , while  $N_t$  was recalculated in order to keep  $\alpha$  constant at its nominal value of  $\alpha = 0.2052$ . The nominal doping concentration used as reference was  $N_t = 4.00 \times 10^{25} \,\mathrm{m}^{-3}$ .

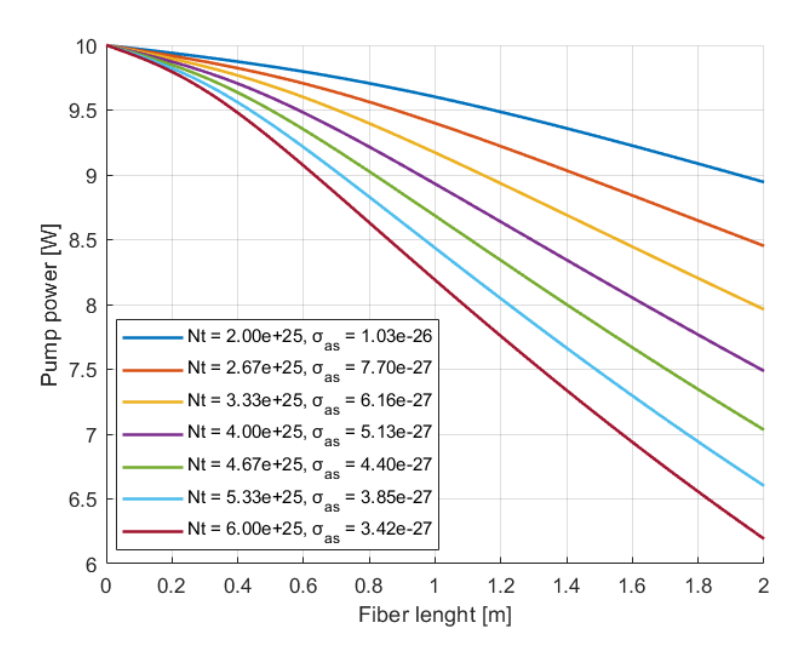


Figure 3.19: Pump power evolution along the fiber for different combinations of  $N_t$  and  $\sigma_{as}$  keeping  $\alpha$  constant.

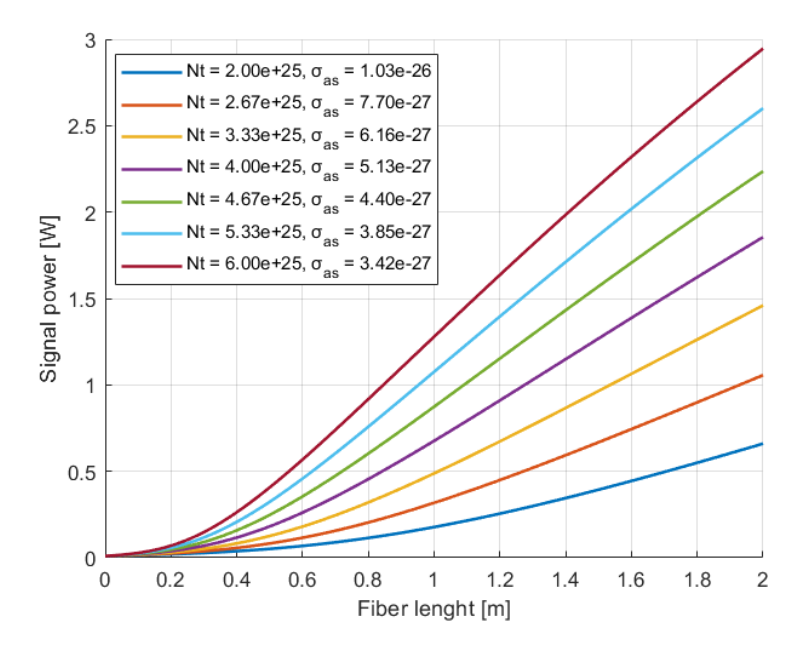


Figure 3.20: Signal power evolution along the fiber for different combinations of  $N_t$  and  $\sigma_{as}$  keeping  $\alpha$  constant.

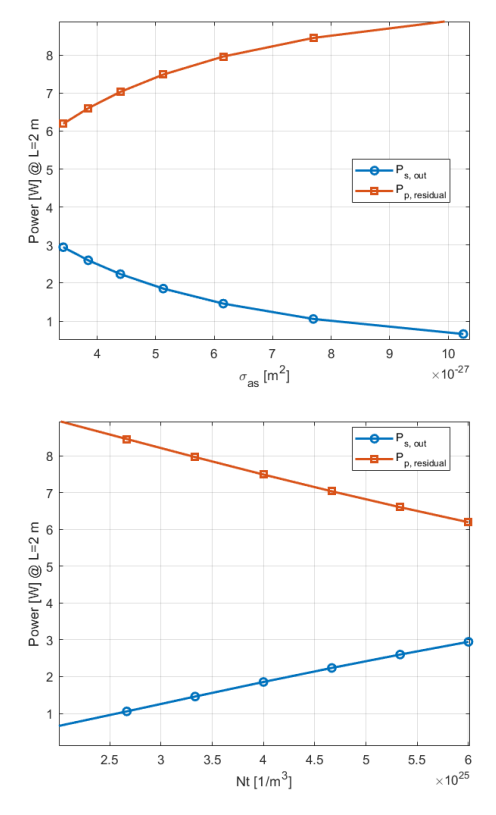


Figure 3.21: Output signal power and residual pump at a fixed fiber length of 2 m, for varying  $\sigma_{as}$  (top) and varying  $N_t$  (bottom), while keeping  $\alpha$  constant.

From Figs. 3.19, 3.20 it can be observed that variations of  $\pm 50\%$  in  $\sigma_{as}$ , with the corresponding recalculated  $N_t$  to preserve  $\alpha$ , produce evident deviations in both the pump and signal evolution along the fiber. At a fixed length of 2 m, in Fig. 3.21, where output signal and residual pump can be directly measured, these differences remain clearly visible. This confirms that the combined treatment of  $N_t$  and  $\sigma_{as}$  through the absorption coefficient  $\alpha$  provides a meaningful sensitivity perspective, underlining their critical role in determining device performance.

The final part of the sensitivity analysis focuses on the combined effect of the doping concentration  $N_t$  and the pump absorption cross section  $\sigma_{ap}$ . This aspect is particularly relevant, since the product of these two quantities is often reported in the datasheets of commercial fibers and provides direct experimental insight into the absorption characteristics of the material. Similarly to the case of  $N_t$  and  $\sigma_{as}$ , the relevant quantity is their product, which defines the small-signal pump absorption coefficient:

$$\alpha_p = N_t \cdot \sigma_{ap}. \tag{3.8}$$

In this study,  $\sigma_{ap}$  was varied by  $\pm 50\%$  with respect to its nominal value, while  $N_t$  was recalculated in order to keep  $\alpha_p$  constant. The reference parameters were

 $\sigma_{ap} = 7.80 \times 10^{-25} \,\mathrm{m}^2$  and  $N_t = 4.00 \times 10^{25} \,\mathrm{m}^{-3}$ , corresponding to an absorption coefficient of  $\alpha_p = 31.20 \,\mathrm{m}^{-1}$ . All other spectroscopic and geometrical parameters were kept unchanged.

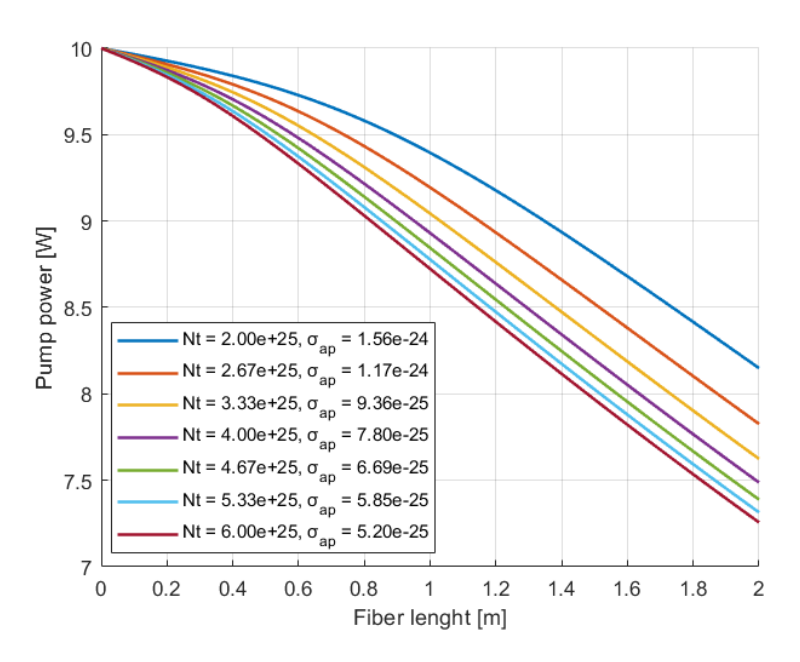


Figure 3.22: Pump power evolution along the fiber length for different values of  $\sigma_{ap}$  and the corresponding recalculated  $N_t$ .

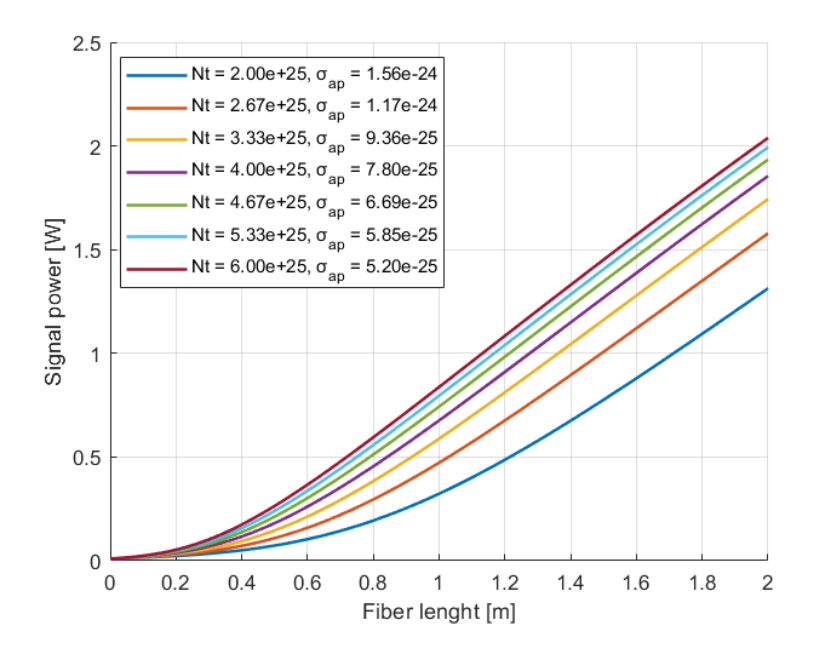
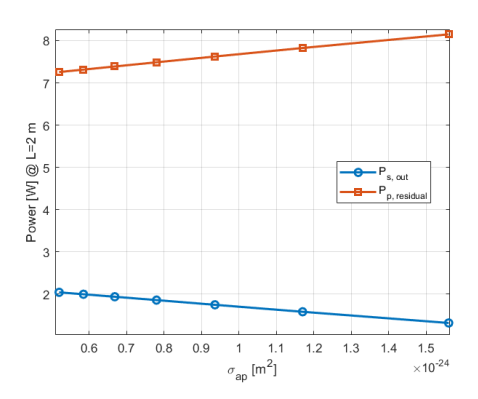


Figure 3.23: Signal power evolution along the fiber length for different values of  $\sigma_{ap}$  and the corresponding recalculated  $N_t$ .



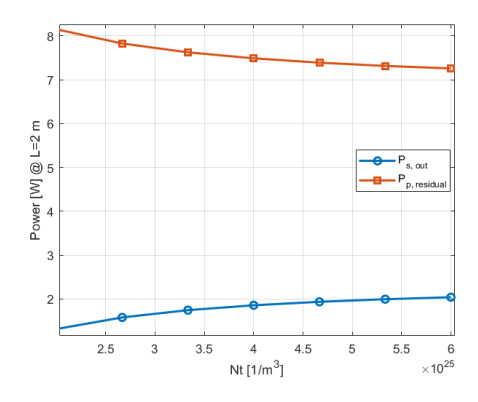


Figure 3.24: Output signal power and residual pump at a fixed fiber length of 2 m, for varying  $\sigma_{ap}$  (left) and varying  $N_t$  (right).

From Figs. 3.22,3.24, it can be observed that variations of  $\pm 50\%$  in the absorption cross section, accompanied by a corresponding recalculation of  $N_t$ , induce noticeable deviations in the evolution of both the residual pump and the signal power. In particular, Fig. 3.24 highlights that, at a fixed fiber length of 2 m, the output signal and residual pump remain strongly affected by such variations. These results confirm the significant sensitivity of device performance to the accuracy of  $\sigma_{ap}$  and  $N_t$ , underlining the importance of a precise characterization of these parameters in order to achieve reliable modeling and predictive simulations.

In conclusion, the sensitivity analysis has demonstrated that variations in the main spectroscopic and physical parameters, such as the absorption and emission cross sections and the dopant concentration, can lead to significant deviations in both the residual pump power and the signal power. In particular, even variations (on the order of  $\pm 50\,\%$ ) from the nominal values produce noticeable effects, highlighting the need for accurate characterization of the fundamental parameters of the model. This sensitivity will inevitably be reflected in the subsequent optimization through fitting of the experimental data: uncertainties in the input values can influence the reliability of the calibration process and, consequently, the predictive capability of the model. As will be discussed in the following section, this aspect becomes evident when comparing fitting results obtained from different sets of nominal parameters.

To further underline this aspect, Fig. 3.25 reports the values of the spectroscopic parameters of the ytterbium-doped double-clad fiber (YD-DC,  $10/125\,\mu\text{m}$ ) used in the experimental activity, as retrieved from different sources in the literature and datasheets. Even though the same fiber type is considered, the reported parameters exhibit non-negligible discrepancies. In particular, the largest deviations are found for the dopant concentration  $N_t$ , the absorption cross section at the pump wavelength  $\sigma_{ap}$ , and the emission cross section at the signal wavelength  $\sigma_{es}$ . The histograms,

plotted in logarithmic scale for the cross sections, highlight the variability across the different references and confirm that the choice of the nominal set of parameters has a direct impact on the simulation results and on the robustness of the fitting procedure.

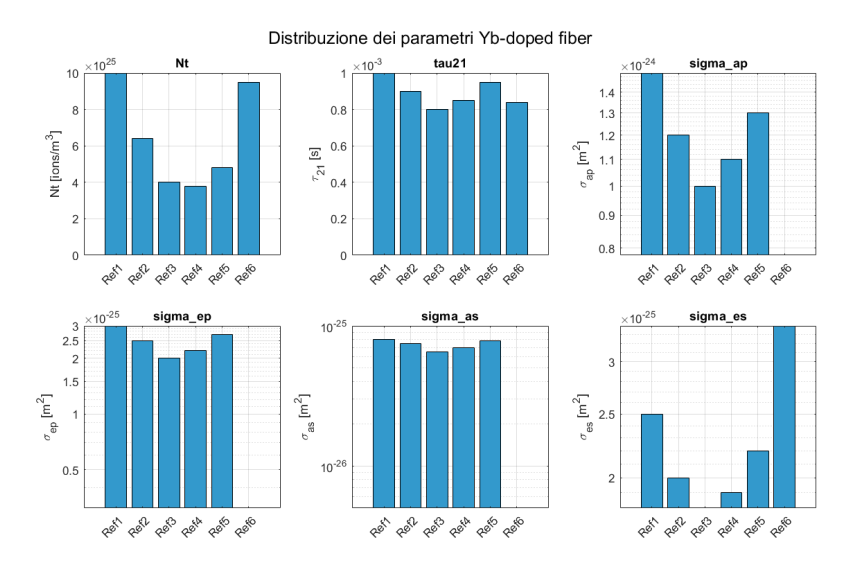


Figure 3.25: Comparison of the spectroscopic parameters of the Nufern 10 125 DC fiber as reported by different sources. The most significant variations are observed for the dopant concentration  $N_t$ , the absorption cross section at the pump wavelength  $\sigma_{ap}$ , and the emission cross section at the signal wavelength  $\sigma_{es}$  [6, 7, 8, 9, 10, 11].

# 3.6 Numerical Fitting as Preliminary Validation

Following the sensitivity analysis, the feasibility of using an optimization algorithm to retrieve simulated parameter values from experimental data was assessed through a numerical fitting procedure of the main spectroscopic parameters. To this end, the Particle Swarm Optimization (PSO) algorithm was employed, which efficiently identifies the set of parameters that minimize the discrepancy between the simulated curves and the reference data.

In this preliminary phase, no restrictions were imposed on individual parameters: the fitting was performed on all the most relevant quantities (doping concentration, lifetime, and absorption and emission cross sections), ensuring consistency between the retrieved values and the trends already highlighted during the sensitivity analysis. For validation purposes, reference data were taken from the commercial simulator RP Fiber Power (RP Photonics) [38], which is widely adopted for modeling rare-earth-doped fiber lasers and amplifiers. In particular, several configurations were analyzed, corresponding to fiber lengths of  $2 \,\mathrm{m}$ ,  $4 \,\mathrm{m}$ , and  $8 \,\mathrm{m}$ , combined with different values of output coupler reflectivity (R = 0.1, 0.3, 0.5). These operating conditions allow the investigation of representative scenarios for power propagation in YDFLs.

The fitting criterion was based on the minimization of the sum of squared errors Sum of Squared Errors (SSE) between the simulated and reference powers at the fiber output. For each candidate parameter set  $x_i$ , the total error is computed as:

$$E(x_i) = \sum_{k=1}^{N_{\text{ref}}} \left[ \left( P_{p,\text{ref}}^{(k)} - P_{p,\text{sim}}^{(k)}(x_i) \right)^2 + \left( P_{s,\text{ref}}^{(k)} - P_{s,\text{sim}}^{(k)}(x_i) \right)^2 \right], \tag{3.9}$$

where  $P_{p,\text{sim}}^{(k)}(x_i)$  and  $P_{s,\text{sim}}^{(k)}(x_i)$  denote, respectively, the simulated pump and forward-signal powers at the fiber end for the k-th reference condition. This formulation penalizes large deviations more strongly and provides a smooth and convex error surface, improving the robustness of the optimization and helping the PSO algorithm to avoid premature convergence toward suboptimal minima.

This approach represents a preliminary validation step, aimed at testing the robustness of the MATLAB®-based fitting procedure before applying it to the experimental
data, which will be discussed in the following chapter. The fitting procedure developed in MATLAB® follows a structured workflow, summarized in the flowchart of
Fig. 3.26. Starting from the reference datasets exported from RP Fiber Power, the
algorithm computes the simulated output curves, evaluates the error function SSE,
and iteratively applies the optimization routine to minimize the discrepancy with the
reference values. The optimized parameter set is then used to update the simulated
curves, which are directly compared with the reference data. This logical sequence

is represented in the flowchart, while the optimization algorithm itself (PSO) will be described in detail in the following subsection.

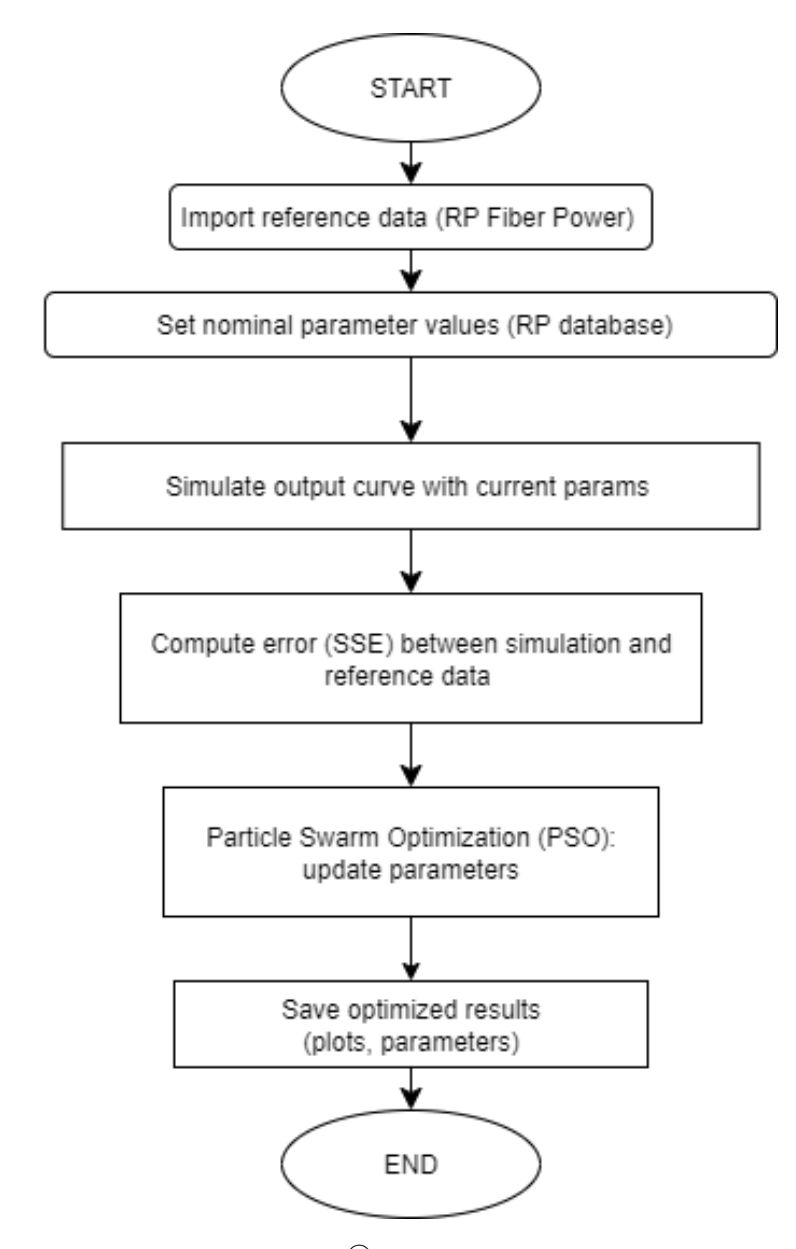


Figure 3.26: Workflow of the MATLAB®-based fitting procedure: from data retrieval to error evaluation and parameter optimization.

## 3.6.1 Particle Swarm Optimization (PSO)

To perform the fitting procedure effectively, it is essential to explain the rationale behind the choice of the optimization algorithm. Among several possible methods, Particle Swarm Optimization (PSO) was selected for its robustness and its reduced tendency to become trapped in local minima. The PSO is a stochastic, population based optimization technique inspired by collective behavior observed in nature, such as bird flocks or fish schools [41]. In these systems, each individual adjusts its movement based on both its own experience and information shared by the group. The PSO algorithm applies the same principle numerically: a set of candidate solutions, called particles, moves through the parameter space, updating their positions according to both their personal best positions and the best position found by the swarm. This combination of individual learning and collective information enables an efficient exploration of the solution space, making PSO particularly suitable for the parameter fitting task.

Each particle i is characterized by a position vector  $\mathbf{x}_i$  and a velocity vector  $\mathbf{v}_i$ . The position represents a potential solution to the optimization problem, while the velocity determines the direction and magnitude of the particle's movement in the parameter space. At each iteration, the velocity and position are updated according to the following rules:

$$\mathbf{v}_i(t+1) = w\mathbf{v}_i(t) + c_1r_1(\mathbf{p}_i - \mathbf{x}_i(t)) + c_2r_2(\mathbf{g} - \mathbf{x}_i(t))$$
$$\mathbf{x}_i(t+1) = \mathbf{x}_i(t) + \mathbf{v}_i(t+1)$$

where:

- w is the *inertia weight*, controlling how much the particle tends to maintain its previous velocity;
- $c_1$  and  $c_2$  are the personal and social learning coefficients, respectively;
- $r_1$  and  $r_2$  are uniformly distributed random numbers in [0,1];
- $\mathbf{p}_i$  is the best individual position of the particle up to the current iteration;
- **g** is the best global position found by all particles in the swarm.

This mechanism allows the particles to explore the parameter space, balancing global exploration with local convergence toward optimal solutions.

In our study, the PSO was implemented using MATLAB®'s particleswarm function, adapted to the specific problem of fitting the parameters of a doped fiber laser. In particular, the fitting was performed considering one parameter at a time (e.g.,  $N_t$ ,  $\tau_{21}$ ,  $\sigma_{ap}$ ), while all other parameters were kept fixed at their nominal or previously optimized values. The objective function was defined as the SSE between the power values calculated by our model and those in the reference dataset provided by RP Photonics [38].

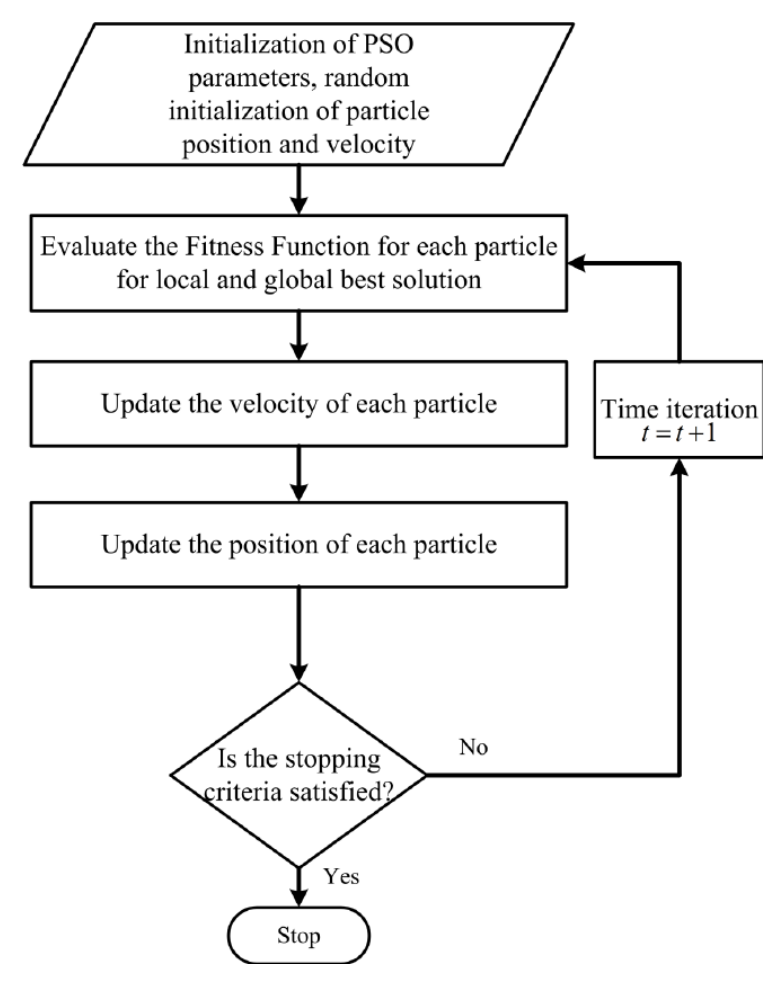


Figure 3.27: Flowchart illustrating the operation of the Particle Swarm Optimization algorithm as applied to the parameter fitting of a doped fiber laser.

3.7 Results 57

The flowchart in Fig. 3.27 summarizes the iterative procedure followed by the PSO algorithm. Each particle evaluates its fitness, updates its personal best, and collectively updates the global best, guiding the swarm toward the optimal solution for the parameter under consideration.

This approach allowed us to assess the influence of each parameter individually and to optimize the agreement between simulations and reference data, providing a reliable preliminary fitting before extending the method to actual experimental values in the following chapter.

### 3.7 Results

This section presents the results of the fitting procedure applied to the main spectroscopic parameters of the YDF laser model. The optimization was performed using the PSO algorithm, considering one parameter at a time while keeping the others fixed at their nominal or previously optimized values. For each parameter, the fitted curves are compared with reference data obtained from RP Fiber Power [38], considering different fiber lengths  $(2 \, \text{m}, 4 \, \text{m}, \text{ and } 8 \, \text{m})$  and output coupler reflectivities (R = 0.1, 0.3, 0.5). In addition to the comparison of simulated and reference power curves, the convergence of the (SSE) is reported to assess the stability and accuracy of the fitting procedure.

## 3.7.1 Fitting results for $N_t$

This subsection reports the fitting results for the active ion density  $N_t$ . The optimization converged to

$$N_t^* = 4.02 \times 10^{25} \text{ m}^{-3},$$

which is very close to the nominal value from the RP database, confirming the reliability of the reference data and the effectiveness of the PSO-based fitting.

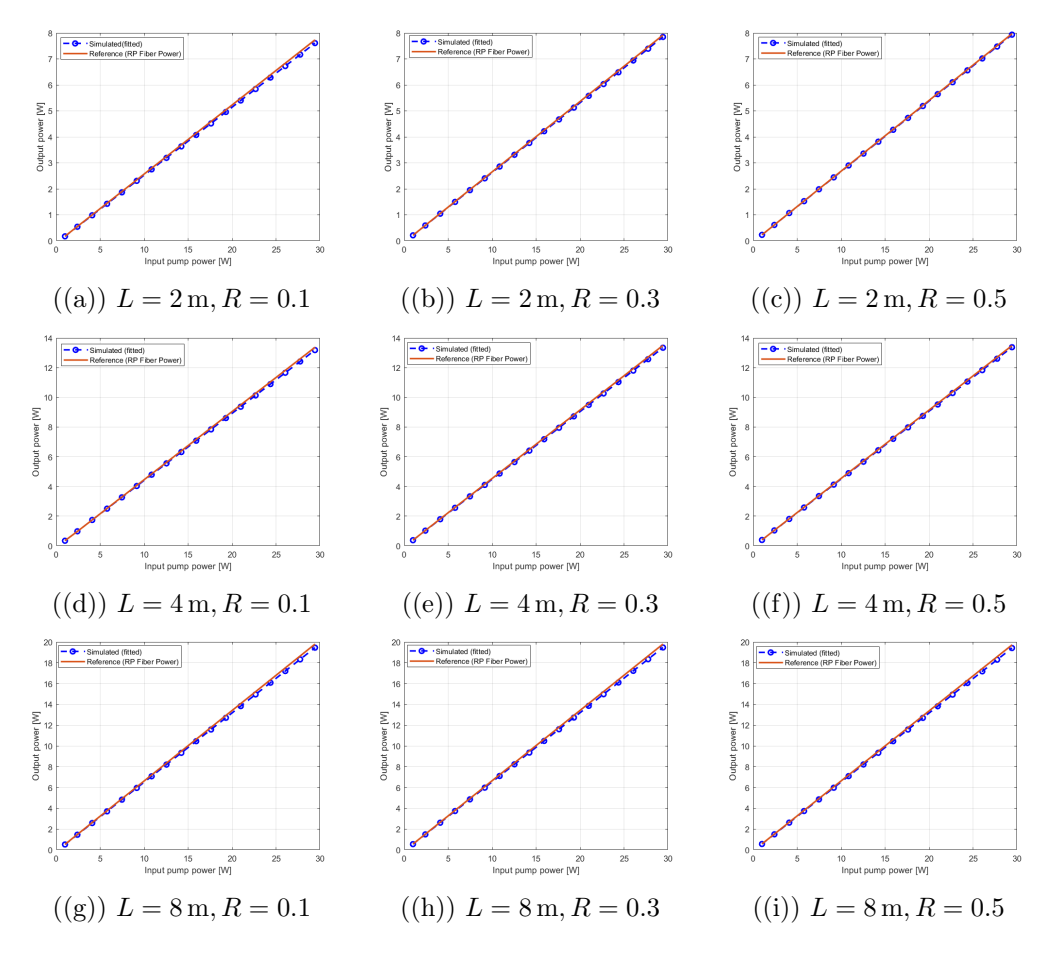


Figure 3.28: Fitting results for  $N_t$ : comparison of RP Fiber Power experimental data with theoretical and PSO-optimized simulated curves.

Figures 3.28 show the comparison between the reference data (RP Fiber Power), the theoretical model, and the optimized curves obtained through PSO. The analysis was carried out for three fiber lengths  $(2\,\mathrm{m},\,4\,\mathrm{m},\,8\,\mathrm{m})$  and three output couplers (R=0.1,0.3,0.5), for a total of nine cases. In all situations, the optimized curves closely follow the reference ones, with only minor deviations observed for short fibers and higher output coupling.

3.7 Results

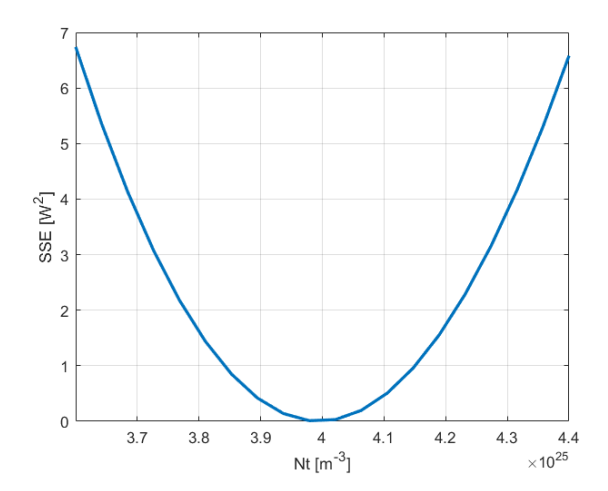


Figure 3.29: Behavior of the function error during the optimization of  $N_t$ . The convergence is reached around  $N_t^* = 4.02 \times 10^{25} \,\mathrm{m}^{-3}$ .

To further quantify the agreement between simulation and experiment, Fig. 3.29 reports the value of the error function over the considered parameter range. The error decreases rapidly and stabilizes after a few steps, indicating good convergence of the algorithm.

# 3.7.2 Fitting results for $\tau_{21}$

This subsection reports the fitting results for the lifetime parameter  $\tau_{21}$ . The optimization converged to

$$\tau_{21}^* = 8.4 \times 10^{-4} \text{ s},$$

which is slightly lower than the nominal value from the RP database,  $\tau_{21}^{\text{nom}} = 9.43 \times 10^{-4} \,\text{s}$ . Nevertheless, the fitting reproduces very well the experimental data, in agreement with the sensitivity analysis which showed that small variations in  $\tau_{21}$  have minor impact on the output curves.

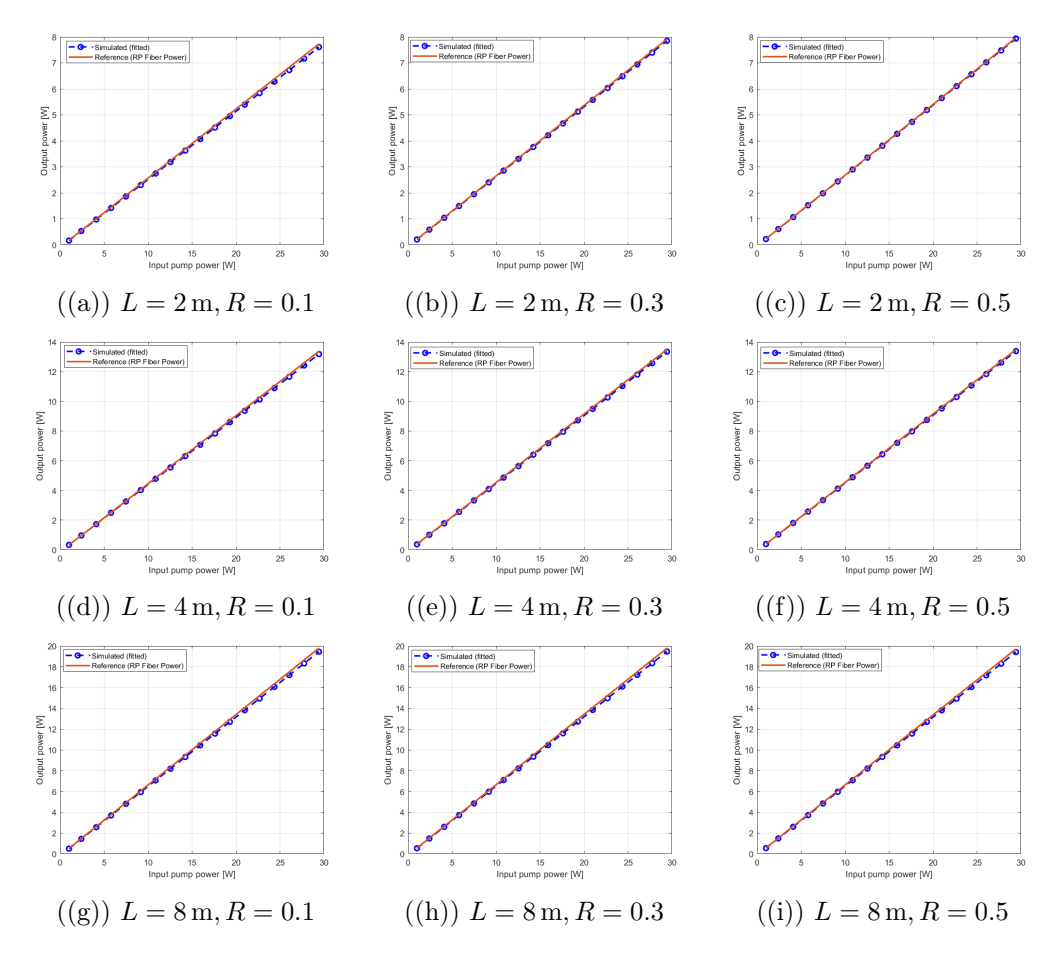


Figure 3.30: Fitting results for  $\tau_{21}$ : comparison of RP Fiber Power experimental data with theoretical and PSO-optimized simulated curves.

Figures 3.41 show the comparison between reference data, theoretical model, and PSO-optimized curves. The analysis was carried out for three fiber lengths (2 m, 4 m, 8 m) and three output couplers (R = 0.1, 0.3, 0.5), resulting in nine cases. In all situations, the optimized curves closely follow the reference ones, confirming the good performance of the fitting procedure despite the small difference from the nominal  $\tau_{21}$ .

3.7 Results 61

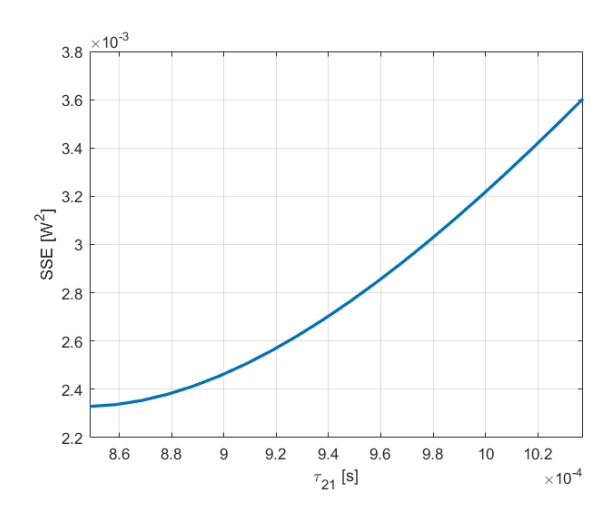


Figure 3.31: Behavior of the SSE during the optimization of  $\tau_{21}$ . The convergence is reached around  $\tau_{21}^* = 8.4 \times 10^{-4} \,\mathrm{s}$ .

Figure 3.31 shows the SSE over the considered range of  $\tau_{21}$ . The error decreases rapidly at first, reaching a minimum near the nominal starting value, then rises slightly before stabilizing. This pattern does not directly reflect the sensitivity of the output to small variations of  $\tau_{21}$ ; rather, it is due to the minimal difference between the resolution of the PSO in MATLAB® and that of the RP simulator. Despite the slight discrepancy from the nominal value, the optimized  $\tau_{21}$  produces fitted curves that accurately reproduce the reference data.

### 3.7.3 Fitting results for signal absorption and emission cross-sections

This subsection reports the fitting results for the signal absorption and emission cross-sections,  $\sigma_{as}$  and  $\sigma_{es}$ . Both parameters were optimized independently using PSO, while the other spectroscopic parameters were kept at their nominal or previously fitted values.

The optimization yielded

$$\sigma_{as}^* = 5.481 \times 10^{-27} \text{ m}^2,$$

slightly above the nominal RP database value,  $\sigma_{as}^{\text{nom}} = 5.13 \times 10^{-27} \,\text{m}^2$ . Despite this minor deviation, the simulated curves reproduce the experimental trends very accurately, confirming the robustness of the PSO-based procedure.

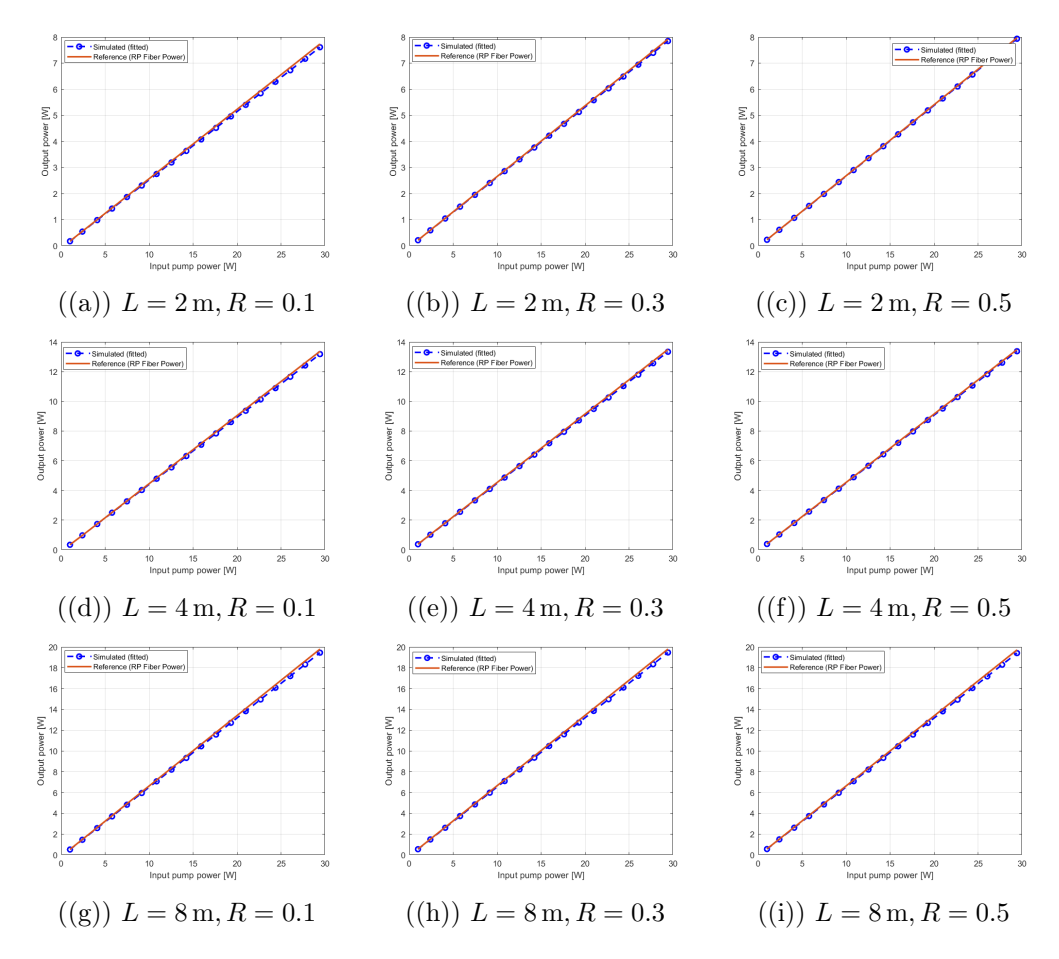


Figure 3.32: Fitting results for  $\sigma_{as}$ : comparison of RP Fiber Power experimental data with theoretical and PSO-optimized simulated curves.

For the signal emission cross-section, the optimization converged to

$$\sigma_{es}^* = 2.877 \times 10^{-25} \text{ m}^2,$$

3.7 Results 63

slightly below the nominal value,  $\sigma_{es}^{\text{nom}} = 3.02 \times 10^{-25} \,\text{m}^2$ . The PSO-optimized curves remain in excellent agreement with the experimental data, confirming the reliability of the fitting despite the minor adjustment of the parameter.

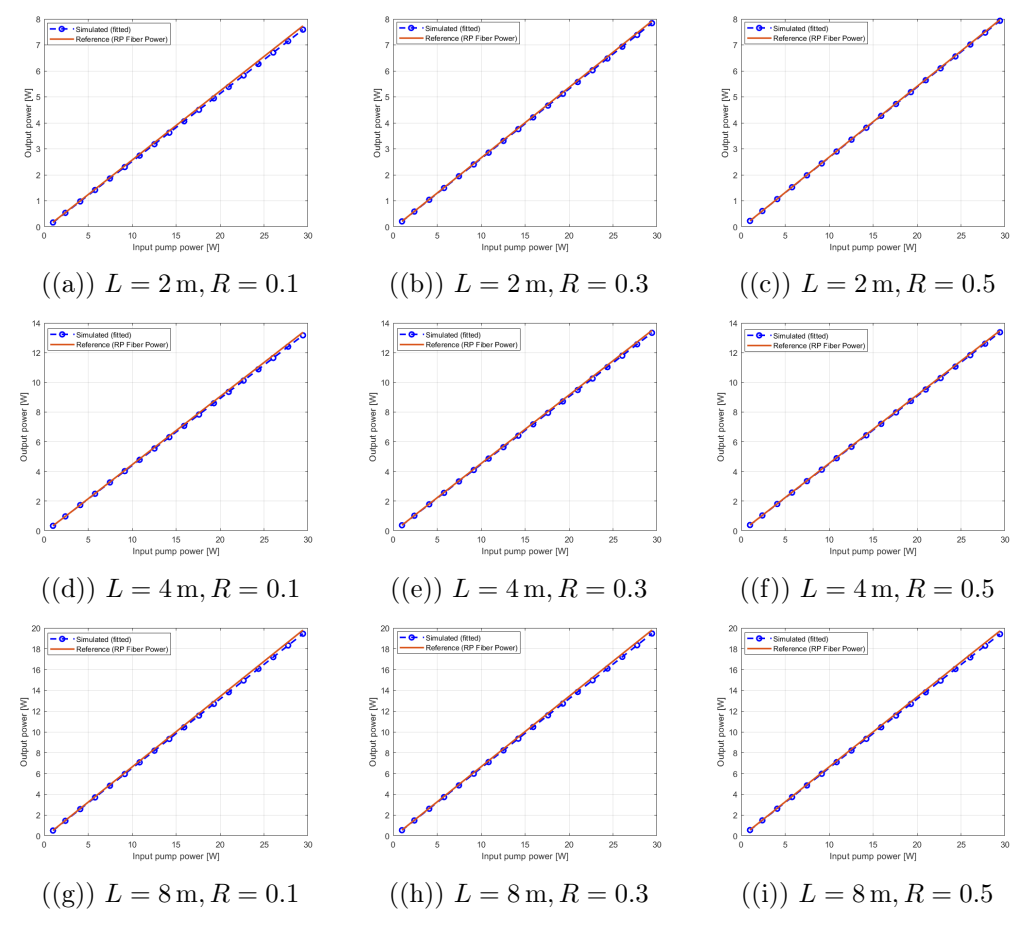


Figure 3.33: Fitting results for  $\sigma_{es}$ : comparison of RP Fiber Power experimental data with theoretical and PSO-optimized simulated curves.

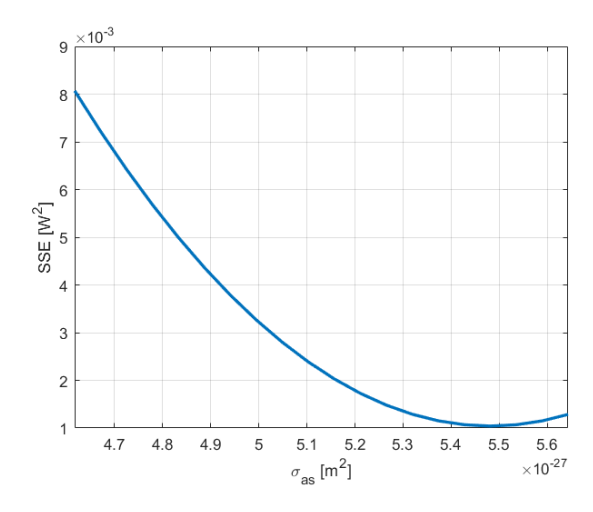


Figure 3.34: SSE behavior during the optimization of  $\sigma_{as}$ . Convergence is reached around  $\sigma_{as}^* = 5.481 \times 10^{-27} \,\mathrm{m}^2$ .

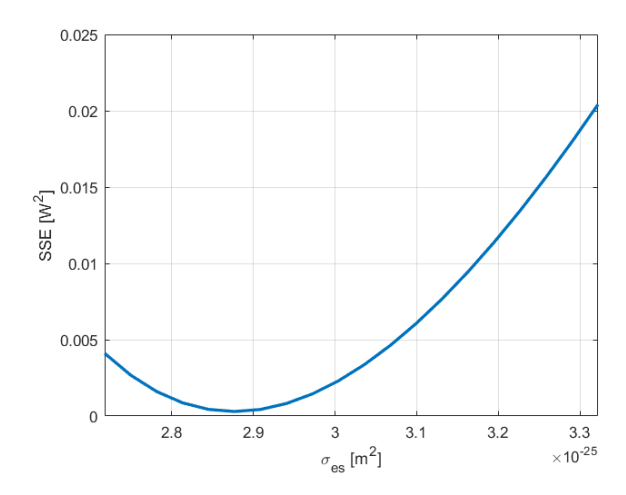


Figure 3.35: SSE behavior during the optimization of  $\sigma_{es}$ . The algorithm converges to  $\sigma_{es}^* = 2.877 \times 10^{-25} \,\mathrm{m}^2$ .

Overall, the optimizations of both  $\sigma_{as}$  and  $\sigma_{es}$  converge rapidly, as illustrated in Figs. 3.34, 3.35. The observed variations from the nominal values are small and largely reflect the minimal differences due to the resolution of the PSO in MATLAB® compared to the reference simulator, rather than the sensitivity of the output to these parameters. As was also observed for  $\tau_{21}$ , these small discrepancies do not compromise the fitting results: the fitted curves accurately reproduce the reference data, indicating that the optimization reliably captures the underlying fiber dynamics.

3.7 Results 65

4

## 3.7.4 Fitting results for pump absorption and emission cross-sections

This subsection presents the fitting results for the pump absorption and emission cross-sections,  $\sigma_{ap}$  and  $\sigma_{ep}$ . Both parameters were optimized independently with PSO, keeping all other spectroscopic parameters fixed.

The optimization converged to

$$\sigma_{ap}^* = 7.8 \times 10^{-25} \text{ m}^2,$$

which perfectly matches the nominal value from the RP database,  $\sigma_{ap}^{\text{nom}} = 7.8 \times 10^{-25} \,\text{m}^2$ . This demonstrates that the reference data for  $\sigma_{ap}$  are highly accurate and the fitting procedure reproduces the experimental power curves without any adjustment.

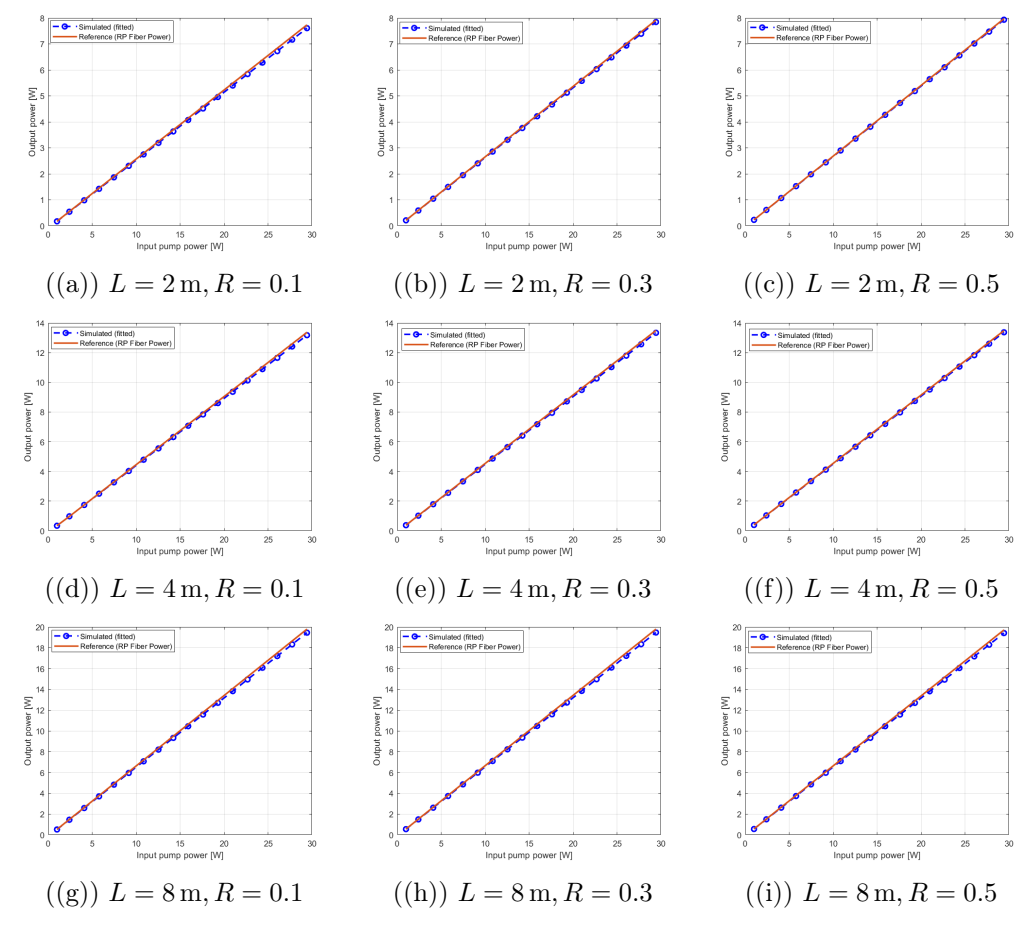


Figure 3.36: Fitting results for  $\sigma_{ap}$ : comparison of RP Fiber Power experimental data with theoretical and PSO-optimized simulated curves.

The optimization for the pump emission cross-section converged to

$$\sigma_{ep}^* = 4.8 \times 10^{-26} \text{ m}^2,$$

slightly higher than the nominal RP database value,  $\sigma_{ep}^{\text{nom}} = 3.8 \times 10^{-26} \,\text{m}^2$ . This small adjustment does not significantly affect the fitted power curves, as the sensitivity analysis previously showed that minor variations of  $\sigma_{ep}$  have a limited impact on the fiber output.

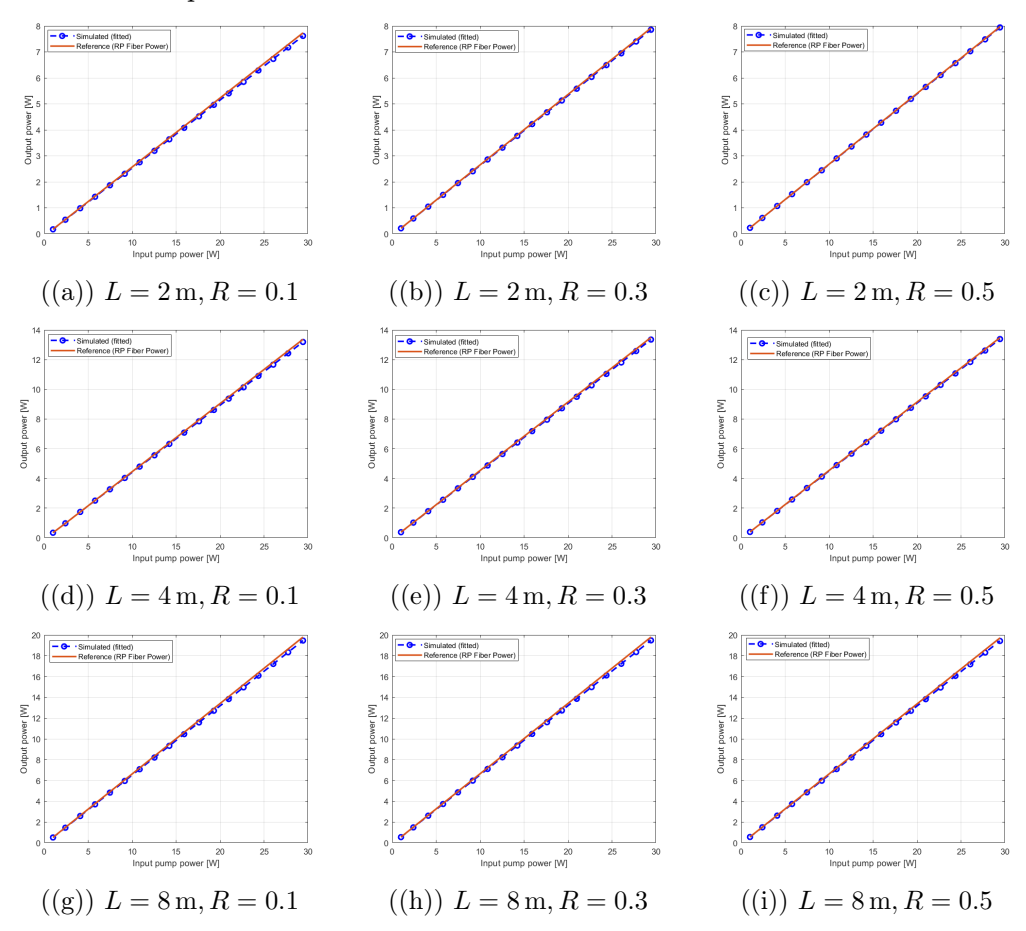


Figure 3.37: Fitting results for  $\sigma_{ep}$ : comparison of RP Fiber Power experimental data with theoretical and PSO-optimized simulated curves.

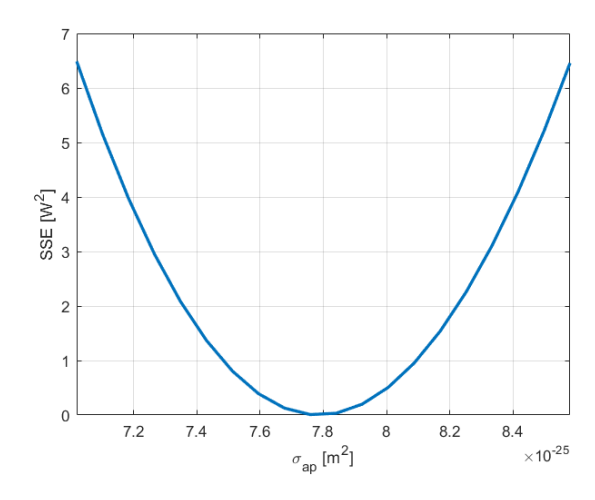


Figure 3.38: SSE behavior during the optimization of  $\sigma_{ap}$ . The algorithm converges perfectly to  $\sigma_{ap}^* = 7.8 \times 10^{-25} \,\mathrm{m}^2$ .

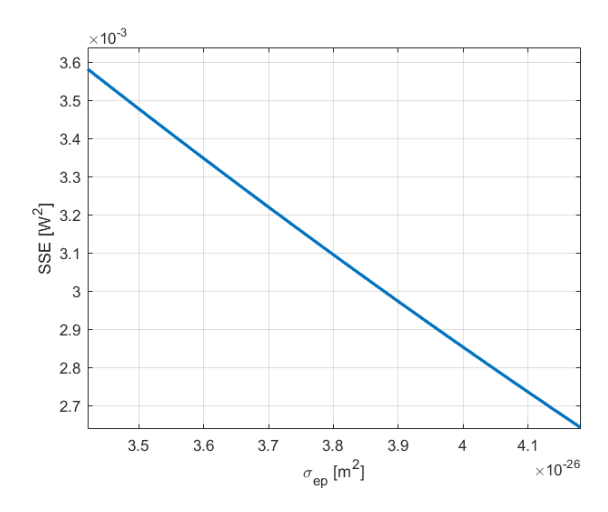


Figure 3.39: SSE behavior during the optimization of  $\sigma_{ep}$ . Convergence is reached at  $\sigma_{ep}^* = 4.8 \times 10^{-26} \,\mathrm{m}^2$ .

Overall, the optimizations of both pump cross-sections,  $\sigma_{ap}$  and  $\sigma_{ep}$ , show excellent agreement with the reference data. For  $\sigma_{ap}$ , the optimized value closely matches the nominal one, and the fitting has negligible effect on the output power curves. In the case of  $\sigma_{ep}$ , small discrepancies arise due to the limited resolution of the PSO in MATLAB® compared to the reference simulator, similar to what was observed for  $\tau_{21}$ . Despite these minor differences, the fitted curves accurately reproduce the reference data, confirming that the optimization procedure captures the pump dynamics reliably.

# 3.8 Fitting Analysis under Noisy Conditions

To assess the robustness of the fitting procedure under non-ideal experimental conditions, a sensitivity analysis was performed by introducing additive noise into the datasets used for optimization. This approach simulates a realistic measurement environment, where the recorded data may be affected by noise sources such as the power meter, the current driver, and other instrumentation limitations.

Specifically, starting from the original datasets, new data were generated by adding white Gaussian noise using the wgn function in MATLAB®, which allows introducing additive noise at a specified power level. In this study, a noise power of  $-10\,\mathrm{dBW}$  was applied, representing a deliberately severe condition to simulate a highly noisy experimental environment.

The noisy datasets were then used as input to repeat the entire optimization process via PSO. For each parameter of interest, the corresponding plots were generated for nine experimental cases, defined by the combinations of fiber length (L = 2 m, 4 m, 8 m) and output coupler reflectivity (OC = 0.1, 0.3, 0.5). This framework enabled

a systematic evaluation of the algorithm's performance in the presence of degraded measurements.

The following subsections report the detailed results obtained for each optimized parameter:

## • Results for $N_t$

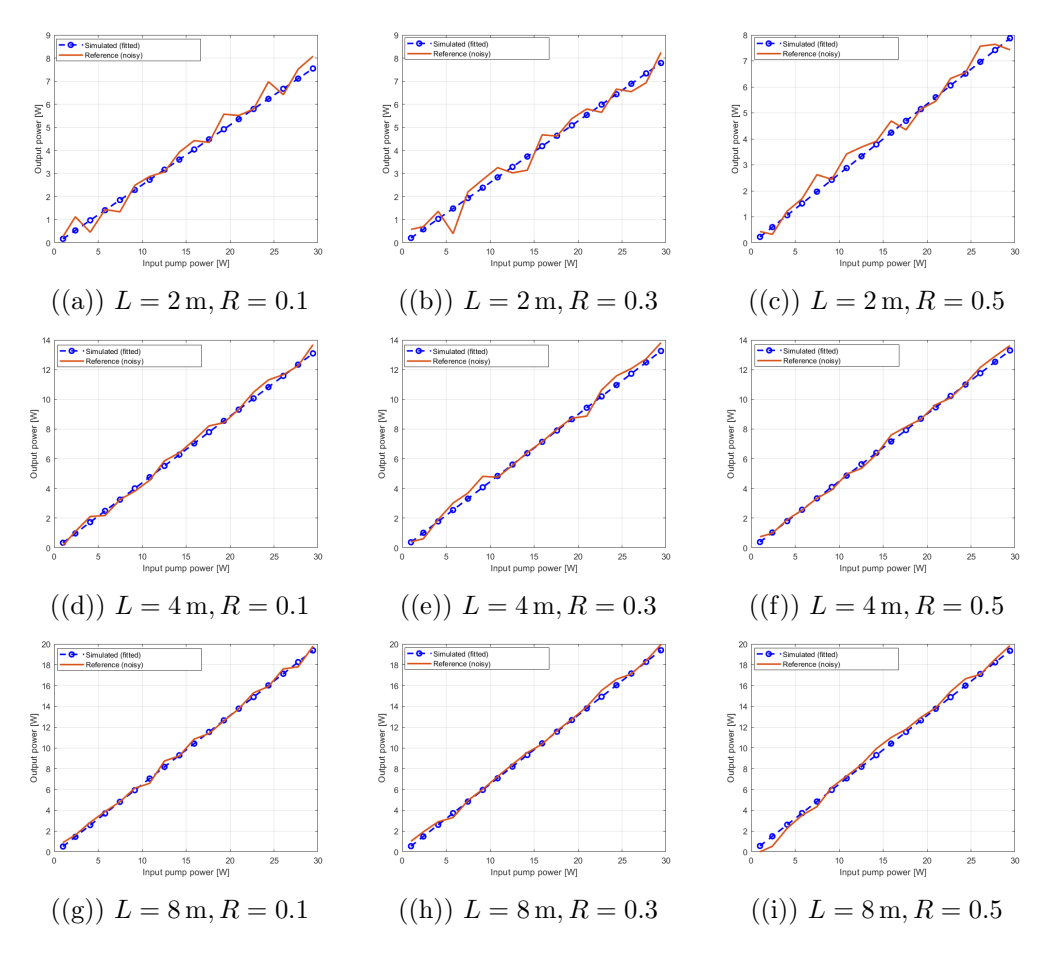


Figure 3.40: Fitting results for  $N_t$ : comparison of RP Fiber Power reference data with additive white Gaussian noise at a noise power of  $-10 \,\mathrm{dBW}$ , along with theoretical and PSO-optimized simulated curves.

# • Results for $\tau_{21}$

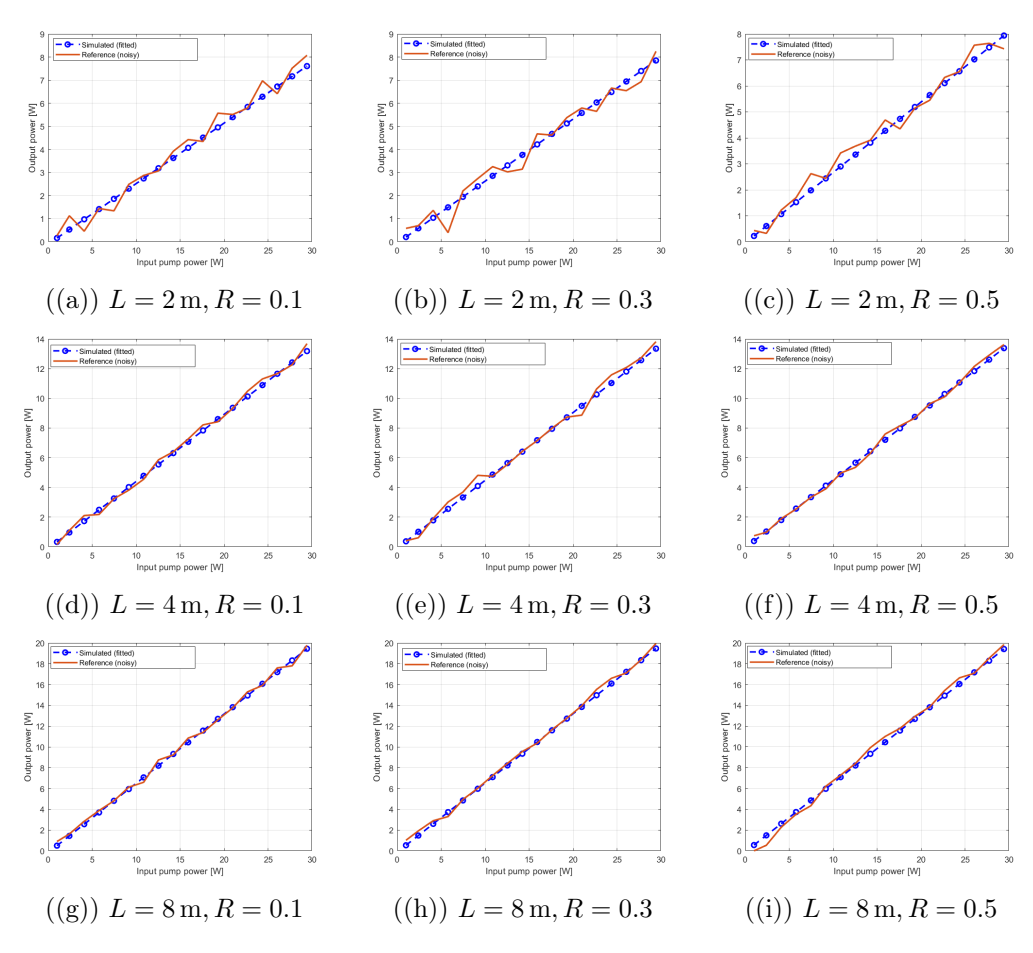


Figure 3.41: Fitting results for  $\tau_{21}$ :comparison of RP Fiber Power reference data with additive white Gaussian noise at a noise power of  $-10\,\mathrm{dBW}$ , along with theoretical and PSO-optimized simulated curves.

# • Results for $\sigma_{as}$

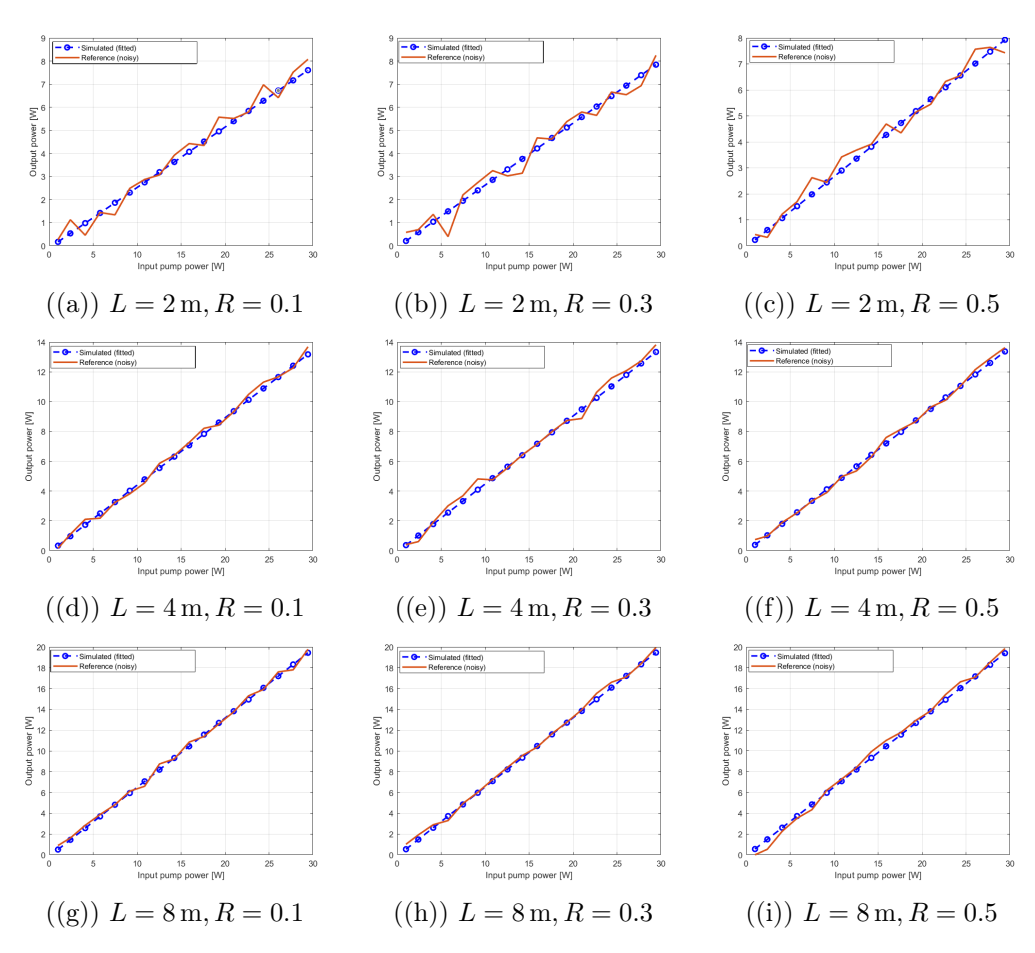


Figure 3.42: Fitting results for  $\sigma_{as}$ :comparison of RP Fiber Power reference data with additive white Gaussian noise at a noise power of  $-10\,\mathrm{dBW}$ , along with theoretical and PSO-optimized simulated curves.

# • Results for $\sigma_{es}$

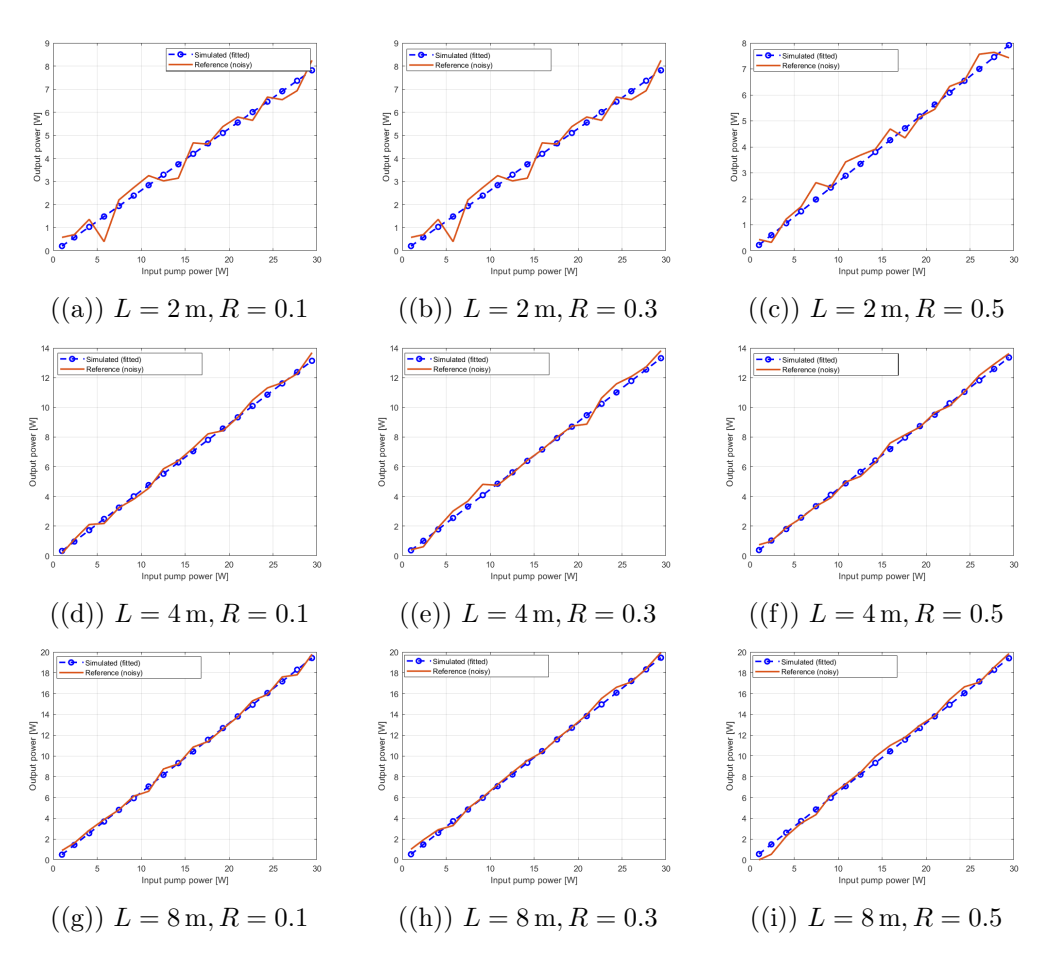


Figure 3.43: Fitting results for  $\sigma_{es}$ :comparison of RP Fiber Power reference data with additive white Gaussian noise at a noise power of  $-10\,\mathrm{dBW}$ , along with theoretical and PSO-optimized simulated curves.

# • Results for $\sigma_{ap}$

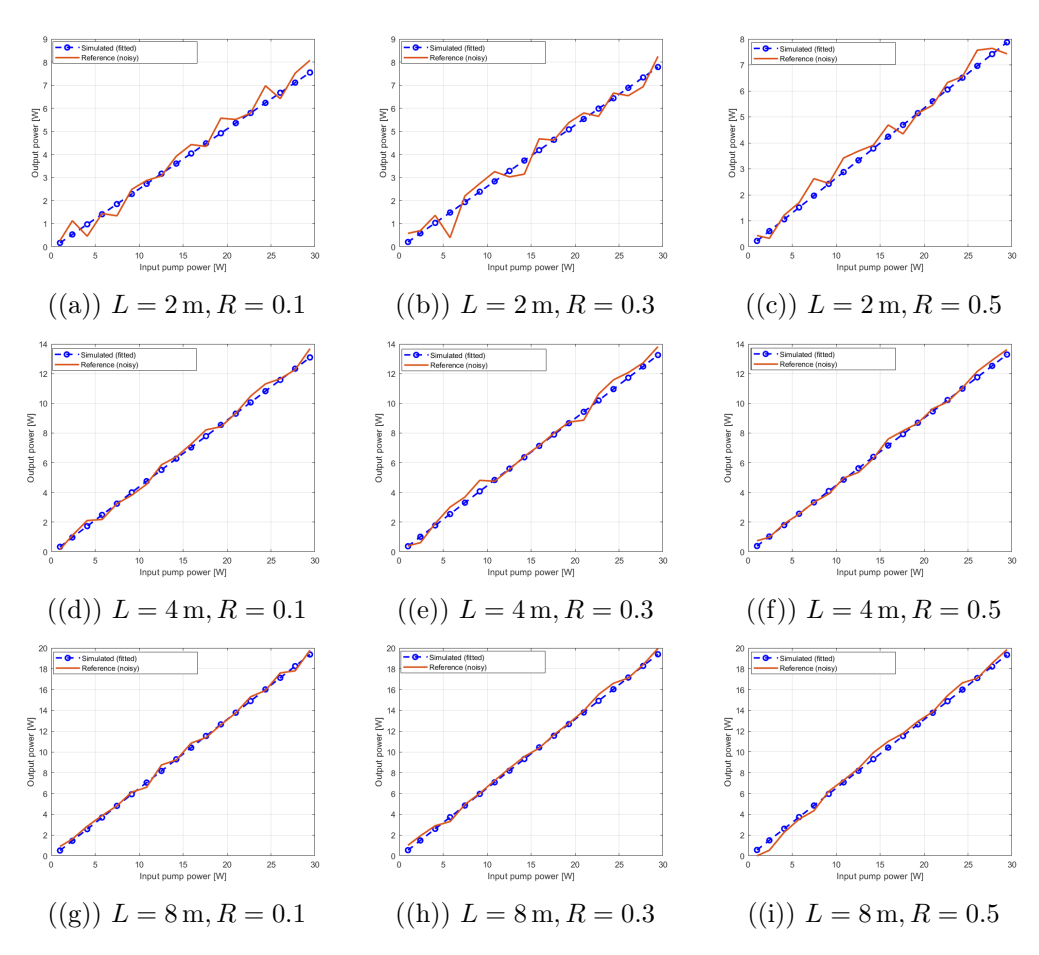


Figure 3.44: Fitting results for  $\sigma_{ap}$ :comparison of RP Fiber Power reference data with additive white Gaussian noise at a noise power of  $-10\,\mathrm{dBW}$ , along with theoretical and PSO-optimized simulated curves.

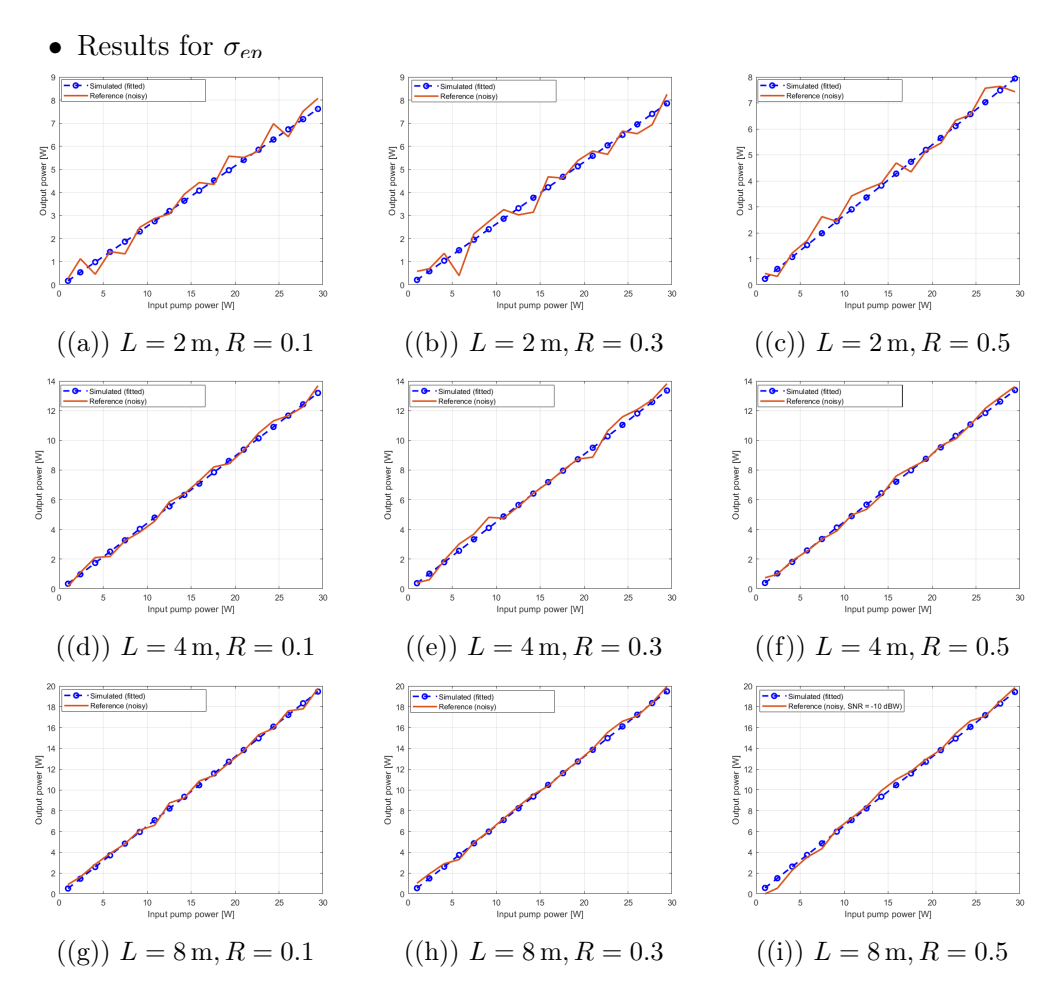


Figure 3.45: Fitting results for  $\sigma_{ep}$ : comparison of RP Fiber Power reference data with additive white Gaussian noise at a noise power of  $-10 \,\mathrm{dBW}$ , along with theoretical and PSO-optimized simulated curves.

The analysis shows that, although in some cases spurious spikes or larger deviations from the reference data may appear, the overall trend of the optimized curves remains in good agreement with the expected behavior. These results indicate that the fitting procedure maintains an acceptable degree of reliability even under challenging experimental conditions, confirming the robustness of the proposed method.

Additionally, it can be observed that, for all parameters, the ones expected to have the largest impact, such as  $N_t$  and the absorption/emission cross sections, still dominate the system's behavior. However, more pronounced deviations are noticed for simulations corresponding to the shortest fiber length  $(2\,\mathrm{m})$ . This trend appears largely independent of the output coupler used and is consistent with previous sensitivity studies. A plausible explanation is that, for shorter fibers, the reduced interaction length between pump and signal results in lower signal powers along the fiber, making the relative contribution of noise—whether from instrumentation or

numerical fluctuations—more significant. Consequently, the signal-to-noise ratio is effectively lower, and local variations have a stronger impact on the simulated curves.

# Chapter 4

# Experimental Validation of the Simulation Model

After testing the proposed model with reference data from RP Fiber Power, the next step is to evaluate its reliability against measurements carried out in our laboratory. The purpose of this experimental activity is not limited to the characterization of the laser setup, but rather to provide an independent dataset on which the simulation code can be tested and fitted. In this way, it is possible to assess whether the model is capable of reproducing realistic operating conditions and not just idealized or literature-based scenarios.

To this end, we realized several ytterbium-doped fiber laser cavities, varying both the length of the active fiber and the reflectivity of the output coupler. Each configuration was assembled, measured, and analyzed in terms of output power and spectral behavior. Particular care was devoted to minimizing insertion losses by means of programmable splicing and cleaving, which ensured both lower attenuation and higher repeatability compared to connectorized solutions.

The collected measurements thus represent a benchmark for the fitting procedure: by comparing the experimental results with the simulations, we can evaluate to what extent the model captures the actual behavior of the system under different conditions.

# 4.1 Experimental Setup

The experimental setup was designed to validate the numerical model through systematic measurements under different cavity configurations. The main elements of the setup are listed below:

- **Pump source.** A high-power diode module (nLight, model e06.0580915105) operating at 920 nm was employed as the pump source. The choice of this wavelength is motivated by its favorable absorption in ytterbium-doped fibers, already discussed in the previous chapters.
- Power supply. The diode module was driven by a laboratory current supply, which allowed control of the injected current and therefore of the pump power delivered to the fiber.
- Thermal management. Proper heat dissipation was ensured by combining a chiller and a cold plate. The chiller circulated cooling fluid through the cold plate, on which the pump module was mounted, maintaining its temperature within safe operating limits. This solution prevented thermal drift of the pump wavelength and ensured stable and repeatable experimental conditions.
- Active fiber. The gain medium consisted of a double-clad ytterbium-doped fiber (YB1200-10/125 DC). Different cavity lengths were prepared from this fiber in order to investigate how the laser performance depends on the active length.
- Fiber Bragg gratings (FBGs). The cavity mirrors were realized by inscribing Bragg gratings on passive fibers using a femtosecond laser. A high-reflectivity (HR) grating was positioned at the pump-input side of the active fiber, while on the opposite side either an output coupler (OC) grating with controlled reflectivity was employed or, alternatively, the Fresnel reflection from the cleaved fiber facet was used as partial reflector. This approach enabled the study of different cavity configurations.
- Splicing and cleaving. All gratings and active fibers were joined using programmable splicing and cleaving equipment. This approach significantly reduced splice losses and improved repeatability compared to connectorized solutions, which are more prone to insertion losses and misalignment.
- **Dichroic mirror.** A long-pass dichroic mirror (LP 900 nm) was used to separate the residual pump from the laser signal, allowing independent analysis of the amplified signal power.

- Collimating optics. A plano-convex lens (Thorlabs LA 1805-A, focal length f=30 mm, N-BK7, AR-coated) was employed to collimate the output beam before the power measurement. This ensured a stable and well-defined spot on the detector, minimizing fluctuations during acquisition.
- Power measurement. Output power was recorded using a thermal power sensor (Thorlabs S350C), suitable for high-power laser measurements and insensitive to beam profile variations. The measurement was performed at the OC side, where both the amplified signal and residual pump were collected.

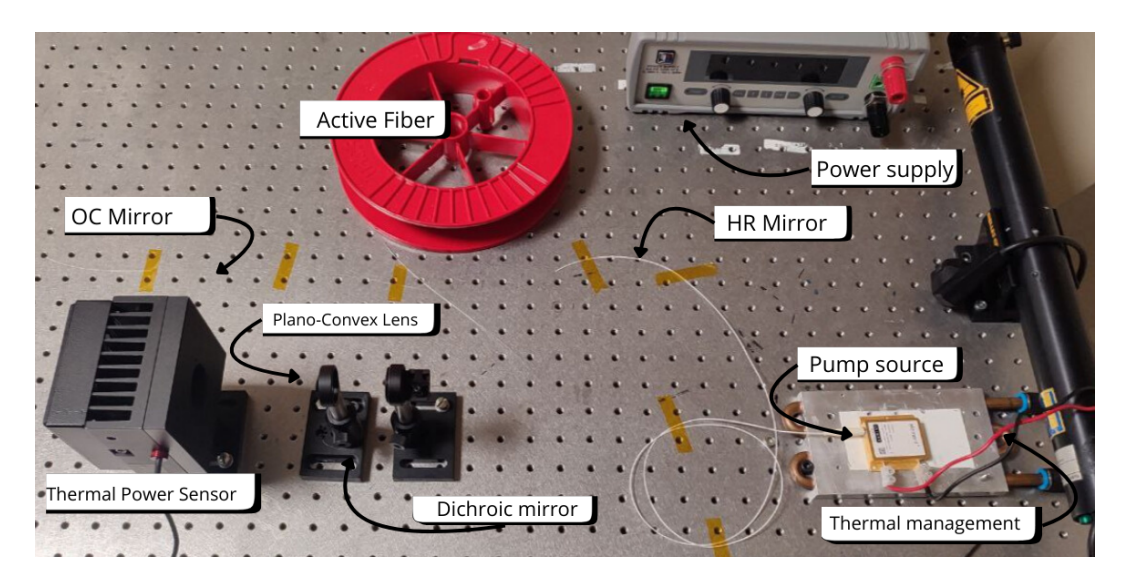


Figure 4.1: Schematic of the experimental setup. The main components are: pump diode (pump source), current supply (power supply), chiller and cold plate (Thermal management), active fiber (Yb-DC), high-reflectivity (HR) grating, output coupler (OC), dichroic mirror, collimating lens (plano-convex lens), and power meter (Thermal power sensor).

Figure 4.1 shows an image of the experimental setup, where all the components described above can be recognized in their actual arrangement on the optical bench.

# 4.2 Sample Configurations

In order to validate the numerical model, a series of YDFA cavities were assembled by combining different reflector terminations with active fibers of varying lengths. The aim of this experimental campaign was not limited to the observation of laser operation under diverse cavity designs, but primarily to generate independent datasets to be compared with the simulations through the fitting procedure. In this way, the model could be tested against realistic conditions, ensuring that its predictions are not restricted to idealized or literature-based cases.

The following subsections describe the optical components employed and the investigated cavity layouts. Active fibers with lengths of 25 m, 15 m, 10 m, and 5 m were tested, each terminated on the pump-input side by a common High-Reflectivity (HR) grating. On the output side, three types of reflectors were considered: two Output Coupler (OC) gratings with reflectivities of R=0.60 and R=0.29, and the Fresnel reflection from a cleaved facet ( $R\approx0.04$ ).

It is worth noting that not all combinations could be tested experimentally: in particular, the longest active fiber (25 m) exhibited strong ASE, which limited the set of feasible measurements with the different OCs. Despite these constraints, the chosen set of samples provides a representative overview of the cavity behavior and, most importantly, a reliable basis for assessing the accuracy of the simulation model through spectral comparison and fitting.

### 4.2.1 Fiber Bragg Gratings

The cavity mirrors were realized through the inscription of Fiber Bragg Gratings (FBGs) on passive fibers using a femtosecond laser. This technique ensures precise control over the reflection spectrum while avoiding the thermal effects typical of other inscription methods. In our work, three different types of reflectors were considered:

• High-Reflectivity (HR) grating. Positioned at the pump-input side of the active fiber, the HR served as the back mirror of the cavity. The measured reflection spectrum exhibited an attenuation of approximately 9 dB, corresponding to a reflectivity close to unity.

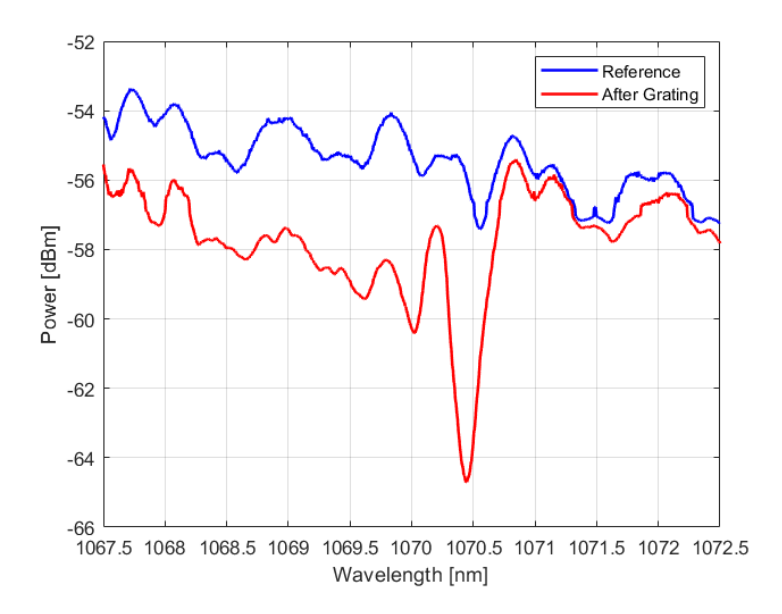


Figure 4.2: Reflection spectrum of the HR grating, showing a peak attenuation of about  $9\,\mathrm{dB}$ .

- Output Coupler (OC) gratings. Two gratings with different reflectivity levels were inscribed in passive fibers to act as the output mirror of the cavity:
  - OC<sub>1</sub>: reflectivity  $R \approx 0.29$ , with a measured spectral attenuation of about 1.5 dB.

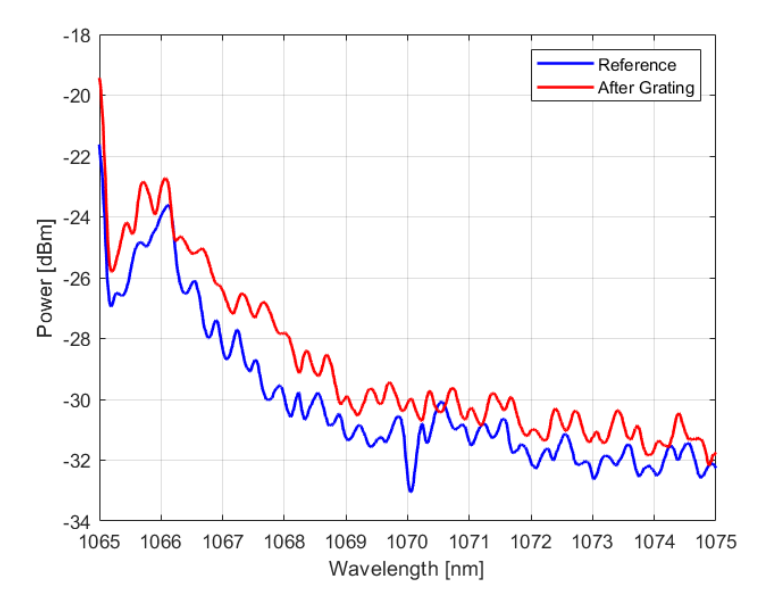


Figure 4.3: Reflection spectrum of the OC grating with reflectivity  $R\approx 0.29~(\sim 1.5\,\mathrm{dB}$  attenuation).

– OC<sub>2</sub>: reflectivity  $R \approx 0.60$ , with a measured spectral attenuation of about 4 dB.

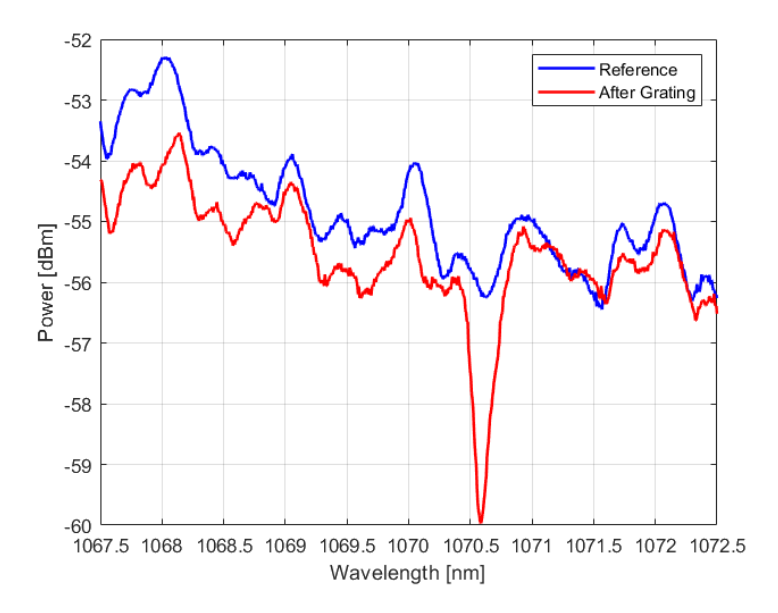


Figure 4.4: Reflection spectrum of the OC grating with reflectivity  $R \approx 0.60$  ( $\sim 4\,\mathrm{dB}$  attenuation).

• Fresnel reflection. As a third configuration, no grating was employed on the output side, and the cavity relied on the natural Fresnel reflection from the cleaved fiber facet, corresponding to a reflectivity of approximately  $R \approx 0.04$ . In this case, no reflection spectrum was recorded, since the termination does not involve an inscribed grating.

The measured spectra of the gratings are reported in Figs. 4.2, 4.3, and 4.4. While some variations are observed, the overall reflectivity levels are consistent with the target design values, ensuring their applicability in the experimental cavities.

### 4.2.2 Spectral Measurements of the Assembled Cavities

After characterizing the individual Fiber Bragg Gratings, the next step consisted in recording the emission spectra of the assembled laser cavities. These measurements allow evaluating the spectral behavior of the laser signal, the presence of amplified spontaneous emission (ASE), and the effect of different cavity configurations. In all cases, the pump current was limited to 4A to avoid excessive ASE that would compromise the quality of the measurements. For clarity, the results are presented according to the active fiber length of the sampled cavities:

• Cavity with 25 m active fiber: Two configurations were investigated:

– HR + Fresnel (R  $\approx 0.04$ ): The spectrum shows a signal peak around 1070 nm, while ASE is already noticeable at longer wavelengths ( $\lambda > 1090$  nm). The pump current was set to 4 A.

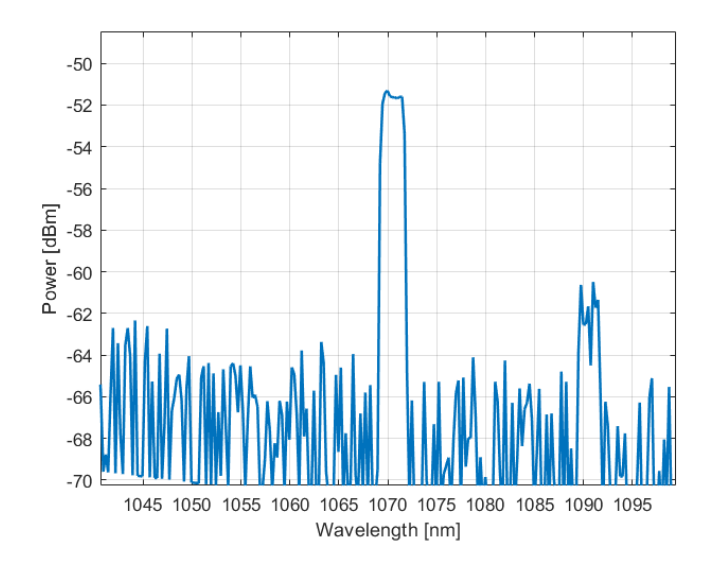


Figure 4.5: Emission spectrum of the  $25\,\mathrm{m}$  cavity with HR + Fresnel termination. The signal peak is visible around  $1070\,\mathrm{nm}$ , while ASE appears at longer wavelengths.

- HR + OC (R = 0.60): In this configuration, the ASE contribution becomes even stronger, almost exceeding the signal itself, again measured with a pump current of 4 A. This indicates that the fiber length is already excessive relative to the optimal length.

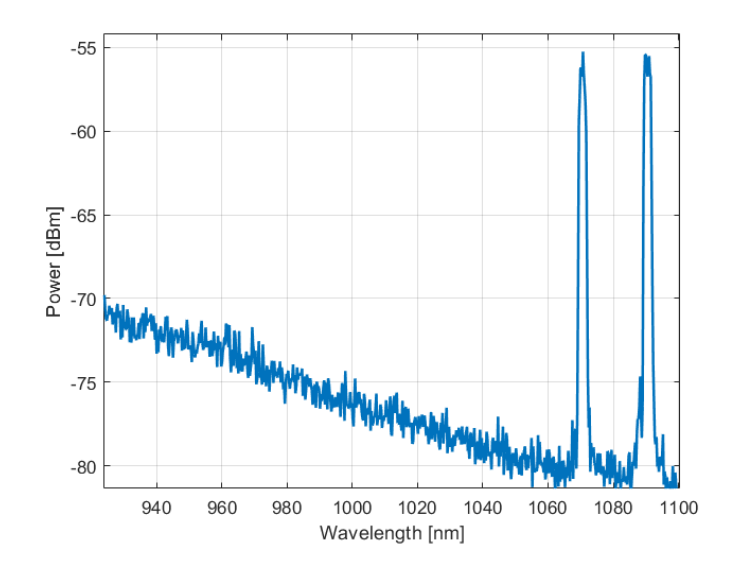


Figure 4.6: Emission spectrum of the  $25\,\mathrm{m}$  cavity with HR + OC (R = 0.60). The ASE contribution is dominant relative to the signal peak.

Only the first sample (Figs. 4.5) was considered for analysis, as the second sample was too noisy to provide a clean dataset for simulation validation.

- Cavity with 15 m active fiber: Two cavity configurations were analyzed, both employing the HR grating at one end:
  - HR + Fresnel (R  $\approx 0.04$ ): The spectrum shows a strong lasing peak centered at 1070 nm, without evidence of ASE at longer wavelengths. The measurement was performed at a pump current of 4 A.

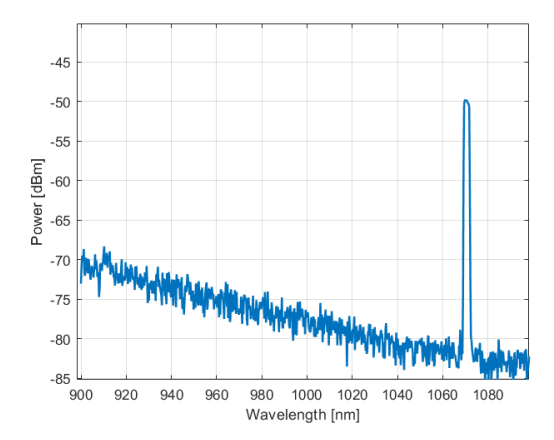


Figure 4.7: Emission spectrum of the 15 m cavity with HR + Fresnel termination (R  $\approx 0.04$ ). The lasing peak is at 1070 nm .

- HR + OC (R = 0.60): The output spectrum is qualitatively similar, with a dominant lasing peak at 1070 nm and no significant ASE contribution. Also in this case, the residual pump at 920 nm is observed. The pump current was kept at 4 A.

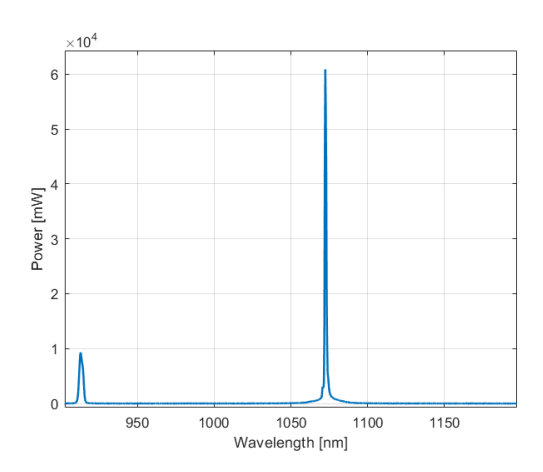


Figure 4.8: Emission spectrum of the 15 m cavity with HR + OC (R = 0.60). The spectrum is dominated by the lasing line at  $1070 \,\mathrm{nm}$ , while the pump residual at  $920 \,\mathrm{nm}$  remains visible.

### • Cavity with 10 m active fiber:

Three samples were characterized, all terminated on the pump-input side by the HR grating, and with different output reflectors:

- HR + Fresnel reflection (R  $\approx 0.04$ ): The spectrum is dominated by the lasing emission around 1070 nm, together with a residual pump contribution at 920 nm. No evidence of ASE is observed in this configuration.

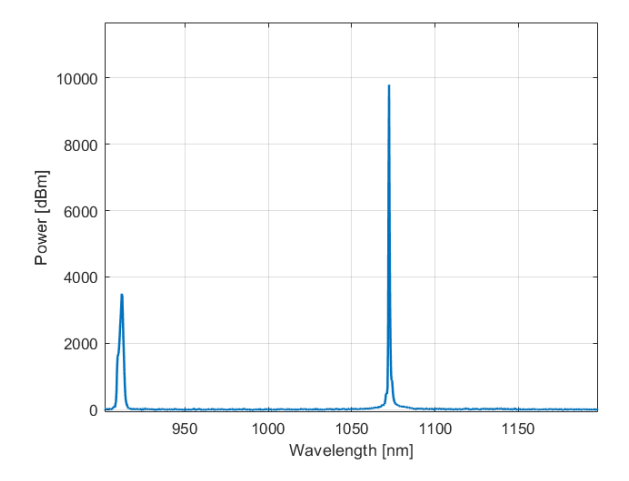


Figure 4.9: Emission spectrum of the 10 m cavity terminated by HR + Fresnel reflection (R  $\approx 0.04$ ). The lasing line at 1070 nm is accompanied by a residual pump peak at 920 nm.

- HR + OC (R = 0.29): In this case the lasing peak at 1070 nm is clearly observed, while the residual pump contribution is not visible. As for the other samples at this length, no ASE was detected.

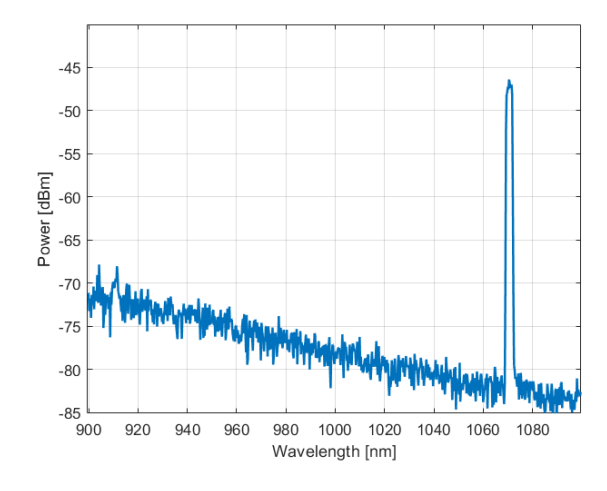


Figure 4.10: Emission spectrum of the  $10 \,\mathrm{m}$  cavity terminated by HR + OC (R = 0.29). The lasing line at  $1070 \,\mathrm{nm}$  is observed without significant pump residual.

• HR + OC (R = 0.60): The spectrum shows the lasing peak at 1070 nm, together with the residual pump signal at 920 nm. Again, no ASE contribution is detected.

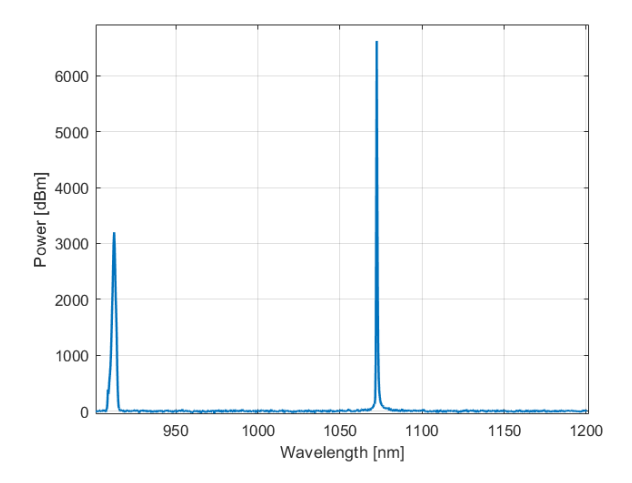


Figure 4.11: Emission spectrum of the  $10\,\mathrm{m}$  cavity terminated by HR + OC (R = 0.60). The lasing emission at  $1070\,\mathrm{nm}$  coexists with the residual pump at  $920\,\mathrm{nm}$ .

- Cavity with 5 m active fiber: Three configurations were investigated, all employing the HR grating on the pump-input side, while different terminations were applied at the output facet. This fiber length proved to be the most effective among the tested ones, as the spectra display a clean laser emission without residual pump peaks or significant ASE contributions.
  - HR + Fresnel reflection (R  $\approx 0.04$ ): The emission spectrum exhibits a well-defined laser line at 1070 nm, with no detectable residual pump signal and negligible ASE.

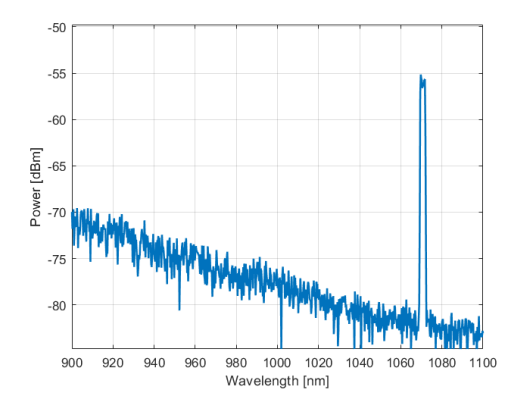


Figure 4.12: Emission spectrum of the 5 m cavity terminated by HR + Fresnel reflection (R  $\approx 0.04$ ). A clean lasing line is observed at 1070 nm, without pump or ASE.

-  $\mathbf{HR} + \mathbf{OC}$  ( $\mathbf{R} = \mathbf{0.29}$ ): The spectrum confirms once again the efficient operation of the cavity: the lasing peak at 1070 nm is sharp and isolated, with no measurable ASE background or pump leakage.

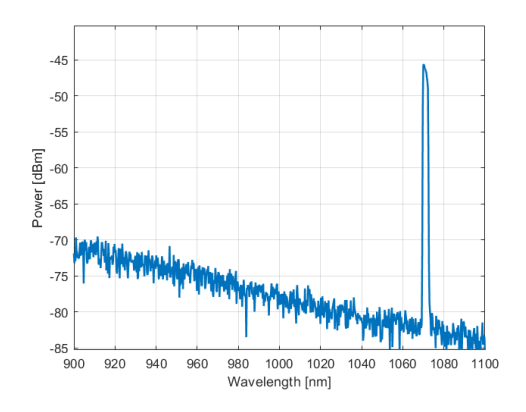


Figure 4.13: Emission spectrum of the  $5\,\mathrm{m}$  cavity terminated by HR + OC (R = 0.29). The laser emission at  $1070\,\mathrm{nm}$  is clearly visible without other contributions.

- HR + OC (R = 0.60): Also in this case the laser operates stably at 1070 nm, with no spectral features related to ASE or residual pump light.

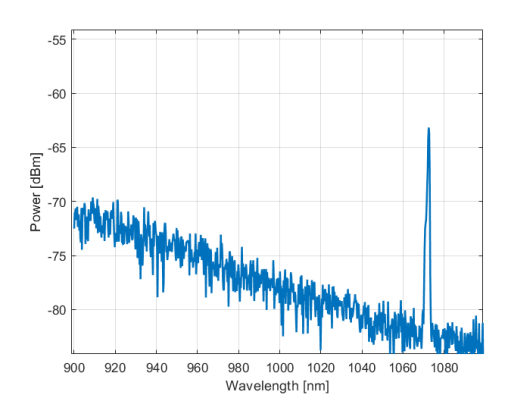


Figure 4.14: Emission spectrum of the  $5\,\mathrm{m}$  cavity terminated by HR + OC (R = 0.60). The spectrum shows only the lasing emission at  $1070\,\mathrm{nm}$ .

# 4.3 Experimental measurements

The first step of the experimental campaign was the characterization of the pump diode module, where the output power was recorded for different driving currents. Subsequently, we carried out measurements on the assembled cavities with the high-reflectivity (HR) grating and the different output couplers (OC), depending on the considered sample. The procedure involved the direct measurement of the combined  $signal + residual\ pump$  power, followed by the insertion of a dichroic mirror to isolate the laser signal. By subtracting this value from the total power, we retrieved the residual pump contribution.

## 4.3.1 Pump diode characterization

The output power of the pump diode was measured at different driving currents. The results are summarized in Table 4.1.

Table 4.1: Characterization of the pump diode module.

Current [A]	Output Power [W]
1	3.00
2	9.07
3	14.72
4	20.19

#### 4.3.2 Cavity measurements

For each sample, we measured the output powers under the different cavity configurations. Tables 4.2, 4.3, 4.4, and 4.5 report the results corresponding to the fibers of length  $25\,\mathrm{m}$ ,  $15\,\mathrm{m}$ ,  $25\,\mathrm{m}$ , and  $5\,\mathrm{m}$ , respectively.

Table 4.2: Measured powers for the 25 m fiber samples.

Configuration	Total [W]	Signal [W]	Residual Pump [W]
HR + Fresnel (R = 0.04)	3.0	0.59	0.18
	9.07	3.2	0.1
	14.72	5.86	0.09
	20.19	8.1	0.1

Total [W] Signal [W] Residual Pump [W] Configuration HR + Fresnel (R = 0.04)1.27 3.0 0.03 9.074.640.0614.727.9 0.320.1911.14 0.46HR + OC(R = 0.60)3.0 0.590.089.072.240.2614.724.950.1220.19 6.670.17

Table 4.3: Measured powers for the 15 m fiber samples.

Table 4.4: Measured powers for the 10 m fiber samples.

Configuration	Total [W]	Signal [W]	Residual Pump [W]
HR + Fresnel (R = 0.04)	3.0	1.46	0.18
	9.07	5.11	0.44
	14.72	8.8	0.8
	20.19	13.03	1.97
HR + OC(R = 0.29)	3.0	1.28	0.17
	9.07	4.42	0.35
	14.72	7.53	0.48
	20.19	10.6	0.7
HR + OC(R = 0.60)	3.0	0.7	0.07
	9.07	2.5	0.8
	14.72	5.19	0.55
	20.19	6.74	0.66

Table 4.5: Measured powers for the 5 meter fiber samples.

Configuration	Total [W]	Signal [W]	Residual Pump [W]
HR + Fresnel (R = 0.04)	3.0	1.5	0.6
	9.07	5.3	1.74
	14.72	9.07	2.83
	20.19	12.8	3.85
HR + OC(R = 0.29)	3.0	1.21	0.49
	9.07	4.18	1.62
	14.72	7.59	2.61
	20.19	10.3	3.76
HR + OC(R = 0.60)	3.0	0.62	0.69
	9.07	2.5	3.78
	14.72	4.7	5.9
	20.19	5.9	8.3

# 4.4 Fitting Results

After having characterized the emission spectra of all the realized cavities, the next step is to quantitatively compare the measured input—output characteristics with the corresponding simulated curves. This analysis allows verifying whether the developed model can accurately reproduce the experimental behavior and, through optimization, retrieve internal parameters. Among the different fitting strategies tested, the optimization of the splice losses at the HR and OC interfaces proved to be the most effective and physically meaningful. These losses were assumed to be approximately equal, introducing a single parameter  $\alpha_{\rm splice}$  common to both gratings. The following figures show, for each cavity, the comparison between the experimental data and the simulated model before and after the PSO optimization.

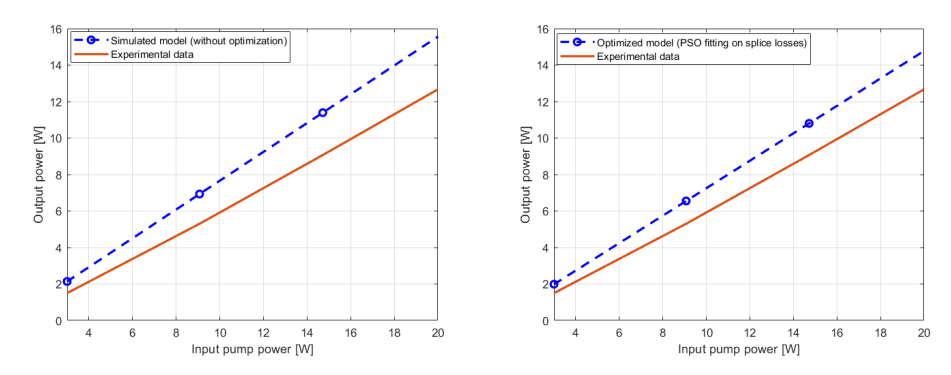


Figure 4.15: Comparison between experimental data and simulated model for  $5 \,\mathrm{m}$ , R = 0.04: (left) before and (right) after PSO optimization on splice losses.

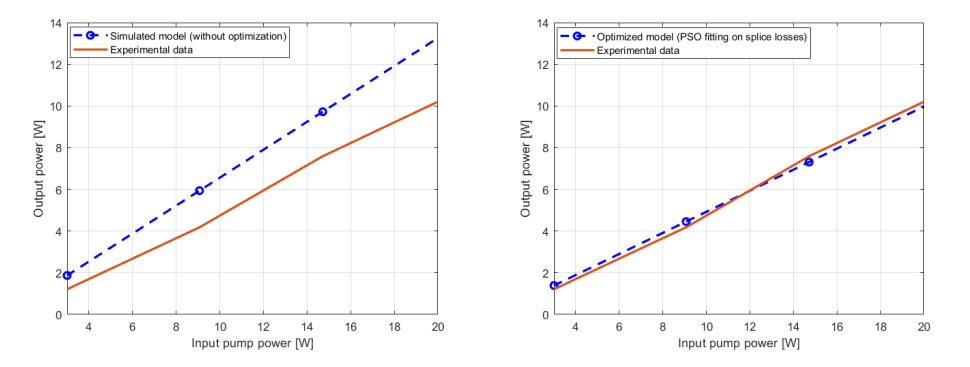


Figure 4.16: Comparison between experimental data and simulated model for L=5 m, R=0.29: (left) before and (right) after PSO optimization on splice losses.

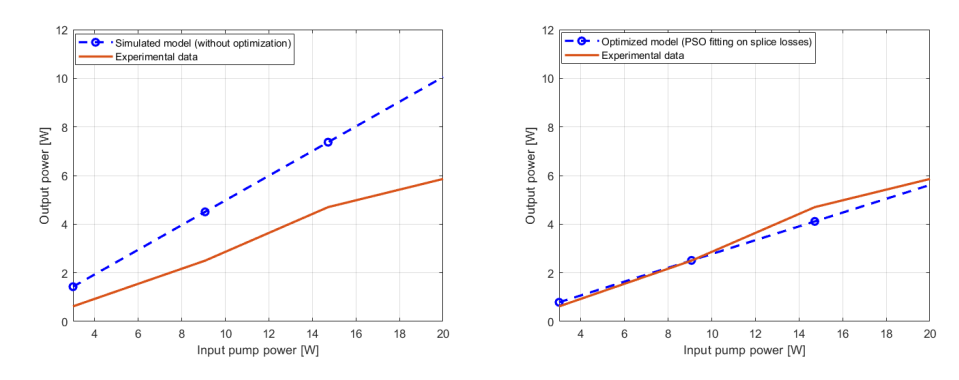


Figure 4.17: Comparison between experimental data and simulated model for L=5 m, R=0.60: (left) before and (right) after PSO optimization on splice losses.

As shown in Figs. 4.15, 4.16, 4.17, for the 5 m cavities the fitting quality is already reasonable before optimization and becomes excellent after applying the PSO.

After analyzing the behavior of the 5 m cavities, attention is now directed to the configurations with 10 m active fiber:

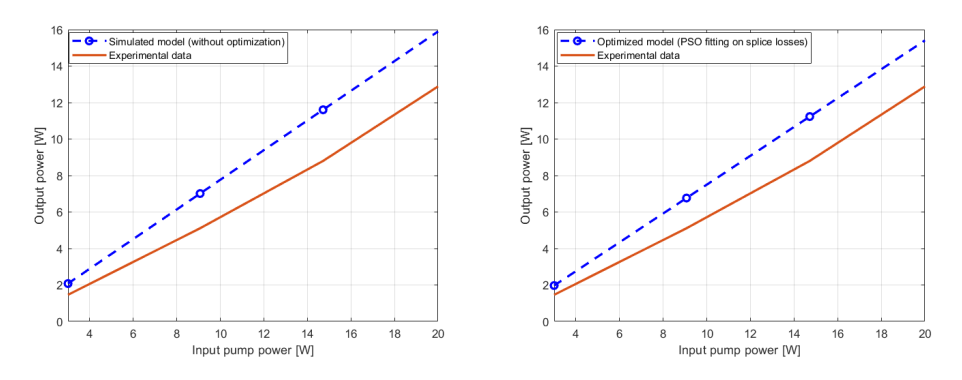


Figure 4.18: Comparison between experimental data and simulated model for  $10 \,\mathrm{m}$ , R = 0.04: (left) before and (right) after PSO optimization on splice losses.

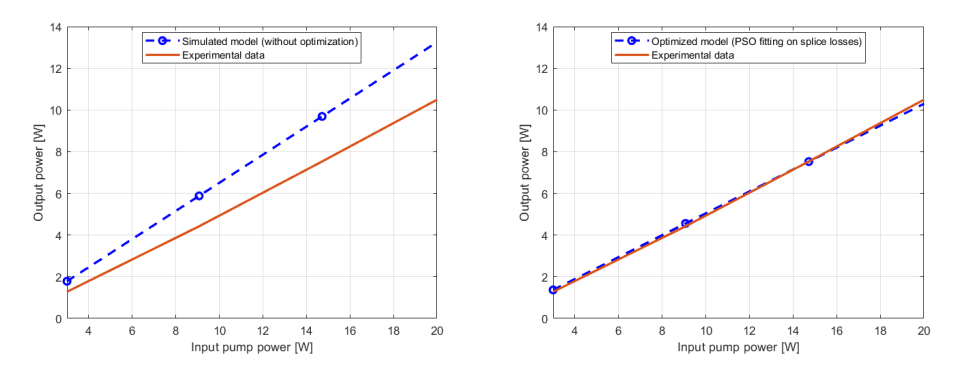


Figure 4.19: Comparison between experimental data and simulated model for  $L=10 \,\mathrm{m}$ , R=0.29: (left) before and (right) after PSO optimization on splice losses.

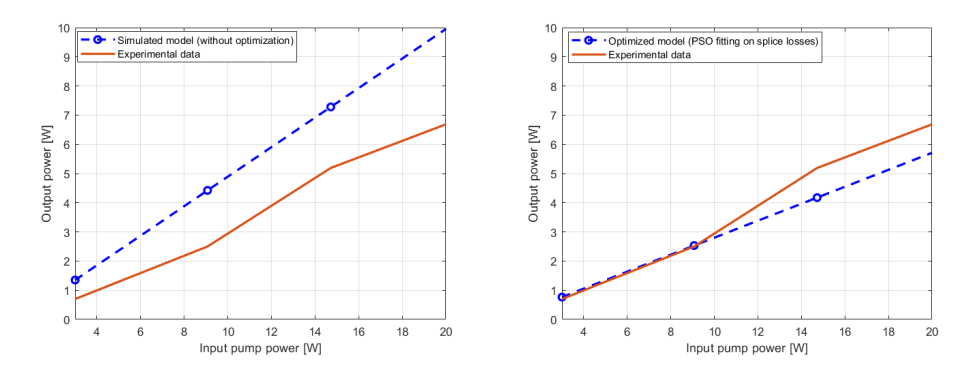


Figure 4.20: Comparison between experimental data and simulated model for  $L=10 \,\mathrm{m},\,R=0.60$ : (left) before and (right) after PSO optimization on splice losses.

For the cavity with R = 0.29 (Fig. 4.19), the optimization produces an almost perfect overlap between the simulated and experimental curves, indicating an excellent fitting quality and confirming the accuracy of the physical model when appropriate loss parameters are adopted.

In the sample with R = 0.60 (Fig. 4.20), the initial agreement between simulation and measurements is already satisfactory. However, as the pump power increases, a slight deviation appears.

Finally, in the case with R=0.04 (Fig. 4.18), the experimental and simulated curves exhibit similar slopes but are not perfectly superimposed. This behavior may be attributed to measurement uncertainties, possibly related to the power meter calibration.

Following the analysis of the 10 m cavities, the focus now shifts to the configurations employing a 15 m active fiber:

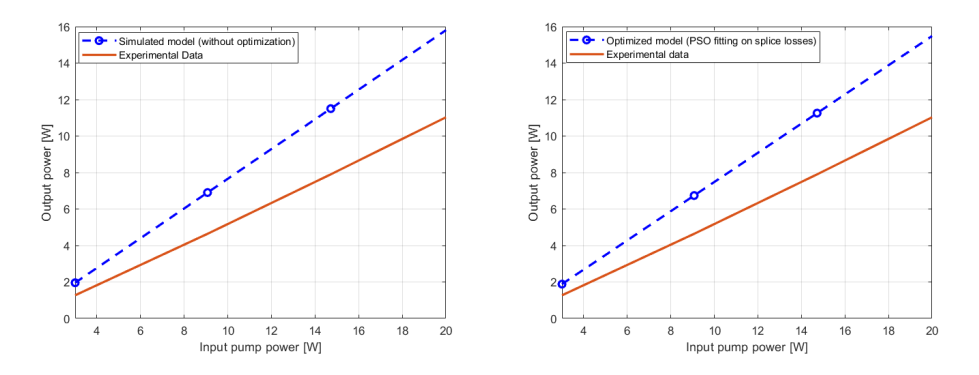


Figure 4.21: Comparison between experimental data and simulated model for  $15\,\mathrm{m}$ , R=0.04: (left) before and (right) after PSO optimization on splice losses.

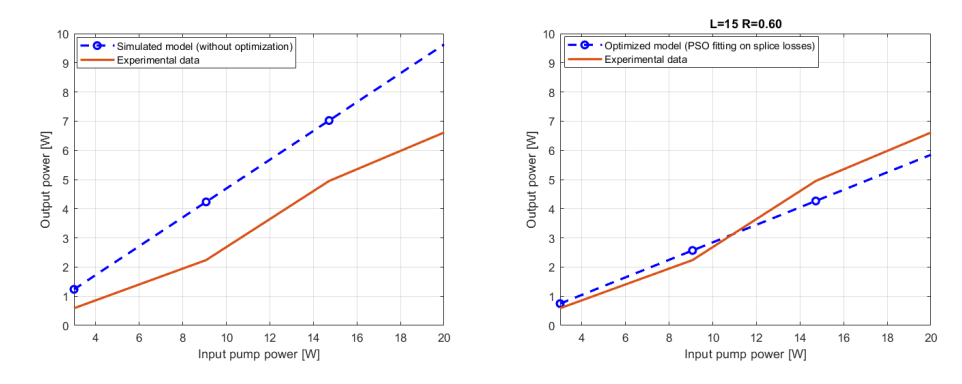


Figure 4.22: Comparison between experimental data and simulated model for  $L=15\,\mathrm{m}$ , R=0.60: (left) before and (right) after PSO optimization on splice losses.

As shown in Figs. 4.21 and 4.22, the effect of the PSO optimization on splice losses varies depending on the cavity configuration. For the 15 m, R = 0.04 case (Fig. 4.21), the optimization resulted in negligible changes, with the simulated model remaining closely aligned with the pre-optimization behavior.

In contrast, for the  $15 \,\mathrm{m}$ , R = 0.60 configuration (Fig. 4.20), a significant improvement is observed after optimization, demonstrating the effectiveness of the PSO procedure in this particular scenario.

Having analyzed the 15 m cavities, we now turn our attention to the 25 m sample.

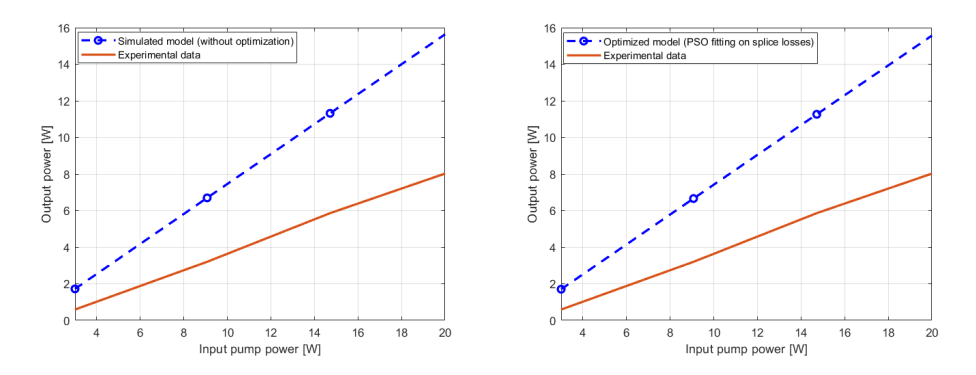


Figure 4.23: Comparison between experimental data and simulated model for  $25 \,\mathrm{m}$ , R = 0.04: (left) before and (right) after PSO optimization on splice losses.

In this case, the PSO optimization did not lead to a substantial improvement in the fitting, which was anticipated given that the experimental spectrum, as already noted in Fig. 4.5, exhibits a significant contribution from ASE.

Additional PSO tests were carried out on other physical parameters of the model, such as the total ion concentration  $(N_t)$  and the pump absorption and emission cross sections  $(\sigma_{ap} \text{ and } \sigma_{as})$ . These quantities are directly linked to the gain dynamics and the energy transfer processes within the active medium, and thus represent potential fitting variables. However, despite the increased number of degrees of

freedom, the obtained results did not exhibit a significant improvement compared to the single-parameter optimization based on splice losses. This outcome indicates that the discrepancies observed in the nominal simulations are mainly of macroscopic origin ,that is, related to the cavity coupling and propagation losses, rather than to uncertainties in the microscopic parameters of the active fiber.

The overall agreement between simulations and measurements confirms that the implemented model reliably reproduces the laser behavior under realistic operating conditions. Remaining deviations can be attributed to the limited number of experimental points, to the uncertainty of the thermal power meter especially at low powers, and to slight alignment errors between the collimating optics and the detector. Nonetheless, the optimized results demonstrate that the model can effectively adapt to experimental data through physically consistent parameters, thereby validating its use for parameter estimation and sensitivity analysis in subsequent sections.

# Chapter 5

# Conclusions

The main objective of this work was to develop and validate a numerical model capable of accurately estimating the internal parameters of YDFL cavities through an optimization process combined with experimental validation. Although a perfect match between simulation and measurement was not achieved, the results demonstrate that the proposed model can reproduce the real behavior of the system with good agreement, thus representing a reliable tool for the analysis and performance prediction of Yb<sup>3+</sup>-doped fiber lasers. The obtained results highlight a clear improvement in the model's ability to adapt to different experimental configurations, providing parameter values increasingly consistent with the measured data. This confirms the validity of the proposed approach and shows that, even in the presence of residual discrepancies, the model can effectively approximate the actual physical conditions inside the cavity.

The experimental activity, however, revealed some limitations of the measurement setup, mainly related to the thermal sensitivity of the power sensor and the difficulty in ensuring perfectly repeatable alignment conditions. Future developments should therefore focus on achieving a more stable and repeatable experimental system, for instance by employing temperature-compensated optical sensors and automated alignment procedures. Such improvements would significantly reduce measurement uncertainties and provide more reliable data for model validation. From the numerical perspective, a possible evolution of the work involves extending the model to include physical effects that were not yet considered, such as distributed losses along the fiber or amplified spontaneous emission (ASE), which could further enhance the accuracy of the simulations. At the same time, the introduction of adaptive optimization algorithms or artificial intelligence techniques could accelerate the convergence of the fitting process and make the parameter identification more robust and efficient.

In conclusion, the results achieved in this thesis confirm the soundness of the adopted methodology and provide a solid foundation for future research. The combination of a more reliable experimental setup and an increasingly complete numerical model 96 Conclusioni

will enable a progressively more realistic and predictive description of YDFL systems, bringing simulations closer to the actual operating conditions of high-performance fiber lasers.

# Bibliography

- [1] D. J. Richardson, J. Nilsson, and W. A. Clarkson. High power fiber lasers: current status and future perspectives. *Journal of the Optical Society of America B*, 27(11):B63–B92, 2010.
- [2] C. Jauregui and et al. High-power fiber lasers. Nature Photonics, 7:861–867, 2013.
- [3] R. Paschotta, J. Nilsson, A. C. Tropper, and D. C. Hanna. Ytterbium-doped fiber amplifiers. *IEEE Journal of Quantum Electronics*, 33(7):1049–1056, 1997.
- [4] Chen Shi, Hanwei Zhang, Xiaolin Wang, and Xu Xiaojun. Schematic of the yb-doped t-dcf based fiber amplifier. *Optics Express*, 2018.
- [5] VisCircuit. Euler vs runge-kutta methods, 2020. Accessed: October 2025.
- [6] R. Paschotta. Encyclopedia of laser physics and technology ytterbium-doped fibers. RP Photonics Encyclopedia, 2023. General theoretical reference for Ybdoped fibers.
- [7] Coherent / Nufern. NuYDF Ytterbium-Doped Double-Clad Fibers,  $10/125 \mu m$ , 2020. Manufacturer datasheet for Yb-doped DC 10/125 fiber.
- [8] C. Stihler, S. Jetschke, S. Unger, A. Schwuchow, and M. Leich. Spectroscopic properties of yb-doped phospho-aluminosilicate fibers for pbg 1178 nm emission. *Optical Materials Express*, 6(9):2956–2965, 2016.
- [9] Coherent. Large Mode Area (LMA) Ytterbium-Doped Double-Clad Fiber, 10/400
   μm, 2020. Datasheet for LMA Yb-doped double-clad fiber.
- [10] J. W. Dawson, M. J. Messerly, R. J. Beach, M. Y. Shverdin, E. A. Stappaerts, A. K. Sridharan, P. H. Pax, J. E. Heebner, C. W. Siders, and C. P. J. Barty. Analysis of the scalability of diffraction-limited fiber lasers and amplifiers to high average power. *Optics Express*, 16(17):13240–13266, 2008.

98 BIBLIOGRAPHY

[11] Jie Ma, Haitao Huang, Kaijie Ning, Xiaodong Xu, Guoqiang Xie, Liejia Qian, Kian Ping Loh, and Dingyuan Tang. Generation of 30-fs pulses from a diodepumped graphene mode-locked yb:cayalo4 laser. *IEEE Journal of Selected Topics in Quantum Electronics*, 21(1):1–7, 2015.

- [12] Elif Gül Özkan. Development of high power cw yb-doped fiber laser system. Master's thesis, Bilkent University, 2015.
- [13] T. H. Maiman. Stimulated optical radiation in ruby. Nature, 187:493–494, 1960.
- [14] E. Snitzer. Proposed fiber laser. *Journal of Applied Physics*, 32(10):1833–1834, 1961.
- [15] J. E. Geusic, H. M. Marcus, and L. G. Van Uitert. Laser oscillations in nd:yag. Applied Physics Letters, 4(10):182–184, 1964.
- [16] E. Snitzer, P. C. Becker, and H. J. Shaw. Double-clad fiber lasers. In Conference on Optical Fiber Communication. Optical Society of America, 1988.
- [17] R. J. Mears, L. Reekie, I. M. Jauncey, and D. N. Payne. Low-threshold tunable cw and q-switched fibre laser. *Electronics Letters*, 21(15):738–740, 1985.
- [18] D. C. Hanna, I. R. Perry, P. C. Rogers, M. J. F. Digonnet, and H. J. Shaw. Ytterbium fiber laser with wide tuning range. *Electronics Letters*, 24(20):1226–1227, 1988.
- [19] D. D. et al. 110 w yb-doped fiber laser. Optics Letters, 24(14):1047–1049, 1999.
  DOI not available; use as placeholder.
- [20] A. V. Barannikov and S. V. Turitsyn. 250 w linearly polarized yb fiber laser. In *Proceedings of SPIE*, volume 5335, pages 231–236, 2004.
- [21] V. Khitrov et al. 306 w polarization-maintained yb fiber laser. In *Proceedings* of SPIE, volume 5335, pages 210–215, 2004.
- [22] Y. Jeong, J. Nilsson, D. B. S. Soh, J. A. Alvarez-Chavez, W. A. Clarkson, H. J. Kim, S. U. Alam, and D. N. Payne. High-power ytterbium-doped fiber laser with 610 w output power. *Optics Letters*, 29(12):1230–1232, 2004.
- [23] Y. Jeong, J. Nilsson, D. B. S. Soh, J. A. Alvarez-Chavez, W. A. Clarkson, H. J. Kim, S. U. Alam, and D. N. Payne. 1.36 kw single-mode ytterbium-doped fiber laser. *Optics Letters*, 29(13):1534–1536, 2004.
- [24] G. A. Sincore, M. J. Andrejco, and D. L. Sipes. Pump absorption improvement in double-clad fibers. *Journal of Lightwave Technology*, 23(12):3790–3797, 2005.

BIBLIOGRAPHY 99

- [25] W. Koechner. Solid-State Laser Engineering. Springer, 2006.
- [26] J. Hecht. Understanding Fiber Optics. Prentice Hall, 2002.
- [27] K. O. Hill and G. Meltz. Fiber bragg grating technology fundamentals and overview. *Journal of Lightwave Technology*, 15(8):1263–1276, 1997.
- [28] R. Paschotta. Fiber lasers. Encyclopedia of Laser Physics and Technology, 2008.
- [29] G. P. Agrawal. Nonlinear Fiber Optics. Academic Press, 2013.
- [30] W. J. Wadsworth and et al. Large mode area fibers for high power applications. *Optics Express*, 11:48–53, 2003.
- [31] P. St. J. Russell. Photonic crystal fibers. Science, 299:358–362, 1995.
- [32] Author Unknown. High Power Fiber Laser Design and Modeling. PhD thesis, Technical University / Institution Name, Year. Retrieved from thesis document "Thesis\_high\_power\_RP.pdf".
- [33] Author Unknown. Ytterbium-Doped Fiber Amplifiers and Laser Systems. PhD thesis, Institution Name, Year. Retrieved from "Thesis with RP fiber power.pdf".
- [34] D. N. Payne. Rare-earth doped silica fibers. IEEE Journal of Quantum Electronics, 23(9):1509–1518, 1987.
- [35] MathWorks. fsolve Nonlinear system solver, 2023. https://www.mathworks.com/help/optim/ug/fsolve.html.
- [36] MathWorks. vpasolve Numeric solution of equations, 2023. https://www.mathworks.com/help/symbolic/vpasolve.html.
- [37] Ori Katz and Yoav Sintov. Strictly all-fiber picosecond ytterbium fiber laser utilizing chirped-fiber-bragg-gratings for dispersion control. *Proceedings of SPIE*, 7001:70011D, 2008.
- [38] Rüdiger Paschotta. Rp fiber power, 2025. RP Photonics Encyclopedia, accessed September 2025.
- [39] RP Photonics Encyclopedia. Absorption coefficient, 2025. Accessed: 2025-09-19.
- [40] RP Photonics Encyclopedia. Transition cross-sections, 2025. Accessed: 2025-09-19.
- [41] J. Kennedy and R. Eberhart. Particle swarm optimization. Proceedings of IEEE International Conference on Neural Networks, 4:1942–1948, 1995.